

An expanded workflow for **Navigating the complexity of detrital rutile provenance studies: An application: Methodological insights from the Neotethys Orogen in Anatolia**

Megan A. Mueller^{1,2,*}, Alexis Licht^{1,3}, Andreas Möller⁴, Cailey B. Condit¹, Julie C. Fosdick^{1,2}, Faruk Ocakoğlu⁵, Clay Campbell⁶

¹ Department of Earth and Space Sciences, University of Washington, 4000 15th Avenue NE, Seattle, WA 98195, USA

² Department of Earth Sciences, University of Connecticut, 354 Mansfield Road - Unit 1045, Storrs, CT 06269, USA

³ Department of Earth and Space Sciences, University of Washington, 4000 15th Avenue NE, Seattle, WA 98195, USA

⁴ Aix-Marseille Université, CNRS, IRD, INRAE, Collège de France, CEREGE, Technopôle de l'Arbois-Méditerranée, BP80, 13545 Aix-en-Provence, France

⁵ Department of Geology, The University of Kansas, 1414 Naismith Drive, Lawrence, KS 66045, USA

⁶ Department of Geological Engineering, Eskişehir Osmangazi University, Büyükdere, 26040 Eskişehir, Türkiye

^{*} Department of Geosciences, University of Arizona, 1040 E 4th St, Tucson, AZ 85721, USA

^{*} Now at Department of Geological Earth and Planetary Sciences, Jackson School of Geosciences, The University of Texas at Austin, 2305 Speedway Stop C1160, Austin, TX 78712, USA

Correspondence to: Megan Mueller (megan.mueller@jsg.utexas.edu)

Abstract. Sedimentary provenance is a powerful tool for reconstructing convergent margin evolution. Yet single mineral approaches, like detrital zircon, have struggled to track sediment input from mafic and metamorphic sources. Sediment input from these lithologies is especially critical for reconstructing orogenic settings dominated by terrane accretion, ophiolite obduction, and forearc inversion. Rutile can form in metamorphic and igneous rocks and hydrothermal veins, and its U-Pb age and geochemistry often records cooling from the most recent medium to high grade metamorphic event. Thus, detrital rutile complements detrital zircon datasets by offering a path forward in sedimentary provenance reconstructions where metamorphic terranes are potential source regions. However, U-Pb geochronology in rutile can be difficult due to low uranium concentrations and high discordance. Here, we present incorporation of common Pb, and multiple workflows are currently in use. Here, investigate U-Pb and trace element data reduction, processing, and common Pb correction workflows using new detrital rutile U-Pb geochronology and trace element geochemistry results from the Late Cretaceous to Eocene Central Sakarya and Sarıcakaya Basins in Anatolia to reconstruct provenance during Neotethys orogenesis. The resulting detrital rutile U-Pb analyses are highly discordant due to the incorporation of non-radiogenic initial Pb. We present a new workflow that accounts for low-U rutile and is based on common Pb corrections and discordance

- Style Definition: Heading 2
- Style Definition: Heading 3
- Style Definition: Heading 4
- Style Definition: Heading 5
- Style Definition: Heading 6
- Style Definition: Caption: Font: 10 pt, Not Bold, Italic
- Style Definition: Body: Font: 10 pt
- Formatted: Font: 17 pt, Bold, Font color: Black
- Formatted: Normal, Space Before: 18 pt, Line spacing: Multiple 1.83 li, Border: Top: (No border), Bottom: (No border), Left: (No border), Right: (No border), Between : (No border)
- Formatted: Font: 17 pt, Bold, Font color: Black
- Formatted: Font color: Black
- Formatted: Font: 12 pt, Font color: Black
- Formatted: Font: 12 pt, Font color: Black
- Formatted: Font: 12 pt, Font color: Black
- Formatted: Font: 12 pt, Font color: Black
- Formatted: Font: 12 pt, Font color: Black
- Formatted: Font color: Black
- Formatted: Font color: Black
- Formatted: Font color: Black
- Formatted: Font color: Black

- Formatted: Font color: Black
- Formatted: Font: +Headings (Times New Roman)
- Formatted: Font: +Body (Times New Roman), Not Bold, Font color: Auto
- Formatted: Heading 1, Line spacing: 1.5 lines

- Formatted: Font: +Body (Times New Roman), Not Bold, Font color: Auto
- Formatted: Font: +Body (Times New Roman), Not Bold, Font color: Auto

- Formatted: Font: +Body (Times New Roman), Not Bold, Font color: Auto

filters. The resulting age spectra are similar for grains up to 40% concordant (60% discordant) and across the common Pb correction methods, thus providing a path forward to confidently interpret provenance from discordant rutile grains. Together, the detrital rutile trace element geochemistry and Zr-in-rutile thermometry indicate sediment was sourced from mixed metamafic and metapelitic units with low grade metamorphic temperatures. Low-U concentration rutile are numerous and more discordant and were predominantly sourced from Late Triassic-Early Jurassic greenschist and blueschist facies rocks with both mafic and pelitic lithologies. This corresponds to sediment derived from the Karakaya Complex, a Paleozoic subduction-accretion complex or oceanic plateau that was accreted and metamorphosed in the Triassic-Jurassic, exhumed to the surface in the Jurassic, and then deformed during Neotethys suturing in the Late Cretaceous to Paleogene. Late Triassic-Early Jurassic ages are nearly absent from the detrital zircon record, emphasizing that a multi-mineral approach, especially inclusive of low U rutile, provides a more holistic provenance reconstruction. These detrital rutile results serve as an additional layer of data often unexplored across convergent margins globally, and thus provide an exciting path forward in characterizing diverse provenance of orogenic settings. A significant number of analyses were rejected (54%) due to signal intensity limitations, namely low U, low Pb, anomalous signal, and inclusions. We identify this as a universal limitation of large-*n* detrital rutile studies and recommend the systematic reporting of the amount of discarded analysis and the processes for rejection in all studies using detrital rutile U-Pb geochronology. Additionally, we show that (1) the ²⁰⁸Pb and ²⁰⁷Pb common Pb reduction schemes produce similar age distributions and can be used indifferently; (2) The Stacey-Kramers distance is a suitable metric for quantifying U-Pb discordance but a discordance filter is not recommended; (3) Instead, filtering U-Pb data by a power law function based on corrected date uncertainty is appropriate; (4) the exclusion of low uranium concentration rutile biases date distributions and favors pelitic-derived, higher Zr-in-rutile temperature, higher U-Pb concordance grains; (5) paired U-Pb and trace elements can be used to evaluate potential bias in U-Pb data rejection, which reveals that data rejection does not bias the provenance interpretations; (6) the signature of sediment recycling can be identified through U-Pb dates and Zr-in-rutile temperatures. To better navigate the complexity of detrital rutile datasets and to facilitate the standardization of data reporting approaches, we provide open access code as Jupyter Notebooks for data processing and analysis steps, including common Pb corrections, uncertainty filters, discordance calculations, and trace element analysis.

1 Introduction

The acceptance of plate tectonics brought about the recognition that sediment deposited in convergent margin basins archives orogenesis. Sedimentary provenance analysis is widely used to reconstruct ancient sediment dispersal networks, source-to-sink sediment budgets, sedimentary basin evolution, and to discern links between tectonics, geodynamics, paleogeography, climate, and biologic evolution (Dickinson and Suczek, 1979; Garzanti et al., 2007; Clift et al., 2008; Gehrels, 2014; Blum and Pecha, 2014). Not only do sedimentary basins archive these processes in their stratigraphic architecture and environments of deposition, but they are often the best, and sometimes only, record of these processes in deep time. In convergent margin settings, sedimentary provenance analysis uses the mineralogical

Formatted: Font: Arial Nova Light

Formatted: Font color: Black

70 and geochemical composition of sedimentary rocks to interpret changes in sediment source as a function of geodynamics, deformation, topography, climate, and paleogeography.

75 ~~Classic~~Compositional provenance methods include ~~bulk~~ sediment petrologic, chemical, and heavy mineral characterizations (e.g., Gazzi, 1965; Hubert, 1971; Dickinson and Suczek, 1979; Morton, 1985; Garzanti and Andò, 2007). Over the last several decades, the rise of chronometric and geochemical techniques ~~has elevated~~led to the ~~increase in~~ single-mineral approaches. Detrital zircon U-Pb geochronology has become the ~~gold standard~~most widely ~~used~~ technique ~~as zircon is refractory and is abundant in crustal rocks~~ (e.g., Gehrels, 2014). ~~Further~~, the age, thermal history, and elemental and isotopic composition of detrital zircons can quantitatively reconstruct both sedimentary provenance and geodynamic, tectonic, and magmatic processes (Carrapa, 2010; Paterson and Ducea, 2015; Tang et al., 2020; Sundell et al., 2022). ~~However, one major limitation is that zircons predominantly form in intermediate to felsic magmas, thus detrital zircon suites generally lack information about mafic igneous and metamorphic processes and sources (Hietpas et al., 2011; Moecher et al., 2011; Gaschnig, 2019). Although zircon~~Zircon is present in metamorphic rocks as ~~small~~ inclusions in other minerals or as recrystallized-dissolved-reprecipitated rims on zircon cores (Kohn and Kelly, 2017). ~~The outer growth domains of zircons can be targeted with laser ablation ICP-MS depth profiling or with spot analysis if the standard detrital zircon U-Pb geochronology rims are thick enough, yet the most commonly used~~ techniques for rapid provenance data acquisition (~~i.e., laser ablation ICP-MS~~) do not routinely analyze ~~zircon rims. Therefore, sedimentary provenance interpretations based on detrital zircon alone are incomplete. For this reason the sedimentary provenance community is increasingly turning to U-Th-Pb and trace elements in~~ phases commonly used in petrochronology, such as detrital rutile (Zack et al., 2004a; Meinhold, 2010; Triebold et al., 2012; Bracciali et al., 2013; Rösel et al., 2014, 2019; O'Sullivan et al., 2016; Odlum et al., 2019; Pereira et al., 2020), ~~detrital apatite~~ (Morton and Yaxley, 2007; Chew et al., 2011; Mark et al., 2016; O'Sullivan et al., 2016, 2020), detrital monazite (Hietpas et al., 2010; Moecher et al., 2011; Gaschnig, 2019), and detrital titanite (Guo et al., 2020; Chew et al., 2020). ~~The 'zircon problem' is especially pronounced in continental collision and accretionary orogenic settings where obducted ophiolites, ophiolitic mélange, metamafic and metapelitic terranes, and exhumed metamorphic massifs are commonly exposed, and the P-T-t history of these units pinpoint important geodynamic milestones, in addition to other isotopic systems in these and other detrital minerals.~~

95 Detrital rutile is a ~~promising~~complementary sedimentary provenance proxy to ~~overcome this~~detrital zircon ~~problem~~. Rutile ~~can form~~forms in metamafic and metapelitic rocks across a range of P-T conditions, therefore, detrital rutile is especially advantageous when tracking sediment input from greenschist to eclogite ~~or granulite facies sources~~ (e.g., Meinhold, 2010; Zack and Kooijman, 2017) ~~facies sources~~. ~~With a U-Pb closure temperature of 490–640°C, rutile U-Pb dates correspond. The geochemical composition~~cooling from the most recent medium to high temperature metamorphic event that exceeded the closure temperature (Zack et al., 2004b; Zack and Kooijman, 2017). ~~Hence, first-cycle detrital rutile can track sediment input from metamorphic units. The geochemical composition (Cr/Nb) can~~ further distinguish between metamorphic protoliths (e.g., Triebold et al., 2007, 2012; Meinhold, 2010). ~~Analytically, though, U-Pb geochronology in~~rutile ~~can be difficult~~U-Pb analysis is challenging due to low ~~uranium~~U and ~~low radiogenic Pb~~ concentrations. ~~For this reason, some studies only analyze or interpret and due to the incorporation of initial non-radiogenic Pb. Here, we use a new~~ detrital rutile ~~above a given U threshold~~. ~~However, this analytical~~

Formatted: Font color: Black

Formatted: Font color: Black

Formatted: Font color: Black

Formatted: Font color: Black

Formatted: Font color: Black

Formatted: Font color: Black

Formatted: Font color: Black

Formatted: Font color: Black

Formatted: Font color: Black

Formatted: Font color: Black

Formatted: Font color: Black

Formatted: Font color: Black

approach likely biases provenance results as the concentration of uranium in rutile systematically varies by metamorphic protoliths, with mafic eclogites having lower U contents than metapelites.

Here, we investigate the limitations of U threshold filtering with a new petrochronology dataset from Anatolia inclusive of all rutile, where low U rutile grains are numerous and diagnostic of specific metamorphic units to investigate data reduction, processing and analytical steps in order to support robust provenance interpretations. In a number of studies, analyses have been discarded during U-Pb data reduction due to unacceptable signal intensity (e.g. Bracciali et al., 2013; Rösel et al., 2014, 2019), and we find that discarding analyses is a limitation to large-*n* detrital rutile datasets in the literature and this study. We build a new workflow that includes low U rutile and tests different common Pb correction approaches. Furthermore, we test the sensitivity of resulting U-Pb date spectra to the Pb correction methods, uncertainty, and to discordance filters and determine whether these factors alter the overall provenance interpretation. Overall, this, and a low U cutoff threshold. Ultimately, the new dataset demonstrates that detrital rutile captures sediment input from a subduction accretion complex that is poorly resolved in the detrital zircon record. Despite the described limitations, detrital rutile petrochronology can be effectively used to reconstruct sedimentary provenance and sediment recycling, deformation, and metamorphism.

2 Detrital Rutile Provenance

2.1 Detrital Rutile Synopsis

The utility advantages of detrital rutile is provenance are extensively documented (e.g., Zack et al., 2004a; Meinhold, 2010; Triebold et al., 2012; Bracciali, 2019; Gaschnig, 2019; Pereira et al., 2020; Pereira and Storey, 2023) so here we provide only a brief overview here. Rutile is the most common TiO₂ polymorph, a common accessory mineral in metamorphic and igneous rocks (Meinhold, 2010; Zack and Kooijman, 2017), and an abundant heavy mineral in sedimentary rocks (Morton, 1985). Rutile is present across a range of P-T conditions: rutile is generally stable at the surface and medium- to high-grade metamorphic conditions. Rutile can readily crystallize from titanite, ilmenite and biotite during prograde metamorphism (Luvizotto et al., 2009; Meinhold, 2010; Cave et al., 2015). The breakdown of rutile to titanite occurs in prograde and retrograde environments, particularly in sub-greenschist to lower greenschist facies where titanite stability is favored (Cave et al., 2015; Zack et al., 2004b). Experimentally, rutile is stable above around 1.2–1.4 GPa in metagranitoids and hydrated basalts depending on compositional and chemical variability and in some cases can be stable down to 0.7 GPa (Xiong et al., 2005; Angiboust and Harlov, 2017). In subduction zone settings, rutile is especially abundant in eclogites (Klemme et al., 2002). During prograde metamorphism, rutile crystallizes from ilmenite and biotite and rutile's chemical composition.

The chemical composition of rutile preserves original petrogenetic information. Rutile concentrates high field strength elements (Zr, Nb, Mo, Sn, Sb, Hf, Ta, W) through substitution with Ti that are commonly used as fingerprints of subduction zone metamorphism and crustal evolution (Foley et al., 2000; Rudnick et al., 2000) (e.g., Nb and Ta). Detrital rutile geochemistry fingerprints the lithologies of sediment sources in several unique ways: First, rutile concentrates the vast majority of available Nb whereas Cr is non-selective and is distributed across metamorphic minerals; therefore, the Cr and Nb concentrations in rutile can discriminate between metamafic and

Formatted: Font color: Black

Formatted: Normal, Indent: First line: 0.5", Border: Top: (No border), Bottom: (No border), Left: (No border), Right: (No border), Between : (No border)

Formatted: Font color: Black

Formatted: Font color: Black

Formatted: Font color: Black

Formatted: Font color: Black

Formatted: Font color: Black

Formatted: Font color: Black

Formatted: Font color: Black

Formatted: Font color: Black

Formatted: Font color: Dark Red

Formatted: Font: +Headings (Times New Roman)

Formatted: Font: +Headings (Times New Roman)

Formatted: Font: +Headings (Times New Roman), Font color: Black

Formatted: Font: +Headings (Times New Roman), Font color: Black

Formatted: Font: +Headings (Times New Roman), Font color: Black

Formatted: Font: +Headings (Times New Roman)

Formatted: Font: +Headings (Times New Roman)

Formatted: Font: +Headings (Times New Roman)

Formatted: Font: +Headings (Times New Roman)

Formatted: Font: +Headings (Times New Roman)

Formatted: Font: +Headings (Times New Roman)

Formatted: Font: +Headings (Times New Roman)

Formatted: Font: +Headings (Times New Roman)

Formatted: Font: +Headings (Times New Roman), Font color: Black, English (United Kingdom)

Formatted: Font: +Headings (Times New Roman), Font color: Black, English (United Kingdom)

Formatted: Font: +Headings (Times New Roman), English (United Kingdom)

Formatted: Font: +Headings (Times New Roman), Font color: Black, English (United Kingdom)

Formatted: Font: +Headings (Times New Roman), Font color: Black, English (United Kingdom)

metapelitic lithologies (Zack et al., 2004a, b; Triebold et al., 2011, 2012), Cr and Nb concentrations are attributed to different protoliths: metapelitic rutile (i.e. mica schists, paragneisses, felsic granulites) have Cr < Nb and metabasic rutile (i.e., mafic eclogites and granulites) have Cr > Nb, generally (Zack et al., 2004b). ~~Second~~ Additionally, the incorporation of Zr in rutile is largely temperature dependent (Zack et al., 2004b; Watson et al., 2006; Tomkins et al., 2007; Ferry and Watson, 2007). Zirconium mobilizes during prograde metamorphic fluid release; the incorporation of Zr into rutile is buffered by coexisting quartz and zircon (Zack et al., 2004b). Zr contents in rutile correlate with peak metamorphic temperature and pressure conditions (Zack et al., 2004b; Watson et al., 2006; Tomkins et al., 2007; Kohn, 2020). Therefore, the Zr elemental composition in rutile is a commonly used thermometer, empirically and experimentally calibrated across a range of pressures and thermodynamic activity parameters (Zack et al., 2004b; Watson et al., 2006; Tomkins et al., 2007; Kohn, 2020). Zircon, quartz and rutile must be equilibrium to use the Zr-in-rutile thermometer (e.g., Zack et al., 2004b), an assumption that likely holds in pelitic rocks (Pereira et al., 2021) but may not in mafic lithologies, yet the assumption is hard to evaluate in a detrital context. Inclusions in rutile can be used to determine whether rutile grew in equilibrium (Hart et al., 2016, 2018; see also Pereira and Storey, 2023 and references therein). In detrital rutile, removed from the petrologic system in which they formed, and thereby miss key thermobarometric mineral associations, the Zr-in-rutile thermometer thus provides an estimate of the minimum peak metamorphic temperatures because the exact activity of SiO₂ in the original system is unconstrained (Kooijman et al., 2012; Triebold et al., 2012; Pereira et al., 2021; see also Meinhold et al., 2008; Rösel et al., 2019; Şengün et al., 2020; Zoleikhaei et al., 2021) In detrital minerals, which are removed from the context of constitutive relationships (i.e., pressure and silica activity), these thermometers can provide an estimate of the minimum peak metamorphic temperatures. For rutile of unknown source lithology, the calculated temperature is affected by the chosen pressure estimate; Pereira and Storey (2023) demonstrate this pressure dependence in detrital grains, and therefore, recommend using the experimental and empirical calibration of Kohn (2020; their eqn. 13) at an average pressure of 13 kbar with an uncertainty of 5 kbar:

$$T \text{ (}^\circ\text{C)} = \frac{71360 + 0.378 \cdot P(\text{bars}) - 0.130 \cdot C(\text{ppm})}{130.66 - R \cdot \ln[C(\text{ppm})]} = \frac{71360 + 0.378 \times P - 0.130 \times C}{130.66 - R \times \ln[C]} - 273.15$$

where P is the pressure in bars, C is the concentration of Zr in ppm and R is the gas constant, 8.3144 in J·mol⁻¹·K⁻¹.

Uranium is easily substituted for Ti⁴⁺ in rutile at concentrations up to ~100 ppm U making rutile a suitable mineral for U-Pb analysis. Rutile U-Pb analyses were first performed using thermal ionization mass spectrometry (TIMS) (Schärer et al., 1986; Mezger et al., 1989; Möller et al., 2000; Schmitz and Bowring, 2003; Kylander-Clark et al., 2008) and have since been collected with SHRIMP (Clark et al., 2000; Meinhold et al., 2010; Ewing et al., 2015), LA-MC-ICP-MS (Vry and Baker, 2006; Bracciali et al., 2013; Apen et al., 2020), LA-Q-ICP-MS (Storey et al., 2007; Zack et al., 2011), and LA-SC-ICP-MS (Kooijman et al., 2010; Okay et al., 2011; Smye and Stockli, 2014). As a high-temperature thermochronometer, U-Pb dates in rutile likely reflect mineral cooling through the closure temperature for volume diffusion of Pb (Dodson, 1973), which is between 400–640°C in rutile. The temperature sensitivity of this partial retention zone in rutile is dependent on diffusion kinetics, cooling rate, chemistry, and grain size (Mezger et al., 1989; Cherniak, 2000). Rutile U-Pb dates may correspond to monotonic cooling from post-magmatic temperatures or cooling from the most recent medium to high-temperature metamorphic event that exceeded the closure temperature (Zack et al., 2004b; Zack and

Formatted: Font: +Headings (Times New Roman)

Formatted: Font: +Headings (Times New Roman), Font color: Black, English (United Kingdom)

Formatted: Font: +Headings (Times New Roman)

Formatted: Font: +Headings (Times New Roman)

Formatted: Font: +Headings (Times New Roman), Font color: Black

Formatted: Font: +Headings (Times New Roman)

Formatted: Font: +Headings (Times New Roman), Font color: Black

Formatted: Font: +Headings (Times New Roman), Font color: Black, English (United Kingdom)

Formatted: Font: +Headings (Times New Roman)

Formatted: Font: +Headings (Times New Roman), Font color: Black, English (United Kingdom)

Formatted: Font: +Headings (Times New Roman)

Formatted: Font: +Headings (Times New Roman)

Formatted: Font: +Headings (Times New Roman)

Formatted: Font: +Headings (Times New Roman)

Formatted: Font: +Headings (Times New Roman)

Formatted: Font: +Headings (Times New Roman), Not Italic

Formatted: Font: +Headings (Times New Roman), Bold

Formatted: Font: +Headings (Times New Roman), Not Italic

Formatted: Font: +Headings (Times New Roman), Bold

Formatted: Font: +Headings (Times New Roman), Bold, Not Italic

Formatted: Font: +Headings (Times New Roman), Not Italic

Formatted: Font: +Headings (Times New Roman), Bold

Formatted: Font: +Headings (Times New Roman)

Formatted: Font: +Headings (Times New Roman)

Formatted: Font: +Headings (Times New Roman)

Formatted: Font: +Headings (Times New Roman), Font color: Black

Formatted: Font: +Headings (Times New Roman), Font color: Black

180 Kooijman, 2017). Slow cooling rates can produce rutile U-Pb dates significantly younger than the timing of
peak metamorphism (e.g., Möller et al., 2000; Flowers et al., 2005). Because rutile U-Pb dates record thermal
history information from conditions characteristic of the middle to lower crust (> 400 °C), U-Pb dates are ideal
for inferring the timing and rate of deep seated orogenic processes (Mezger et al., 1989; Möller et al., 2000;
185 Flowers et al., 2005; Kylander-Clark et al., 2008; Smye et al., 2018) and of craton formation, stabilization and
cooling (Davis et al., 2003; Schmitz and Bowring, 2003; Blackburn et al., 2012). Furthermore, detrital rutile U-
Pb geochronology is regularly used in sedimentary provenance analysis to reconstruct sedimentary basin
evolution, paleoclimate and paleoenvironments, and orogen-scale deformation, exhumation, and sediment
transport (Rösel et al., 2014, 2019; Mark et al., 2016; O'Sullivan et al., 2016; Pereira et al., 2020; Caracciolo et

190 2.2 Detrital Rutile U-Pb Challenge #1: Low Uranium Content

Detrital rutile U-Pb petrochronology presents unique analytical, data reduction, and interpretation challenges.
Uranium concentration in rutile varies among metamorphic protoliths: for example, rutile from mafic eclogites tend
to have, on average, 75% less U than those from metapelites (i.e., 5 ppm vs. 21 ppm; Meinhold, 2010). Analytically,
195 the low U concentrations in— from old rutile, predominantly or, sourced from mafic lithologies— (cf. Section 6.2)—
can make rutile challenging to date. To optimize data collection, many some detrital rutile methods first analyze trace
elements then only collect U-Pb data on rutile above a given U concentration threshold (ca. > 4–5 ppm; e.g., Zack et
al., 2004a, 2011; Okay et al., 2011; Rösel et al., 2019). As expected There is not a systematic relationship between
uranium concentration and common Pb concentration. However, screening low U rutile produces a higher proportion
200 of concordant analyses and U rutile, reduces the overall length of U-Pb analytical sessions and produces a higher
proportion of concordant analyses (Zack et al., 2004a, 2011; Okay et al., 2011; Rösel et al., 2019), but, This protocol
however, introduces bias into the provenance results against metamafic rocks (cf. Section 6.2), and is generally
discouraged (Bracciali et al., 2013; Bracciali, 2019). While this low-U screening is not necessarily common globally,
it is a regional concern. There are 4 published detrital rutile U-Pb datasets from Türkiye: 2 of the 4 (Okay et al., 2011;
205 Şengün et al., 2020) only analyze U-Pb on detrital rutile with uranium concentrations above ca. 4–5 ppm. The two
studies that do not use a U-threshold filter but instead analyze all detrital rutile grains (Shaanan et al., 2020; this study)
must discard data due to very low uranium signals (below limit of detection: LOD). The U-threshold filter is intended
to maximize the proportion of concordant rutile analyzed. This includes rutile grains that have low incorporation of
U during growth (independent of analytical instrumentation) and rutile grains that have poorly resolved U-Pb ratios
210 due to low U CPS such as old rutile and mafic rutile (machine dependent). Omitting low U rutile may make sense in
some geologic settings; however, this analytical approach likely biases provenance results as the concentration of
uranium in rutile systematically varies by metamorphic protoliths, with mafic eclogites having lower U contents than
metapelites (e.g., Meinhold, 2010) based on the lithology of potential sediment sources; however, This potential bias
is important to investigate as metamafic units in suture zones, presumably with low U rutile, are expected to be a
215 major contributor of detritus to many orogenic basins, including the northwestern Anatolian basins of this study.
Therefore, we explore whether analyzing detrital rutile of all U concentrations offers the opportunity to reconstruct a
completer and more representative sedimentary provenance in forearc and suture zone settings during subduction and
collision.

Formatted: Font: +Headings (Times New Roman)

Formatted: Font: +Headings (Times New Roman)

Formatted: Font: +Headings (Times New Roman)

Formatted: Font: +Headings (Times New Roman)

Formatted: Font: +Headings (Times New Roman)

Formatted: Font: +Headings (Times New Roman)

Formatted: Font: +Headings (Times New Roman)

Formatted: Font: +Headings (Times New Roman)

Formatted: Font: +Headings (Times New Roman)

Formatted: Font: +Headings (Times New Roman)

Formatted: Font: +Headings (Times New Roman)

Formatted: Font: +Headings (Times New Roman)

Formatted: Font: +Headings (Times New Roman)

Formatted: Font: +Headings (Times New Roman)

Formatted: Font: +Headings (Times New Roman)

Formatted: Font: +Headings (Times New Roman)

Formatted: Font: +Headings (Times New Roman)

Formatted: Font: +Headings (Times New Roman)

Formatted: Font: +Headings (Times New Roman)

Formatted: Font: +Headings (Times New Roman)

Formatted: Font: +Headings (Times New Roman)

2.3 Detrital Rutile U-Pb Challenge #2: Common Pb Incorporation

2.3.1 Common Pb Correction Overview

A second challenge with detrital rutile lies with data reduction and presentation. ~~Because many detrital geochronologists are familiar with the zircon system, here we emphasize the differences in how U-Pb data should be treated in common Pb bearing minerals versus zircon.~~ The U-Pb system in rutile is different from that of zircon, ~~for example,~~ due to the incorporation of common Pb, thereby requiring careful methodological choices on how to treat non-radiogenic Pb and U-Pb discordance. The zircon U-Pb system is 'simple' in the sense that zircon incorporates negligible non-radiogenic initial or 'common' Pb during crystallization, and Pb diffuses only at extremely high temperatures and in zircon with radiation damage (e.g., Schoene, 2014 and references therein). Thus, the majority of detrital zircon U-Pb analyses tend to be close to concordia, ~~and significant discordance is dominantly controlled by recent Pb loss facilitated by radiation damage accumulation.~~ This ~~which~~ makes data reduction and interpretation ~~more fairly~~ straightforward, as even the $^{207}\text{Pb}/^{206}\text{Pb}$ dates of moderately discordant zircon are likely to be meaningful. Rutile, on the other hand, can incorporate significant common Pb, can have low U contents, and is more sensitive to thermally activated Pb diffusion over a wide range of lithospheric thermal conditions. Therefore, most rutile U-Pb dates are expected to be discordant. Unlike zircon where discordant data exceeding a specified threshold are often discarded, it is not surprising that many rutile analyses may be discordant as rutile can incorporate a significant amount of common Pb. *In-situ* studies mitigate this by: (1) regressing discordia lines through co-genetic analyses in Tera-Wasserburg space, where the lower intercept of the discordia with the concordia defines the U-Pb age of Pb diffusion closure (e.g., Faure, 1986; Chew et al., 2011; Vermeesch, 2020); or (2) applying a non-radiogenic Pb correction using either ~~by using an ad hoc Pb evolution model such as that of Stacey and Kramers (1975), or by measuring the composition of non-radiogenic Pb in a co-existing phase.~~ (e.g. Zack et al. 2004b). However, by nature, the co-genetic grains in detrital samples are unknown. ~~This creates a first order methodological hurdle for detrital petrochronology: what is the best way to determine the U-Pb age for discordant detrital analyses?; and do different discordance filters influence the resulting age spectra and provenance interpretations or not?~~ This careful methodological step is critical to produce age distributions that can a model therefore has to be interpreted confidently applied. Below we review ^{208}Pb -based the common Pb correction calculations and ^{207}Pb -based methods discordance metrics for calculating U-common Pb dates in discordant grains, then we illustrate this comparison with a new dataset from Anatolia bearing detrital minerals.

2.3.2 ^{204}Pb Correction

The basis of all common Pb correction approaches— ^{204}Pb , ^{207}Pb and ^{208}Pb —is to use a Pb evolution model (e.g., Stacey and Kramers, 1975) to find the fraction of total ^{206}Pb that is common ^{206}Pb and, by corollary, find the radiogenic ^{206}Pb fraction and then calculate the corrected date (Compston et al., 1984; Williams, 1997). We did not measure ^{204}Pb in this study and refer readers to other publications for ^{204}Pb correction details (Williams, 1997; Andersen, 2002; Storey et al., 2006; Chew et al., 2014). The ^{204}Pb correction method is valuable because it uses the non-radiogenic ^{204}Pb isotope and does not assume concordance, yet accurate measurement of ^{204}Pb is needed (in contrast, see Andersen, 2002) which can be challenging as ^{204}Pb is the least abundant Pb isotope. While accurate

Formatted: Font: +Headings (Times New Roman)

Formatted: Font: +Headings (Times New Roman)

Formatted: Font: +Headings (Times New Roman)

Formatted: Font: +Headings (Times New Roman)

Formatted: Font: +Headings (Times New Roman)

Formatted: Font: +Headings (Times New Roman)

Formatted: Font: +Headings (Times New Roman)

Formatted: Font: +Headings (Times New Roman)

Formatted: Font: +Headings (Times New Roman)

Formatted: Font: +Headings (Times New Roman)

Formatted: Font: +Headings (Times New Roman)

Formatted: Font: +Headings (Times New Roman)

Formatted: Font: +Headings (Times New Roman)

Formatted: Font: +Headings (Times New Roman)

Formatted: Font: +Headings (Times New Roman)

Formatted: Font: +Headings (Times New Roman)

Formatted: Font: +Headings (Times New Roman)

Formatted: Font: +Headings (Times New Roman)

Formatted: Font: +Headings (Times New Roman)

Formatted: Font: +Headings (Times New Roman)

Formatted: Font: +Headings (Times New Roman)

Formatted: Font: +Headings (Times New Roman)

Formatted: Font: +Headings (Times New Roman)

Formatted: Font: +Headings (Times New Roman)

Formatted: Font: +Headings (Times New Roman)

Formatted: Font: +Headings (Times New Roman)

Formatted: Font: +Headings (Times New Roman)

255 [determination of the low-intensity \$^{204}\text{Pb}\$ peak is not a problem for TIMS or MC-ICP-MS instruments](#) (e.g., Simonetti et al., 2005; Gehrels et al., 2008), [it can require prohibitively long dwell times in single-collector instruments.](#) [Furthermore, the measurement of \$^{204}\text{Pb}\$ is complicated by the isobaric interference of \$^{204}\text{Hg}\$ introduced in the gas supply. In some cases, the concentration of \$^{204}\text{Hg}\$ can be reduced with traps or filters and back stripped by measuring \$^{201}\text{Hg}\$ or \$^{202}\text{Hg}\$](#) (e.g., Storey et al., 2006).

260 **2.3.3. ^{208}Pb Correction**

The ^{208}Pb correction method determines the common Pb component using the ^{232}Th - ^{208}Pb decay scheme and assumes U-Th-Pb concordance ~~and no Pb loss, undisturbed Th/U, and no Pb loss. Because Pb loss is not considered, all corrected dates are (possibly) minimum ages.~~ The ^{208}Pb correction is ideal for low-Th phases (Zack et al., 2011) and is commonly used for rutile, although not all rutile [grains](#) have low Th concentrations ~~and Th contents are often not reported.~~ The ~~method~~ equations here are previously described in Williams (1997) ~~directly follows the method of,~~ Chew et al. (2011) ~~and Odium et al., which is also discussed in,~~ McLean et al. (2011) and as the total-Pb/U-Th scheme in Vermeesch (2020).

The proportion of $^{206}\text{Pb}_{\text{common}}$, f_{206} , is calculated as

$$f_{206} = \frac{(^{208}\text{Pb}/^{206}\text{Pb}_{\text{measured}}) - (^{208}\text{Pb}^*/^{206}\text{Pb}^*)}{(^{208}\text{Pb}/^{206}\text{Pb}_{\text{common}}) - (^{208}\text{Pb}^*/^{206}\text{Pb}^*)}$$

270 where $^{208}\text{Pb}/^{206}\text{Pb}_{\text{measured}}$ is calculated directly from the raw data. The $^{208}\text{Pb}/^{206}\text{Pb}_{\text{common}}$ ratio is calculated from the two-stage Pb evolution model of Stacey and Kramers (1975) for dates ~~younger~~older than 3.7 Ga ~~using~~ t_i as

$$\left(\frac{^{206}\text{Pb}}{^{204}\text{Pb}}\right)_{\text{common}} = 7.19 \cdot (e^{\lambda_{238} \cdot 4.57 \times 10^9} - e^{\lambda_{238} \cdot t_i}) + 9.307$$

275 and

$$\left(\frac{^{208}\text{Pb}}{^{204}\text{Pb}}\right)_{\text{common}} = 33.21 \cdot (e^{\lambda_{232} \cdot 4.57 \times 10^9} - e^{\lambda_{232} \cdot t_i}) + 29.487$$

or for dates younger than 3.7 Ga as

$$280 \left(\frac{^{206}\text{Pb}}{^{204}\text{Pb}}\right)_{\text{common}} = 9.74 \cdot (e^{\lambda_{238} \cdot 3.7 \times 10^9} - e^{\lambda_{238} \cdot t_i}) + 11.152$$

and

$$285 \left(\frac{^{208}\text{Pb}}{^{204}\text{Pb}}\right)_{\text{common}} = 36.84 \cdot (e^{\lambda_{232} \cdot 3.7 \times 10^9} - e^{\lambda_{232} \cdot t_i}) + 31.23$$

- Formatted: Font: +Headings (Times New Roman)
- Formatted: Font: +Headings (Times New Roman)
- Formatted: Font: +Headings (Times New Roman)
- Formatted: Font: +Headings (Times New Roman)
- Formatted: Font: +Headings (Times New Roman)
- Formatted: Font: +Headings (Times New Roman)
- Formatted: Font: +Headings (Times New Roman)
- Formatted: Font: +Headings (Times New Roman)
- Formatted: Font: +Headings (Times New Roman)
- Formatted: Font: +Headings (Times New Roman)
- Formatted: Font: +Headings (Times New Roman)
- Formatted: Font: +Headings (Times New Roman), Not Italic
- Formatted: Font: +Headings (Times New Roman), Bold
- Formatted: Font: +Headings (Times New Roman), Not Italic
- Formatted: Font: +Headings (Times New Roman), Bold, Not Italic
- Formatted: Font: +Headings (Times New Roman)
- Formatted: Font: +Headings (Times New Roman)
- Formatted: Font: +Headings (Times New Roman)
- Formatted: Font: +Headings (Times New Roman)
- Formatted: Font: +Headings (Times New Roman), Not Italic
- Formatted: Font: +Headings (Times New Roman), Bold
- Formatted: Font: +Headings (Times New Roman), Not Italic
- Formatted: Font: +Headings (Times New Roman)
- Formatted: Normal
- Formatted: Font: +Headings (Times New Roman)
- Formatted: Font: +Headings (Times New Roman), Not Italic
- Formatted: Font: +Headings (Times New Roman), Bold
- Formatted: Font: +Headings (Times New Roman), Not Italic
- Formatted: Font: +Headings (Times New Roman), Bold
- Formatted: Font: +Headings (Times New Roman), Not Italic
- Formatted: Font: +Headings (Times New Roman), Bold
- Formatted: Font: +Headings (Times New Roman), Not Italic
- Formatted: Font: +Headings (Times New Roman)
- Formatted: Normal
- Formatted: Font: +Headings (Times New Roman)

where using t_i is the uncorrected date in years, the ^{232}Th decay rate λ_{232} is $4.9475 \times 10^{-11} \text{ yr}^{-1}$, and the ^{238}U decay rate λ_{238} is $1.55125 \times 10^{-10} \text{ yr}^{-1}$ (Faure, 1986) and the expected radiogenic $^{208}\text{Pb}^*/^{206}\text{Pb}^*$ ratios are calculated as

$$\frac{^{208}\text{Pb}^*}{^{206}\text{Pb}^*} = \left(\frac{^{232}\text{Th}}{^{238}\text{U}} \right) \cdot \left(\frac{e^{\lambda_{232}t_i} - 1}{e^{\lambda_{238}t_i} - 1} \right) \quad (6)$$

where t_i is the uncorrected date in years. Then, the radiogenic component, the $^{206}\text{Pb}^*/^{238}\text{U}$ ratio, can be calculated as

$$^{206}\text{Pb}^*/^{238}\text{U} = (1 - f_{206}) \cdot (^{206}\text{Pb}/^{238}\text{U}_{\text{measured}}) \quad (7)$$

Finally, the ^{208}Pb -corrected date ($^{206}\text{Pb}^*/^{238}\text{U}$ date) is calculated by solving the age equation with the $^{206}\text{Pb}^*/^{238}\text{U}$ ratio:

$$t_{206} = \frac{1}{\lambda_{238}} \cdot \ln \left(\frac{^{206}\text{Pb}^*}{^{238}\text{U}} + 1 \right) \quad (8)$$

where t_{206} is the corrected age in years. The final corrected date is calculated iteratively—calculate the date, whereby each iteration replaces t_i with the previously calculated $^{206}\text{Pb}^*/^{238}\text{U}$ date. The final ^{208}Pb -corrected date presented here is from the two hundredth iteration. For our dataset, we varied the initial age estimate, and therefore the initial common Pb composition, from 1 Ma to 1000 Ma and, by the fifth iteration, the error, the resulting ^{208}Pb -corrected date differs by less than 0.05% for 98% of the unknowns. The uncertainty on the date is calculated as the equivalent of the percent error (propagated) uncertainty of the uncorrected $^{206}\text{Pb}/^{238}\text{U}$ date ratio (Odlum et al., 2019).

2.3.24 ^{207}Pb Correction

The ^{207}Pb correction method is based on a linear regression of $^{207}\text{Pb}/^{206}\text{Pb}$ and $^{238}\text{U}/^{206}\text{Pb}$ in Tera-Wasserburg space (Tera and Wasserburg, 1972) along a two-component mixing line between non-radiogenic and radiogenic Pb (Faure, 1986; Figure 1). This method is most powerful for eogenetic-co-genetic minerals because it does not require knowing $^{207}\text{Pb}/^{206}\text{Pb}_{\text{common}}$. Yet, because eogenetic-co-genetic analyses are inherently unknown in detrital samples, the routine used here calculates the common Pb component of each individual analysis using the Stacey and Kramers (1975) two-stage Pb evolution model and an initial age estimate. We explore using an initial date estimate from the uncorrected date (t_i) and from the ^{208}Pb -corrected date (t_{208}). The intersection of the discordia with the concordia curve, anchored by $^{207}\text{Pb}/^{206}\text{Pb}_{\text{common}}$, is the radiogenic $^{207}\text{Pb}/^{206}\text{Pb}^*$. To find the intersection, we use the Schwarz intersection function in MATLAB. The ^{207}Pb -corrected $^{207}\text{Pb}/^{206}\text{Pb}^*$ and $^{206}\text{Pb}^*/^{238}\text{U}$ dates are calculated from $^{207}\text{Pb}/^{206}\text{Pb}^*$ and $^{206}\text{Pb}^*/^{238}\text{U}$, respectively. Note that because the correction forces intersection with the concordia, the two dates are identical. Discordance is calculated in Tera-Wasserburg space, where the percent discordance is defined as the distance between the measured $^{238}\text{U}/^{206}\text{Pb}$ and $^{207}\text{Pb}/^{206}\text{Pb}$ coordinates and the concordia intersection (δ_2) along the total discordia line distance ($\delta_1 + \delta_2$):

Formatted: Font: +Headings (Times New Roman), Not Italic

Formatted: Font: +Headings (Times New Roman), Bold

Formatted: Font: +Headings (Times New Roman), Not Italic

Formatted: Font: +Headings (Times New Roman), Bold

Formatted: Font: +Headings (Times New Roman)

Formatted: Font: +Headings (Times New Roman)

Formatted: Font: +Headings (Times New Roman), Not Italic

Formatted: Font: +Headings (Times New Roman), Bold, Not Italic

Formatted: Font: +Headings (Times New Roman), Not Italic

Formatted: Font: +Headings (Times New Roman), Bold

Formatted: Font: +Headings (Times New Roman)

Formatted: Font: +Headings (Times New Roman)

Formatted: Centered

Formatted: Font: +Headings (Times New Roman), Bold

Formatted: Font: +Headings (Times New Roman), Not Italic

Formatted: Font: +Headings (Times New Roman), Bold

Formatted: Font: +Headings (Times New Roman)

Formatted: Indent: First line: 0"

Formatted: Font: +Headings (Times New Roman)

Formatted: Font: +Headings (Times New Roman)

Formatted: Font: +Headings (Times New Roman)

Formatted: Font: +Headings (Times New Roman)

Formatted: Font: +Headings (Times New Roman)

Formatted: Font: +Headings (Times New Roman)

Formatted: Font: +Headings (Times New Roman)

Formatted: Font: +Headings (Times New Roman)

Formatted: Font: +Headings (Times New Roman)

Formatted: Font: +Headings (Times New Roman)

Formatted: Font: +Headings (Times New Roman)

Formatted: Font: +Headings (Times New Roman)

Formatted: Font: +Headings (Times New Roman)

Formatted: Font: +Headings (Times New Roman)

Formatted: Font: +Headings (Times New Roman)

Formatted: Font: +Headings (Times New Roman)

Formatted: Font: +Headings (Times New Roman)

Formatted: Font: +Headings (Times New Roman)

The Concordance = $\delta_1 / (\delta_1 + \delta_2)$

This version of discordance, when applied with a stricter filter, is more forgiving for dates younger than 1000 Ma where the slope of the concordia curve is shallow.

Like the ^{208}Pb correction method, the ^{207}Pb correction method assumes U-Pb concordance and no Pb loss, but, unlike the ^{208}Pb correction, does not assume an undisturbed U/Th ratio. Because Pb loss is not considered, all calculated/corrected dates are obtained from lower intercepts are (possibly) minimum ages. The methods/equations given here are modified for detrital samples with unknown eogenetic-co-genetic minerals based on methods previously described in Faure (1986), Williams (1997), Chew et al. (2011), and the semitotal-Pb/U scheme of Ludwig (1998) and Vermeesch (2020).

We illustrate the calculation is similar to the difference between these different ^{208}Pb correction methods and, first, the proportion of $^{206}\text{Pb}_{\text{common}}$ is calculated as

$$f_{206} = \frac{(^{207}\text{Pb}/^{206}\text{Pb}_{\text{measured}}) - (^{207}\text{Pb}^*/^{206}\text{Pb}^*)}{(^{207}\text{Pb}/^{206}\text{Pb}_{\text{common}}) - (^{207}\text{Pb}^*/^{206}\text{Pb}^*)} \quad (10)$$

where $^{207}\text{Pb}/^{206}\text{Pb}_{\text{measured}}$ is taken directly from the raw data. The $^{207}\text{Pb}/^{206}\text{Pb}_{\text{common}}$ ratio is based on the two-stage Pb evolution model of Stacey and Kramers (1975), which is calculated as the ratio of Equation (3) and Equation (11) for dates older than 3.7 Ga or as the ratio of Equation (5) and Equation (12) for dates younger than 3.7 Ga:

$$\left(\frac{^{207}\text{Pb}}{^{206}\text{Pb}}\right)_{\text{common}} = \frac{7.19}{137.88} \cdot (e^{\lambda_{235} \cdot 4.57 \times 10^9} - e^{\lambda_{235} \cdot t_i}) + 10.294 \quad (11)$$

or

$$\left(\frac{^{207}\text{Pb}}{^{204}\text{Pb}}\right)_{\text{common}} = \frac{9.74}{137.88} \cdot (e^{\lambda_{235} \cdot 3.7 \times 10^9} - e^{\lambda_{235} \cdot t_i}) + 12.998 \quad (12)$$

where t_i is the initial date estimate in years and the ^{235}U decay rate λ_{235} is $9.8485 \times 10^{-10} \text{ yr}^{-1}$ (Faure, 1986). Here, for t_i we use the $^{206}\text{Pb}/^{238}\text{U}$ date from the iolite data reduction. However, Chew et al. (2011) demonstrated that the choice of initial date results in a $< 0.05\%$ difference in the final ^{207}Pb -corrected date after 5 iterations. The expected radiogenic $^{207}\text{Pb}/^{206}\text{Pb}^*$ ratio is calculated as

$$\frac{^{207}\text{Pb}^*}{^{206}\text{Pb}^*} = \left(\frac{^{235}\text{U}}{^{238}\text{U}}\right) \cdot \left(\frac{e^{\lambda_{235} t_i} - 1}{e^{\lambda_{238} t_i} - 1}\right) \quad (13)$$

where $^{235}\text{U}/^{238}\text{U}$ is 137.88 (Steiger and Jäger, 1977). Finally, the radiogenic component, the $^{206}\text{Pb}^*/^{238}\text{U}$ ratio, can be calculated using Equation (8) and then used to solve the age equation (Equation (9) issue raised by low U screening). As with the ^{208}Pb correction, to iteratively calculate the date, each iteration replaces t_i with the previously calculated $^{206}\text{Pb}^*/^{238}\text{U}$ date. The ^{207}Pb -corrected date presented here is from the two hundredth iteration. The uncertainty on the

Formatted: Font: +Headings (Times New Roman)

Formatted: Font: +Headings (Times New Roman)

Formatted: Font: +Headings (Times New Roman)

Formatted: Font: +Headings (Times New Roman)

Formatted: Font: +Headings (Times New Roman)

Formatted: Font: +Headings (Times New Roman)

Formatted: Font: +Headings (Times New Roman)

Formatted: Font: +Headings (Times New Roman)

Formatted: Font: +Headings (Times New Roman)

Formatted: Font: +Headings (Times New Roman)

Formatted: Font: +Headings (Times New Roman)

Formatted: Font: +Headings (Times New Roman)

Formatted: Font: +Headings (Times New Roman)

Formatted: Font: +Headings (Times New Roman)

Formatted: Font: +Headings (Times New Roman)

Field Code Changed

Formatted: Font: +Headings (Times New Roman)

Formatted: Font: +Headings (Times New Roman)

Formatted: Font: +Headings (Times New Roman)

Formatted: Font: (Default) +Headings (Times New Roman), Not Italic, Do not check spelling or grammar

Formatted: Font: (Default) +Headings (Times New Roman), Do not check spelling or grammar

Formatted: Font: (Default) +Headings (Times New Roman)

Formatted: Font: (Default) +Headings (Times New Roman)

Formatted: Font: (Default) +Headings (Times New Roman)

Formatted: Font: (Default) +Headings (Times New Roman)

Formatted: Font: (Default) +Headings (Times New Roman)

Formatted: Font: (Default) +Headings (Times New Roman)

Formatted: Font: (Default) +Headings (Times New Roman)

Formatted: Font: (Default) +Headings (Times New Roman)

Formatted: Font: (Default) +Headings (Times New Roman)

Formatted: Font: (Default) +Headings (Times New Roman)

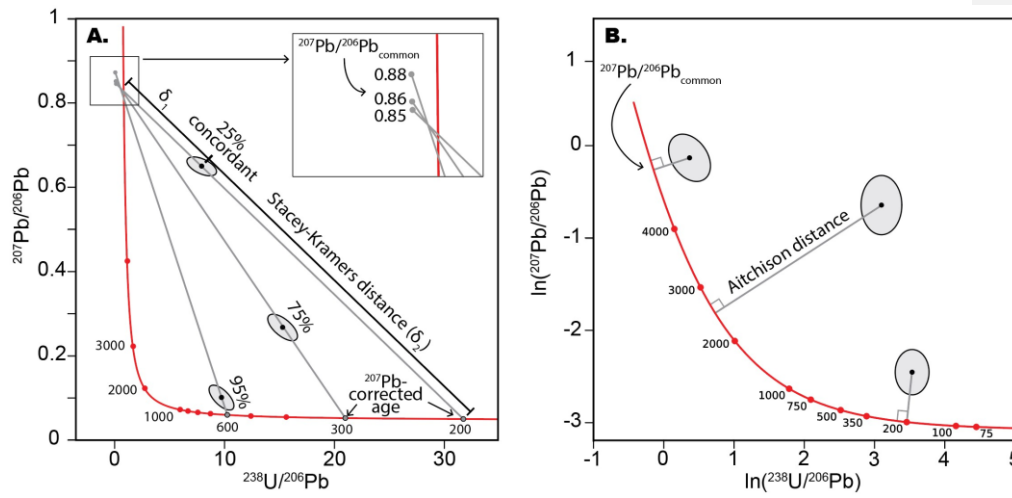
Formatted: Font: (Default) +Headings (Times New Roman)

Formatted: Font: (Default) +Headings (Times New Roman)

Formatted: Font: (Default) +Headings (Times New Roman), Do not check spelling or grammar

Formatted: Font: +Headings (Times New Roman)

date is calculated as the equivalent of the percent (propagated) uncertainty of the uncorrected $^{206}\text{Pb}/^{238}\text{U}$ ratio (Odlum et al., 2019). For example, if the initial $^{206}\text{Pb}/^{238}\text{U}$ ratio has 2% uncertainty at 2 sigma and the corrected date is 200 Ma, then the corrected date uncertainty is ± 4 Ma (2s).



355 *Figure 1. Conceptual schematics of the ^{207}Pb correction and Stacey-Kramers distance (A) and Aitchison distance (B). (A) For the ^{207}Pb correction, first, the common $^{207}\text{Pb}/^{206}\text{Pb}$ ratio is calculated from the initial date estimate (t_i). Next, a discordia is fitted between $^{207}\text{Pb}/^{206}\text{Pb}_{\text{common}}$ and the data point. Then, the lower intersection of the line with the concordia marks the corrected $^{238}\text{U}/^{206}\text{Pb}$ and $^{207}\text{Pb}/^{206}\text{Pb}$, which are used to calculate the ^{207}Pb -corrected date. The Stacey-Kramers distance defines concordance as the distance between the upper and lower intersections of the discordia with the concordia (Equation (14)). (B) The Aitchison distance calculates the Euclidean distance between the analysis and concordia curve in log-ratio space, where higher distance values are considered more discordant. Figure modified from Vermeesch (2021).*

2.3.5 Discordance

365 Although there are various ways to calculate the discordance of U-Pb analyses, which are reviewed elsewhere (e.g., Vermeesch, 2021), it remains unclear which metric is best for common Pb bearing minerals and if a discordance threshold should be applied. One family of discordance metrics relies on the difference between the $^{206}\text{Pb}/^{238}\text{U}$ date and $^{207}\text{Pb}/^{206}\text{Pb}$ date (e.g., Gehrels, 2011). Because ^{207}Pb and ^{208}Pb corrections force concordance, these metrics are not applicable to common Pb bearing minerals. Two metrics potentially relevant to common Pb-bearing minerals are the Stacey-Kramers distance and Aitchison distance (after Vermeesch, 2021). The Stacey-Kramers distance is calculated by first using the U-Pb analysis and $^{207}\text{Pb}/^{206}\text{Pb}_{\text{common}}$ composition (calculated during common Pb correction) to find the discordia in Tera-Wasserburg space, then discordance is calculated as the distance between the measured $^{238}\text{U}/^{206}\text{Pb}$ and $^{207}\text{Pb}/^{206}\text{Pb}$ coordinates and the concordia intersection (δ_2) along the total discordia distance ($\delta_1 + \delta_2$) (Figure 1; Vermeesch, 2021):

$$\text{Concordance} = \delta_1 / (\delta_1 + \delta_2) \quad (14)$$

If a discordance threshold is applied, the Stacey-Kramers distance approach includes more young dates than old dates (> 1000 Ma) due to the change in concordia slope around 1000 Ma (Vermeesch, 2021). A second metric is the Aitchison distance (Aitchison, 1982; Pawlowsky-Glahn et al., 2015) which calculates the Euclidean distance from the measured $^{238}\text{U}/^{206}\text{Pb}$ and $^{207}\text{Pb}/^{206}\text{Pb}$ coordinates to the concordia line in log-ratio Tera-Wasserburg space (Figure 1; Vermeesch, 2021). We compare these two metrics with our new dataset. Additionally, detrital zircon studies commonly use a discordance threshold that excludes analyses with discordance above 5-30%, typically around 10% (Spencer et al., 2016), which can induce bias (Nemchin and Cawood, 2005; Malusà et al., 2013). The application of a discordance threshold has been underexplored in detrital rutile, with most studies applying no discordance filter, perhaps due to the lack of consensus on how to define discordance in common Pb bearing minerals. Rather, a group of studies proposes to filter analyses based on the percent uncertainty of the corrected date (Mark et al., 2016; Govin et al., 2018; Chew et al., 2020; Caracciolo et al., 2021) a new dataset from Anatolia. It is noted that there is little guidance on how uncertainties are calculated and propagated during Pb correction, which ought to be investigated in future work; meanwhile, the filters should be applied with care. We explore these thresholds with our new dataset.

Formatted: Indent: First line: 0"

Formatted: Font: +Headings (Times New Roman)

3. Geologic Context

Anatolia is composed of a series of subduction complexes, island arcs, and continental terranes that accreted and collided from the Late Paleozoic through Cenozoic during the progressive opening and closing of Paleotethys and Neotethys seaways (Şengör and Yilmaz, 1981). Today, northwestern Anatolia comprises, from structurally highest (north) to lowest (south), the continental Pontides, including the Cretaceous–Eocene forearc-to-foreland Central Sakarya and Sarıcakaya Basins, the Permian–Triassic Karakaya Complex, the İzmir–Ankara–Erzincan suture zone and associated Neotethys ophiolites and mélange, and the lower plate Anatolide–Tauride continental terranes (Figure 2). The Pontides basement contains Paleozoic paragneiss, schist, and amphibolite rocks intruded by Carboniferous granitoids emplaced during the Variscan orogeny (Göncüoğlu et al., 2000; Ustaömer et al., 2012). The nature of the Karakaya Complex is debated but is generally considered a subduction-accretion complex associated with the Late Paleozoic–Early Mesozoic closure of the Paleotethys along the southern margin of Eurasia (Pickett and Robertson, 1996; Okay and Göncüoğlu, 2004; Federici et al., 2010; Ustaömer et al., 2016). The Karakaya Complex contains metamafic and metasedimentary rocks interpreted as seamounts of intra-oceanic basaltic composition and forearc basin and trench deposits (Pickett and Robertson, 1996) that were subsequently metamorphosed to blueschist and epidote-amphibolite with minor eclogite facies with estimated temperatures of $340\text{--}550 \pm 50$ °C (Okay et al., 2002; Federici et al., 2010) with phengite, glaucophane, and barrosite Ar–Ar cooling dates around $200\text{--}215$ Ma (Okay et al., 2002). The youngest Karakaya Complex units are unmetamorphosed or metamorphosed to zeolite to lower greenschist facies ($120\text{--}376$ °C) (Federici et al., 2010) and are unconformably overlain by Jurassic platform carbonates. The Cretaceous to present closure of the Neotethys and associated suturing is recorded in the Central Sakarya and Sarıcakaya Basins located north of the suture. Stratigraphic and paleocurrent (Ocaköğlü et al., 2018), provenance (Mueller et al., 2022; Campbell et al., 2023), and mudstone geochemistry records (Açıkalin et al., 2016) show the input of suture zone derived material into the Central Sakarya Basin from the Late Cretaceous through Eocene, interpreted as progressive suture zone uplift and exhumation during accretion and continental collision

Formatted: Font color: Black, English (United Kingdom)

Formatted: Font: +Headings (Times New Roman), 10 pt

Formatted: Font: +Headings (Times New Roman), 10 pt

Formatted: Font: +Headings (Times New Roman)

Formatted: Font: +Headings (Times New Roman), 10 pt

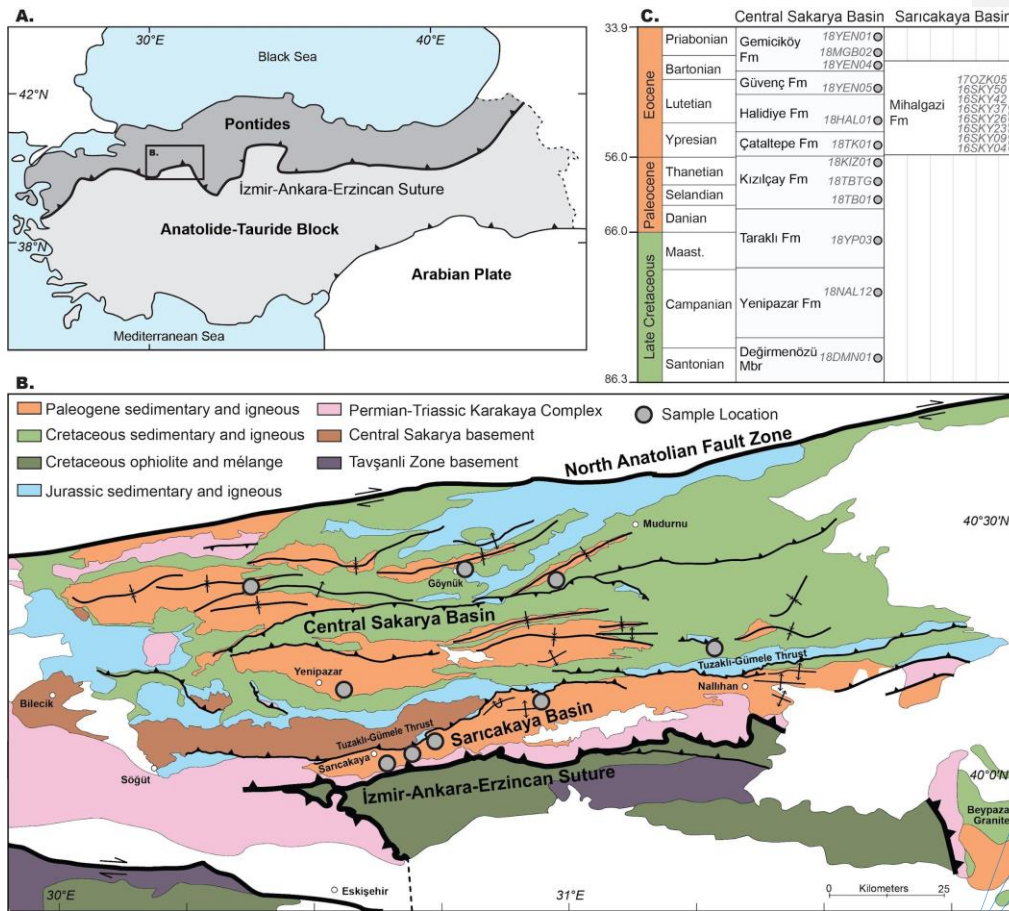
Formatted: Font: +Headings (Times New Roman), 10 pt

Formatted: Font color: Black, English (United Kingdom)

Formatted: Font color: Black, English (United Kingdom)

(Ocakoğlu et al., 2018; Okay et al., 2020; Mueller et al., 2022; Campbell et al., 2023). Cretaceous subduction-related arc volcanism and Paleogene syn-collisional volcanic centers are located within and to the north of the basins (Kasapoğlu et al., 2016; Ersoy et al., 2017, 2023; Keskin and Tüysüz, 2018). By Eocene times, continued collision increased plate coupling which manifested as increased contractional deformation that partitioned the southern Central Sakarya Basin into the Sarıcakaya Basin along the basement-involved Tuzaklı-Gümele Thrust (also termed the Sögüt Thrust or Nallıhan Thrust) (Mueller et al., 2022). The Eocene Sarıcakaya Basin received sediment from the suture zone and Karakaya Complex to the south and basement-involved thrust sheets to the north (Mueller et al., 2019).

415



420

Figure 2: (A) Simplified terrane map of Anatolia and (B) geologic map of the Central Sakarya Basin and Sarıcakaya Basin region (after Aksay et al., 2002). (C) Simplified stratigraphic correlation chart and schematic sample distribution. Stratigraphy after Ocakoğlu et al. (2018).

- Formatted: Font: (Default) +Headings (Times New Roman), English (United Kingdom)
- Formatted: Font: +Headings (Times New Roman), Bold
- Formatted: Font: +Headings (Times New Roman)
- Formatted: Font: +Headings (Times New Roman), Bold
- Formatted: Font: +Headings (Times New Roman)
- Formatted: Font: +Headings (Times New Roman), Bold
- Formatted: Font: +Headings (Times New Roman)
- Formatted: Default Paragraph Font, Font: (Default) +Headings (Times New Roman), Bold

4 Methods

4.1 Sample Information

425 Sedimentary rock samples were collected from Upper Cretaceous to Eocene siliciclastic sedimentary rocks
of sections in the Central Sakarya Basin and Sarıcakaya Basin in western Anatolia (Figure 2; Table S2S1). Detrital
zircon U-Pb ages and Hf isotopes from these samples are already published (cf. Section 8; Mueller et al., 2019, 2022;
Campbell et al., 2023); a set of 20 samples were chosen for detrital rutile U-Pb dating and trace element analysis.
Heavy minerals were extracted using standard heavy mineral techniques, including crushing, water table, heavy liquid,
430 and magnetic separation (Appendix A; see supporting information). Rutile grains were handpicked; all rutile grains
were picked from most the >0.3 amp. magnetic fraction using a Leica M205C binocular microscope. Three samples,
except for samples 16SKY26, 16SKY42 and 17OZK05 for which yielded hundreds of rutile grains and we
handpicked 260–320 rutile grains were selected from each sample; for samples with smaller yield, all grains were
picked. The low yield of rutile grains partially contributes to the low-*n* date distributions of the individual samples.
435 Rutile grains were mounted in epoxy and polished to expose the internal structure. Then, rutile mounts were
carbon coated and imaged with a TFS Apreo-S with Lovac SEM with an energy-dispersive detector (EDS) to
distinguish TiO₂ grains from other heavy minerals (Figure A4S1).

4.2 U-Pb Analytical Protocol

440 Detrital rutile U-Pb geochronology was conducted at the Isotope Geochemistry Lab at the University of
Kansas (KU-IGL) using a Thermo Element2 magnetic sector field ICP-MS coupled to a Photon Machines AnalyteG2
excimer laser ablation system. The protocol was modified from Rösel et al. (2019) to optimize for low U contents
(Appendix A Text S1; Table A2S2). The ICP-MS was manually tuned using NIST SRM 612 reference material glass
to yield Th/U ratios close to 0.8 optimize for high sensitivity, and low oxide production rates while maintaining high
²³⁸U sensitivity. Grains were ablated for 25 seconds with a laser beam diameter of 50 μm, laser fluence of 3.0 J/cm²,
445 and 10 Hz repetition rate. The U-Pb data were collected in 4 analytical sessions. The analytical protocol was modified
from session to session to optimize for the analysis of low U and Pb unknowns and high U and Pb reference materials.
In the first two analytical sessions, 21RtF and 21RtG, Pb and Th isotopes were measured with the secondary electron
multiplier operated operating in counting detection mode, whereas Pb and Th isotopes were measured with the
secondary electron multiplier in both counting and analog modes ('both mode') to handle both the high U counts in
450 the standards and low U counts in the unknowns for the final two sessions, 21RtA and 21RtB. Primary and secondary
reference materials were the R10 (1091.6 ± 3.5 Ma by TIMS, 2s abs.; Luvizotto et al., 2009), Wodgina (2845.8 ± 7.8
Ma by TIMS; Ewing, 2011), 9826J (381.9 ± 1.1 Ma by TIMS; Kylander-Clark, 2008), LJ04-08 (498 ± 3 Ma by LA-
ICP-MS; Apen et al., 2020), and Kragerø (1085.7 ± 7.9 Ma by TIMS; Kellett et al., 2018). For U-Pb analyses, the
analysis of 5–8 unknowns was followed by 2 standards, respectively the primary standard R10 and one of the secondary
455 standards. The data were reduced in iolite 4 (Paton et al., 2011), calibrated against R10. The protocols uncorrected for
initial Pb, and using the weighted linear fit drift correction which reproduced the published secondary standard ages
of the and brought their MSWDs closest to 1. The concordia ages are satisfactory for all reference materials, except
for the Wodgina and Kragerø, which did not perform well during the first two analytical sessions—likely due to ²⁰⁶Pb

Formatted: Font: +Headings (Times New Roman)

Formatted: Font: +Headings (Times New Roman), Font color: Black

Formatted: Font: +Headings (Times New Roman), Font color: Black

Formatted: Normal, Indent: First line: 0.5", Border: Top: (No border), Bottom: (No border), Left: (No border), Right: (No border), Between : (No border)

Formatted: Font: +Headings (Times New Roman), Font color: Black

Formatted: Font: +Headings (Times New Roman)

Formatted: Font: +Headings (Times New Roman)

Formatted: Font: +Headings (Times New Roman)

Formatted: Font: +Headings (Times New Roman)

Formatted: Font: +Headings (Times New Roman)

Formatted: Font: +Headings (Times New Roman)

Formatted: Font: +Headings (Times New Roman)

Formatted: Font: +Headings (Times New Roman)

Formatted: Font: +Headings (Times New Roman), 10 pt, Font color: Auto, Pattern: Clear

Formatted: Font: +Headings (Times New Roman)

Formatted: Font: +Headings (Times New Roman)

Formatted: Font: +Headings (Times New Roman)

Formatted: Font: +Headings (Times New Roman), Font color: Black

Formatted: Font: +Headings (Times New Roman), Font color: Black

Formatted: Font: +Headings (Times New Roman), Font color: Black

Formatted: Font: +Headings (Times New Roman)

Formatted: Font: +Headings (Times New Roman)

Formatted: Font: +Headings (Times New Roman)

Formatted: Font: +Headings (Times New Roman)

Formatted: Font: +Headings (Times New Roman)

Formatted: Font: +Headings (Times New Roman)

Formatted: Font: +Headings (Times New Roman)

Formatted: Font: +Headings (Times New Roman)

Formatted: Font: +Headings (Times New Roman)

Formatted: Font: +Headings (Times New Roman)

Formatted: Font: +Headings (Times New Roman)

Formatted: Font: +Headings (Times New Roman)

Formatted: Font: +Headings (Times New Roman)

Formatted: Font: +Headings (Times New Roman)

Formatted: Font: +Headings (Times New Roman)

Formatted: Font: +Headings (Times New Roman)

Formatted: Font: +Headings (Times New Roman)

460 counts per second exceeding the limit of linear behavior in counting detection mode—and are discarded from those analytical sessions. Standard reproducibility is discussed further in the supplemental text included in the data repository; U-Pb data are provided in the data repository (Mueller et al., 2023).

4.3 Trace Element Geochemistry Analytical Protocol

465 Detrital rutile trace element geochemistry (^{49}Ti , ^{51}V , ^{53}Cr , ^{66}Zn , ^{69}Ga , ^{90}Zr , ^{93}Nb , ^{95}Mo , ^{118}Sn , ^{121}Sb , ^{177}Hf , ^{181}Ta , ^{182}W) was conducted at the KU-IGL using the same instrumentation and parameters, except with a 25 or 35 μm spot size. Reference materials included USGS GSD-1G and USGS GSC-1G glasses (Jochum et al., 2011) and R10 rutile (Luvizotto et al., 2009). For trace element analysis, the analysis of 5–10 unknowns was followed by analysis of 2 standards, the primary standard GSD-1G and one of the secondary standards. Trace element concentrations were calculated using the Trace Element routine in iolite 4 with ^{49}Ti as an internal standard; for rutile unknowns, TiO_2 was set to be 100 mass-% (e.g., Plavsá et al., 2018; Rösel et al., 2019). Standard reproducibility is discussed in the supporting information in the data repository (Text S2). In short, for the secondary standard GSC-1G, all elements are within 10% of the published values except for Sn and Ga, and for the secondary standard R10, all results are within the range of reported values. Following U-Pb and trace element analysis, mounts were imaged in an SEM at University of Nevada Reno (

470 Figure 3). Most grains have both U-Pb and trace element results, but some grains have only U-Pb results due to the grains being too small for a second ablation spot or only trace element results due to discarded U-Pb data. Detrital rutile trace element data are given in the data repository (Mueller et al., 2023).

4.4 Additional Data Workflows

480 Additional data reduction and data calculations steps were performed. Provided as a complement to this manuscript are open access Jupyter Notebooks that contain the Python and R code used to perform these additional calculations and to generate figures, which are briefly described here (Mueller, 2024). (1) The ^{208}Pb and ^{207}Pb corrections were performed in the Detrital-Common-Pb-Corrections notebook using the equations detailed in Section 2 above. The notebook allows for either a manually set number of iterations or to iterate until all analyses are below a given threshold—the percent difference in corrected date between the current and previous iteration. Presented here are the results from the 200th iteration. (2) The UPb-Plotter notebook visualizes the uncorrected U-Pb results in Tera-Wasserburg space, compares metrics for excluding analyses based on uncertainty filters (Section 5.3), and calculates discordance using the Stacey-Kramers and Aitchison distances (Section 2; Figure 1). (3) The Rutile-Trace-Elements notebook includes the calculations and resulting figures for exploring TiO_2 polymorphs, mafic and pelitic protoliths, Zr-in-rutile thermometry, and low U contents. Here, rutile grains are classified as mafic or pelitic based on the Cr-Nb discrimination fields of Triebold et al. (2012), and Zr-in-rutile temperatures are calculated with the Kohn (2020) formulation (Equation 1) at 13 kbar. (4) The Detrital-PCA-R notebook performs principal component analysis on trace element data using the `pcaCoDa` function in the `robCompositions` library, which is designed to handle compositional data (Templ et al., 2011) to 5% or better (Figure A2). Due to the variable performance of Sn and Ga in the secondary standards, these elements were excluded from the PCA (Supplemental Text S2, Figure S6).

Formatted: Font: +Headings (Times New Roman)

Formatted: Font: (Default) +Headings (Times New Roman), Do not check spelling or grammar

495 Additionally, Mo and Sb were excluded because grains with very low or zero concentrations influence the results to be artificially dominated by these elements. (5) Additionally, the UPb-Timeseries notebook is provided for visualizing U-Pb timeseries data.

5 U-Pb Geochronology Results

5.1 U-Pb Data Quality

500 A total of 1,278 detrital rutile grains were analyzed for U-Pb geochronology. A significant number of analyses were rejected and excluded, as discussed below. We aim to be transparent in data reporting—including the number of grains analyzed and the criteria for rejection—in order to give precedence for this practice, which is missing in the literature, and to explore the current limitations of large-*n* detrital rutile studies. Even with the modified optimized LA-ICP-MS protocol, a significant number of analyses did not meet quality control goals: 686 of 1,278 (54%) analyses were excluded due to anomalous (spiky) patterns in raw signal intensity, or low U or low Pb signal intensity. Figure 3 and a further 214 analyses were excluded for $^{207}\text{Pb}/^{206}\text{Pb}$ error above 20%, leaving 378 analyses remaining (30%). Figure 3 depicts representative examples of signal intensity in accepted and rejected analyses. Inclusions and anomalous patterns were easily spotted through monitoring ^{206}Pb , ^{207}Pb , ^{238}U , ^{232}Th , $^{206}\text{Pb}/^{238}\text{U}$ and $^{207}\text{Pb}/^{206}\text{Pb}$ channels. In some instances, the signal of an inclusion or anomalous (spiky) pattern was short enough that the integration window could be shortened to exclude it. In other cases, the non-inclusion signal could not be isolated and the entire analysis was discarded. Potential causes for these abnormal signal patterns and high Pb error uncertainty include (1) elemental heterogeneity from ablating into small inclusions and/or lamellae; (2) inhomogeneities due to micro-cracks with different element/isotope composition; (3) heterogeneous amount of common lead incorporation during rutile growth; (4) textural and/or elemental heterogeneities due to multiple rutile growth events. Although, scenarios 3 and 4 are unlikely for Pb because it diffuses and should not cause spikes. Detrital rutile U-Pb raw data are given in the data repository.

515 The SEM images do not give a clear picture of how to better select grains that will produce acceptable signal intensity and U-Pb concordance.

Figure 3 shows SEM images of representative rutile grains after laser ablation. All grains appeared inclusion-free before ablation, yet some analyses clearly ablated into inclusions (

520 Figure 3b,e). The large laser spot size of 50 μm gives a higher signal, which is better for grains with potentially low U or low Pb concentrations, but the potential trade-off is increasing the likelihood of hitting inclusions. Grains with obvious inclusion lamellae generally yielded poor data quality.

Formatted: Normal, Indent: First line: 0.5", Border: Top: (No border), Bottom: (No border), Left: (No border), Right: (No border), Between : (No border)

Formatted: Font: +Headings (Times New Roman), Font color: Black

Formatted: Font: +Headings (Times New Roman), Font color: Black

Formatted: Font: +Headings (Times New Roman), Font color: Black

Formatted: Font: +Headings (Times New Roman), Font color: Black

Formatted: Font: +Headings (Times New Roman), Font color: Black

Formatted: Font: +Headings (Times New Roman), Font color: Black

Formatted: Font: +Headings (Times New Roman), Font color: Black

Formatted: Font: +Headings (Times New Roman), Font color: Black

Formatted: Font: +Headings (Times New Roman), Font color: Black

Formatted: Font: +Headings (Times New Roman), Font color: Black

Formatted: Font: +Headings (Times New Roman), Font color: Black

Formatted: Font color: Black

Formatted: English (United States)

Formatted: Font color: Dark Red, English (United States)

Formatted: English (United States)

Formatted: Font color: Black

Formatted: Font color: Black

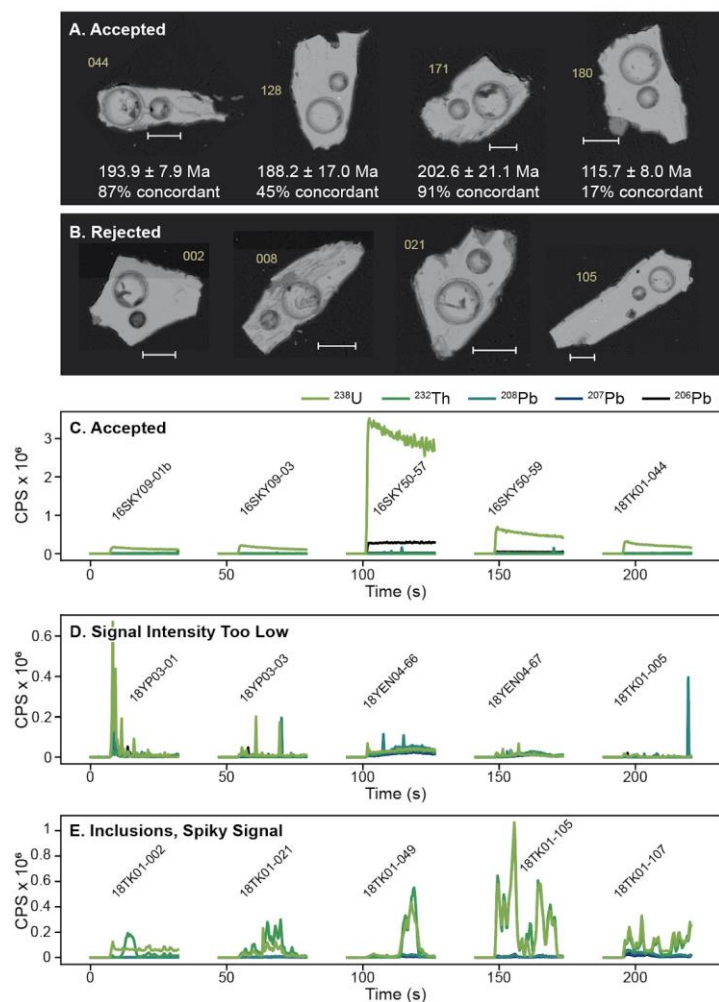


Figure 3(Figure 3C). Grains with clear inclusion lamellae yielded poor data quality (Figure 3B).

525 **4.3 Trace Element Geochemistry Analytical Protocol**

Detrital rutile trace element geochemistry (^{40}Ti , ^{54}V , ^{53}Cr , ^{66}Zn , ^{60}Ga , ^{90}Zr , ^{93}Nb , ^{95}Mo , ^{118}Sn , ^{124}Sb , ^{127}Hf , ^{184}Ta , ^{182}W) was conducted at the KU IGL using the same instrumentation and parameters, except with a 25 or 35 μm spot size. Reference materials included USGS GSD 1G and GSC 1G glasses and R10 rutile. Trace element concentrations were calculated using the Trace Element routine in iolite 4 with ^{49}Ti as an internal standard; for rutile unknowns, TiO_2 was set to be 100 mass %. Following U-Pb and trace element analysis mounts were imaged in an

530

SEM at University of Nevada Reno (). Most grains have both U-Pb and trace element results, but some grains have only U-Pb results due to the grain size being too small for a second ablation spot or have only trace element results due to discarded U-Pb data. Detrital rutile trace element raw data are given in the data repository.

5.1 U-Pb Results

5.1 Influence of Pb Corrections on Date Spectra

All the U-Pb results are displayed together in Figure 4 in Tera-Wasserburg space. A substantial number of analyses plot close to non-radiogenic common Pb values. This is evident in the convergence of data toward y-intercept values close to known common Pb values: from 1000 Ma to present, the $^{207}\text{Pb}/^{206}\text{Pb}_{\text{common}}$ ratio evolves from ~0.88 to 0.83. Therefore, this section explores the sensitivity of U-Pb date spectra to ^{208}Pb and ^{207}Pb correction methods and to discordance filters in order to determine whether these factors change the overall provenance interpretations.

The uncorrected and corrected data are shown in as kernel density estimates (KDEs) and cumulative distributions. Resulting date distributions for each sample are shown in Figure A3, but due to small sample sizes, interpretations are based on the cumulative dataset. Within each common Pb correction method, the results are subdivided by concordance (see Figure 4). For the ^{207}Pb corrections, concordance is defined in Tera-Wasserburg space. For the sake of comparison, the 100–40% concordant group for the ^{208}Pb correction excludes the same grains that are categorized as 40–0% concordant in the $^{207}\text{Pb}_i$ correction. The 100–80%, 80–60%, and 60–40% concordance groups have modes centered around 95 Ma, 190 Ma, 310 Ma, and 580 Ma. The uncorrected, ^{208}Pb corrected with no concordance filter, and 40–0% concordance groups have broad date peaks with poorly defined date modes.

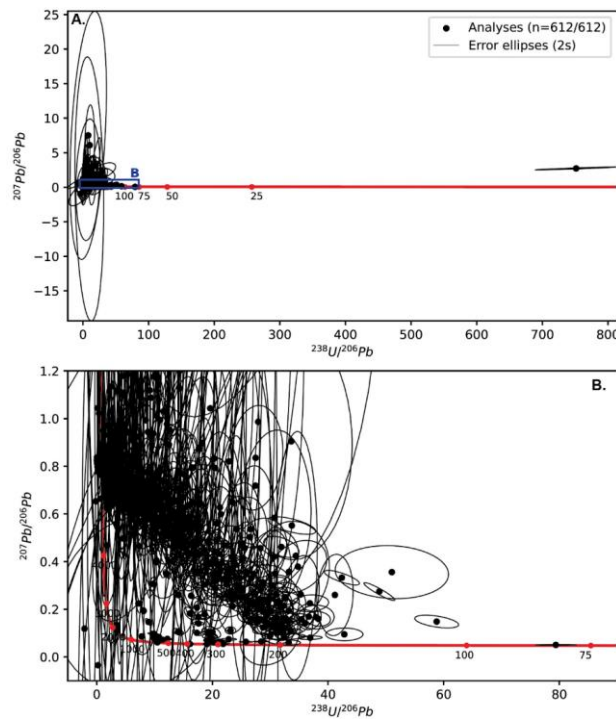
The different common Pb corrections produce differences in peak amplitude, the percent concordance has a larger impact on overall date distribution (). The date difference between the ^{207}Pb corrected dates using t_c and t_{208} is less than 1% for analyses less than 60% concordant and less than 5% for analyses 60–40% concordant (). The difference in date significantly increases for grains that are less than 40% concordant. This result is replicated in statistical comparisons included in the data repository (i.e., similarity, likeness, cross correlation, Kolmogorov-Smirnov). For this reason, we prefer the date distributions that include all grains 100–40% concordant, excluding grains below 40% concordant. However, the similarity in the ^{207}Pb with t_{208} cumulative date distribution for the 100–40% and 40–0% groups is notable, which could warrant the inclusion of those low concordance grains. Ultimately, the prominent date modes are the same across ^{207}Pb and ^{208}Pb corrected groups, meaning that provenance interpretations are not affected by the choice of Pb correction method. This may not be the case for other datasets where the Pb correction method and concordance filter may influence the final date distribution and in cases where the KDE amplitude is important.

5.2 Influence of Low-U Rutile on Age Spectra

A common analytical workflow for detrital rutile is to first analyze trace elements then only collect U-Pb data on rutile above a given U concentration threshold. Elemental concentrations are calculated based on the measured count rate

565 (i.e., counts per second, CPS), which is inherently dependent on the individual mass spectrometer and laser ablation parameters (e.g., spot size, fluence). SEM BSE images and U-Pb signal intensities of representative rutile grains. (A) Rutile grains with acceptable U-Pb analyses across a range of concordance. U-Pb date and concordance are from the ^{207}Pb correction method and Stacey-Kramers metric, respectively. Ablation pits are from U-Pb analysis (larger) and trace element analysis (smaller). The scale bar is 50 μm . All grains are from sample 18TK01; the grain number is in yellow. (B) Images of rutile grains with U-Pb analyses rejected because of inclusions (18TK01-002) or spiky signal (18TK01-008, -021, -105). (C-E) Representative U-Pb raw signal intensity patterns of accepted analyses (C) and rejected analyses from too low signal intensity (D) or inclusions and/or spiky signal (E).

570



575 **Figure 4.** Uncorrected detrital rutile U-Pb results displayed in Tera-Wasserburg space. Uncertainty ellipses are 2s propagated. The area displayed in (B) is highlighted by the blue box in (A).

5.2 U-Pb Geochronology and Common Pb Correction Results

580 The uncorrected U-Pb results are displayed in Figure 4. We note that all concordia diagram figures display the uncorrected U-Pb data; common Pb corrections force concordance and the corrected data are displayed as date distributions. A number of analyses plot close to the concordia curve and many plot along the discordia trend toward common Pb values. Both ^{208}Pb - and ^{207}Pb -corrections were performed on the uncorrected U-Pb analyses. After 200 iterations, the ^{208}Pb - and ^{207}Pb -corrections resulted in 547 and 487 corrected dates between 0 Ma and 4500 Ma, respectively. These numbers differ because no corrected date is calculated when the proportion of $^{206}\text{Pb}_{\text{common}}$ is greater than 1, and because the common Pb corrections can yield dates younger than 0 Ma or significantly older than 4500

Formatted: Font: +Headings (Times New Roman)
Formatted: Font: +Headings (Times New Roman), Pattern: Clear

Ma depending on the calculated proportion of $^{206}\text{Pb}_{\text{common}}$ (f_{206}). The Pb corrected U-Pb data are shown in Figure 5 as kernel density estimates (KDEs) and cumulative KDE distributions. The date distributions of individual samples are given in Figure S7, but due to small sample sizes, interpretations are based on the cumulative dataset.

The two different Pb corrections produce similar date distributions (Figure 5). For both distributions, the main date peak is at ca. 185 Ma with a minor peak around 297 Ma. The ^{207}Pb and ^{208}Pb distributions vary in the presence and amplitude of minor Paleozoic and older populations. The ^{208}Pb correction results include more Devonian and older grains ($n=131/547$, 24%) than the ^{207}Pb correction ($n=68/487$, 14%).

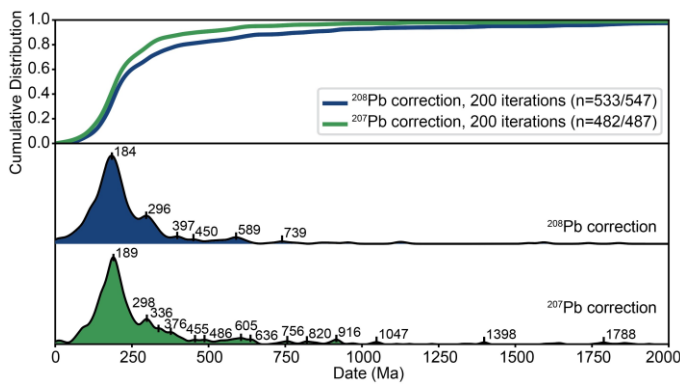


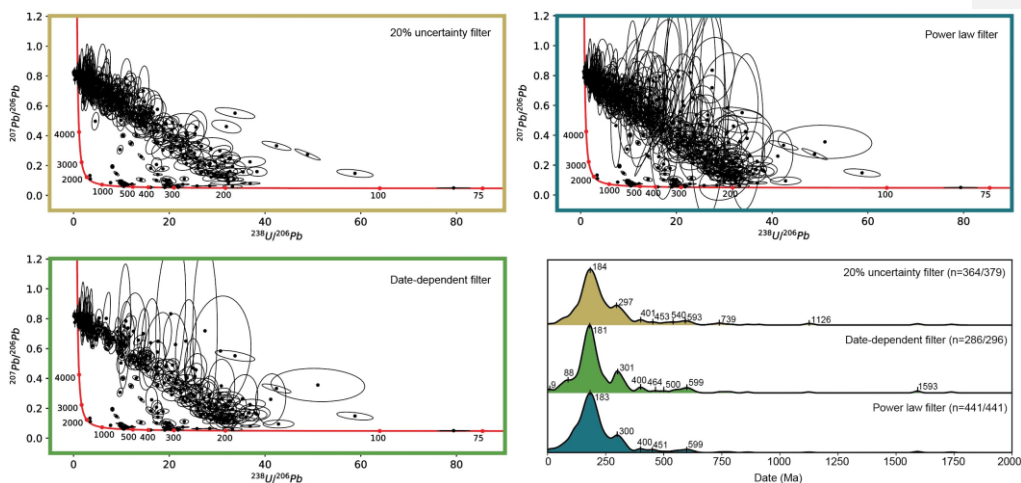
Figure 5. The ^{208}Pb and ^{207}Pb corrected date distributions from 0 to 2000 Ma displayed as normalized kernel density estimates and cumulative KDE distributions, visualized with detritalPy (Sharman et al., 2018). No discordance or uncertainty filter is applied.

5.3 Uncertainty and Discordance Thresholds

Detrital U-Pb data can further be filtered by U-Pb ratio uncertainty, date uncertainty, or discordance thresholds. Because the uncertainty on the corrected date is calculated from the uncertainty on the measured $^{206}\text{Pb}/^{238}\text{U}$ ratio (cf. Section 2), these metrics are similar. Figure 6 displays the results of three uncertainty threshold filters: (1) 20% uncertainty on $^{238}\text{U}/^{206}\text{Pb}$ and $^{207}\text{Pb}/^{206}\text{Pb}$ ratios (modified from Lippert, 2014), (2) a date-dependent filter that excludes analyses with > 10% date uncertainty for corrected dates > 100 Ma, > 20% uncertainty for dates 10–100 Ma, or > 25% uncertainty for dates < 10 Ma (after Govin et al., 2018), and (3) a power law threshold that excludes analyses if the percent uncertainty on the ^{207}Pb corrected date exceeds the function: $(t \wedge -0.65)^*8$ (after Chew et al., 2020). The results of these filters are displayed as uncorrected U-Pb data in Tera-Wasserburg space and ^{207}Pb corrected date distributions (Figure 6). From the ^{207}Pb corrected analyses total ($n=487$), the above thresholds exclude an additional 108 (22%), 191 (39%), and 46 (9%) analyses, respectively. The power law function excludes the fewest number of analyses.

The three filters have similar ^{207}Pb corrected date distributions (Figure 6). The main age modes identified in all three filters are 183 Ma, 300 Ma and 400 Ma. Minor Devonian and older date modes are present. Only the date-dependent filter identifies the 89 Ma date mode and it includes a 9 Ma mode that is significantly younger than the

youngest sampled strata (Bartonian–Priabonian). The U-Pb ratio and power law filters have nearly identical date peaks with the power law filter including more grains, especially in the ~183 Ma mode.



615 *Figure 6. Comparison of U-Pb data filters based on U-Pb ratio and date uncertainties, displayed in Tera-Wasserburg*
space (uncorrected) and normalized kernel density estimates (^{207}Pb -corrected). The U-Pb ratio uncertainty filter
(yellow) excludes all analyses with $^{238}\text{U}/^{206}\text{Pb}$ and $^{207}\text{Pb}/^{206}\text{Pb}$ ratio uncertainties above 20% (modified from Lippert,
2014). The date-dependent filter (green) excludes analyses based on the ^{207}Pb -corrected date and uncertainty (see
text; after Govin et al., 2018); after Govin et al., 2018). The power law filter (blue) excludes analyses if the percent
uncertainty on the ^{207}Pb corrected date exceeds the given power law function (see text; after Chew et al., 2020).
 620

To quantify discordance in common Pb bearing minerals, two metrics are considered: Aitchison and Stacey-Kramers distances (Figure 1). The results are shown in Figure 7 in Tera-Wasserburg space with uncorrected U-Pb analyses colored by distance (concordance). The Aitchison distance is calculated as the Euclidean distance between the analysis and concordia curve in log-ratio space, where higher distance values are considered more discordant. The results show that analyses closest to concordia are the least discordant (most concordant). This means that analyses close to the lower concordia curve and the common Pb composition are considered less discordant (more concordant) whereas analyses in the middle space are considered most discordant (Figure 7b). In the Stacey-Kramers distance formulation, discordance is calculated from the distance between the analysis and the upper and lower intercepts (Equation (14)). In this case, analyses closest to the common Pb composition are considered most discordant (Figure 7c). If a discordance filter were applied based on the Aitchison distance, analyses in the middle space of the concordia diagram would be excluded, whereas a discordance filter based on the Stacey-Kramers distance would exclude analyses closer to the common Pb composition. The Stacey-Kramers distance appears to reflect U-Pb systematics in common Pb bearing minerals and is a representative metric of discordance.

635

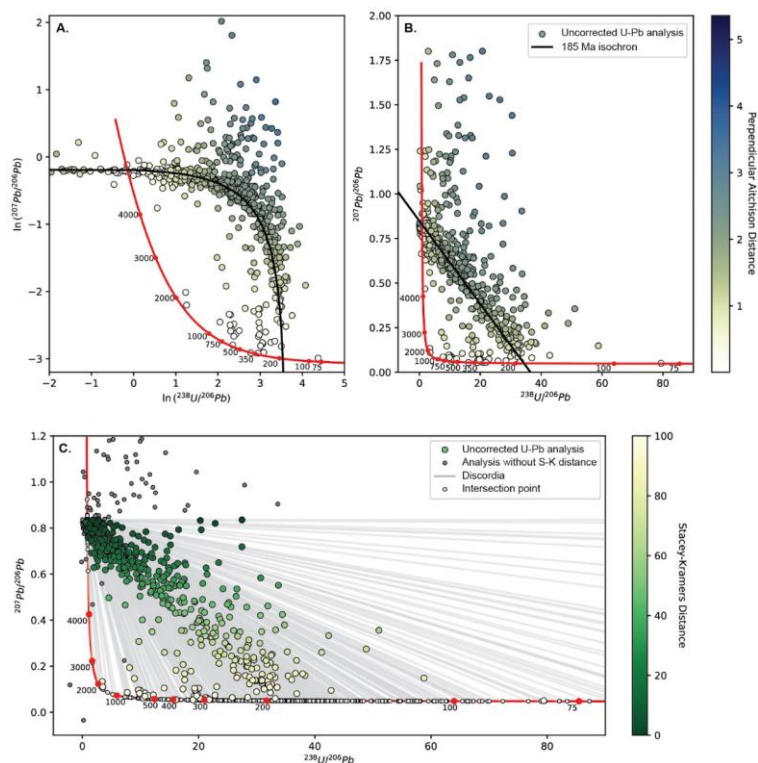


Figure 7. Comparison of (A,B) Aitchison distance and (C) Stacey-Kramers distance as metrics for discordance in common Pb bearing minerals. For simplicity all uncorrected U-Pb data are shown as circles rather than error ellipses. Circles are color-coded by distance (concordance). The Aitchison distance results are shown in Tera-Wasserburg concordia diagrams in original (B) and log-ratio space (A). The 185 Ma isochron is displayed in both diagrams. Circles closest to the concordia have the lowest discordance (highest concordance). (C) The Stacey-Kramers distance results are shown in Tera-Wasserburg space, where the gray lines are individual discordia and light gray circles are intersection points. Uncorrected U-Pb circles are color-coded for percent distance along the total discordia distance (from common Pb composition to lower intersection point). Circles closest to the lower concordia intercept have the lowest discordance. Dark gray circles are U-Pb analyses without Stacey-Kramers distance values (no lower intersection point due to positive discordia line slope, for example) or without ²⁰⁷Pb-corrected dates (due to $f_{206} > 1$).

The U-Pb dates are subdivided into bins based on their Stacey-Kramers concordance values. Figure 8 displays the ²⁰⁷Pb-corrected date distributions filtered using the power law threshold. The 100-80% concordance group has the most discrete date modes at 189 Ma, 307 Ma, 608 Ma, and 1593 Ma. The 80-60%, 60-40% and 40-0% bins have unimodal age distributions that are asymmetric toward older dates, and have a dominant age mode around 180 Ma. The cumulative distributions reveal that the distribution of all grains together has a similar distribution to that of the 40-0% group (Figure 8 top). Comparison of the whole distribution to the 100-80% concordance group reveals that, if a 20% discordance filter were applied similar to detrital zircon U-Pb workflows, the same general date modes would

be identified. However, the addition of lower concordance grains (i.e., 80-0% concordance groups) broadens the Jurassic peak and shifts it slightly younger from 189 Ma to ~180 Ma, decreases the amplitude of the Carboniferous and Proterozoic peaks, and increases the amplitude of the ~400-450 Ma peaks.

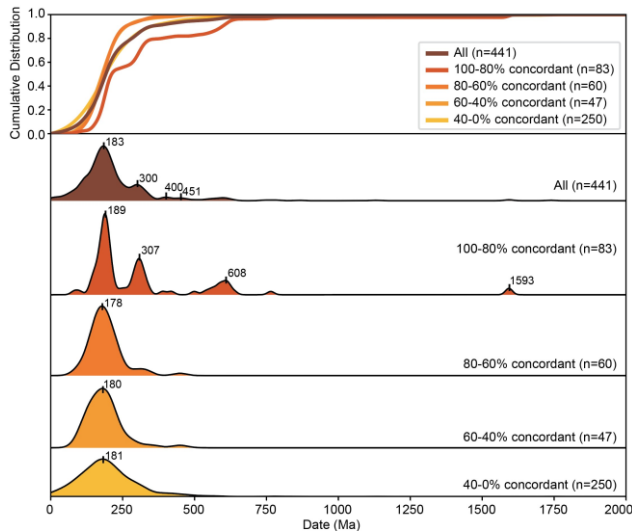


Figure 8 The concentration in an unknown is calculated based on the known concentration in the primary reference material and measured CPS of the primary reference material. Hence, if sensitivity is increased or decreased proportionally for reference materials and unknowns across various ICP-MS instruments and analytical parameters, the resulting concentration (ppm) will be the same. Yet, for instruments with lower sensitivity, the signal background and counting statistics will require a higher CPS to achieve the same measured concentration (i.e., 4 ppm). In this way, the U threshold filter is instrument dependent. The primary standard, R10, has a U concentration of 44 ppm and, in our measurements, on average, 2.1 million CPS ^{238}U . The ^{238}U baseline was about 5 CPS, therefore, the instrument set up used here has a maximum detection limit of about 0.0003 ppm ^{238}U (calculated from 3x background). The detrital rutile with the lowest uranium concentration (0.02 ppm) is nearly two orders of magnitude above this detection limit.

Relative kernel density estimates (KDEs; bottom panels) and cumulative KDE distributions (top) of ^{207}Pb -corrected, power law uncertainty filtered dates categorized by discordance from Stacey-Kramers distance values.

The U threshold filter is intended to maximize the proportion of concordant rutile analyzed. This includes rutile that have low incorporation of U during growth (independent of analytical instrumentation) and rutile that have poorly resolved U-Pb ratios due to low U-CPS such as old rutile and mafic rutile (machine dependent). This U-threshold filtering potentially introduces bias into the provenance results as omitting low U rutile biases results toward younger and metapelitic sources. Therefore, we explore whether using a 4 ppm threshold rather than analyzing rutile of all U concentrations is, in practice, best to maximize usable data or if it imparts a bias in provenance interpretations.

Formatted: Font: +Headings (Times New Roman)

680 A comparison of analyzed rutile included with the U threshold versus concordance filters is given in . The
U threshold filter includes all grains with U higher than 4 ppm, whereas the concordance filter includes grains more
than 40% concordant. Of the rutile that are more than 40% concordant, many have U concentrations below 4 ppm,
and all are above 0.1 ppm. The majority of grains older than 250 Ma are above 4 ppm U. Thus, the U threshold filter
does not seem to impart a bias toward older dates. The two filtering methods produce date spectra with the same
dominant modes, yet the amplitude of peaks vary between methods. For example, the 190 Ma mode is more prominent
685 with the concordance filter than with the U threshold filter. Furthermore, the predominant date modes contain rutile
of both metapelitic and metamafic origin (cf. next section and). Even though the two filters do not yield different
provenance interpretations in this case, most mafic classified grains have U contents below 4 ppm and are in the 190
Ma population. Hence, the U threshold filter is likely biasing results toward pelitic sources. In this dataset, all grains
more than 40% concordant are above 0.1 ppm, which could be a more suitable U threshold. However, a significant
690 number of highly discordant grains are also within 0.1 to 4 ppm U, meaning that the U threshold does not adequately
delineate interpretable data. As the U threshold filter is both instrumentation sensitivity dependent and biases
provenance results, we suggest that a U threshold protocol is not appropriate for provenance studies.

6 Trace Element Geochemistry Results

6.1 Source Lithology/Metamorphic Protolith

695 Trace element results are provided in the [supplementary information data repository](#). Discrimination diagrams
using V, Cr, Zr, Fe, and Nb can distinguish rutile from other TiO₂ polymorphs (Triebold et al., 2011), and all analyzed
grains plot within the [expected rutile fields \(Appendix A; field \(Figure A4S2\)\)](#). The Cr and Nb concentrations
discriminate between metapelitic and metamafic source rocks (Zack et al., 2004a; Triebold et al., 2011, 2012). Even
though ~~the exact~~ [there are multiple proposed](#) discrimination lines between metamafic and metapelitic source lithologies
700 (e.g., Meinhold et al., 2008; Triebold et al., 2012) ~~is debated~~, the detrital rutile in this dataset plot in both the metamafic
(33%) and metapelitic (67%) fields (Figure 9-a). There is no clustering of protolith by sample or U-Pb date, with
prominent date modes containing both metamafic and metapelitic grains (Figure 9-b). While some metamafic grains
plot close to concordia (more concordant), many plot close to the common Pb composition concordia intercept (more
discordant).

Formatted: Font: +Headings (Times New Roman)

Formatted: Font: +Headings (Times New Roman)

Formatted: Font: +Headings (Times New Roman)

Formatted: Font: +Headings (Times New Roman), Font color: Black

Formatted: Font: +Headings (Times New Roman), Font color: Black

Formatted: Normal, Indent: First line: 0.5", Border: Top: (No border), Bottom: (No border), Left: (No border), Right: (No border), Between : (No border)

Formatted: Font: +Headings (Times New Roman)

Formatted: Font: (Default) +Headings (Times New Roman), English (United States)

Formatted: Font: +Headings (Times New Roman), Font color: Black

Formatted: Font: +Headings (Times New Roman), Font color: Black

Formatted: Font: +Headings (Times New Roman), Font color: Black

Formatted: Font: +Headings (Times New Roman), Font color: Black

Formatted: Font: (Default) +Headings (Times New Roman), English (United States)

Formatted: Font: +Headings (Times New Roman)

Formatted: Font: (Default) +Headings (Times New Roman), English (United States)

Formatted: Font: (Default) +Headings (Times New Roman), English (United States)

Formatted: Font: (Default) +Headings (Times New Roman), English (United States)

Formatted: Font: +Headings (Times New Roman)

Formatted: Font: (Default) +Headings (Times New Roman), English (United States)

Formatted: Font: (Default) +Headings (Times New Roman), English (United States)

Formatted: Font: (Default) +Headings (Times New Roman), English (United States)

Formatted: Font: (Default) +Headings (Times New Roman), English (United States)

Formatted: Font: (Default) +Headings (Times New Roman), English (United States)

Formatted: Font: (Default) +Headings (Times New Roman), English (United States)

Formatted: Font: +Headings (Times New Roman)

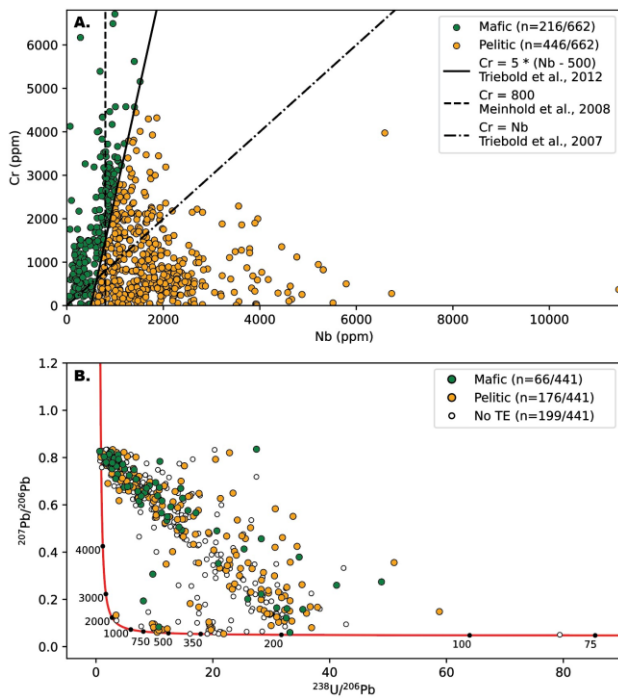


Figure 96.2 Source Metamorphism

(A) Protolith discrimination diagram. Grains are classified as (meta)mafic and (meta)pelitic based on the Triebold et al. (2012) line, with the Triebold et al. (2007) and Meinhold et al. (2008) lines also shown. (B) Concordia diagram of uncorrected U-Pb circles colored by protolith classification. The power law filter is applied. Open circles represent grains with U-Pb data but no trace element data (TE). Sample size differs between plots because not all grains have both U-Pb and trace element data.

6.2 Zr-in-Rutile Temperature and Uranium Concentration

The Zr-in-rutile temperatures were calculated using the Kohn (2020) calibration (Equation (1) temperature) at 13 kbar with an uncertainty of 5 kbar; results are displayed alongside U concentration (-). In this dataset, included in the data repository. The Zr concentrations range from 2 to 1934 ppm, yielding a range in source rock minimum peak temperatures from 359336 ± 15 °C to 824849 ± 28 °C. The Zr-in-rutile temperature results are displayed alongside U concentration and colored by protolith (Figure 10). Even though many studies only acquire U-Pb dates on rutile with U > 4-5 ppm, 87% of (-). There is not a correlation between Zr-in-rutile in this study temperature and protolith. The majority of grains have moderate temperatures corresponding to greenschist to blueschist facies conditions: 68% (n=147/216) of mafic and 67% (n=301/446) of pelitic grains are below 4 ppm (n=517/592). This commonly accepted strategy has important implications for provenance interpretation. In our dataset, the majority of 500 °C. When

Formatted: Font: +Headings (Times New Roman)

Formatted: Font: (Default) +Headings (Times New Roman), Do not check spelling or grammar

Formatted: Font: +Headings (Times New Roman)

Formatted: Font: +Headings (Times New Roman)

Formatted: Font: +Headings (Times New Roman)

Formatted: Font: +Headings (Times New Roman)

Formatted: Font: +Headings (Times New Roman)

Formatted: Font: +Headings (Times New Roman), Font color: Black, English (United Kingdom)

Formatted: Font: +Headings (Times New Roman), Font color: Black, English (United Kingdom)

displayed in Tera-Wasserburg space, dominant date modes—90 Ma, 185 Ma, 300 Ma, 500–650 Ma—have fairly consistent Zr-in-rutile temperatures (Figure 11). The highest temperatures, reaching granulite facies conditions, are found in the 90 Ma date mode. The 500–650 Ma and 300 Ma rutile grains similarly preserve high temperatures, up to 700–820 °C, whereas the majority of 185 Ma grains have temperatures in greenschist to blueschist facies around 450–550 °C.

The uranium concentrations range from 0.0006 to 113 ppm. These low values are within the detection limit. The primary standard, R10, has a U concentration of 44 ppm (Luvizotto et al., 2009) and, in our measurements, on average, 2.1 million CPS ²³⁸U (i.e., ~50,000 counts/ppm). The ²³⁸U baseline was about 5 CPS, therefore, the instrument set-up has a detection limit of about 0.0003 ppm ²³⁸U (calculated from 3x background). All analyses are above the detection limit, with 91% (n=555/612) of analyses at least an order of magnitude above this limit. The comparison of Zr-in-rutile temperatures with U concentration reveals that the majority of low U rutile (< 4 ppm) are within greenschist to blueschist facies conditions (68%, n=205/303 below 500 °C; Figure 10 with U →). Additionally, mafic classified grains are dominantly low U (95%, n=106/112 below 4 ppm). The majority of rutile with U contents above 4 ppm are classified as pelitic (85%, n=34/40) and generally have higher Zr contents.

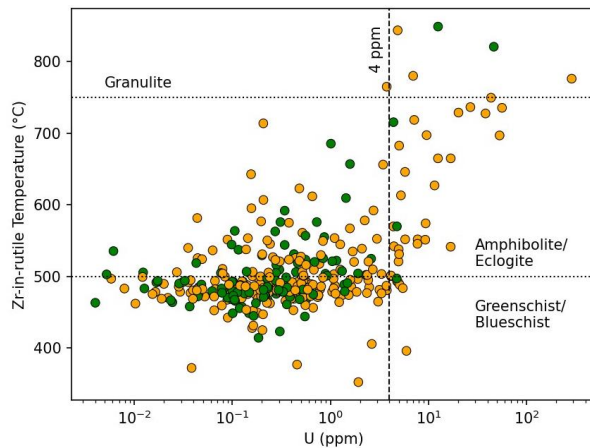


Figure 10. Zr-in-rutile temperature versus U concentration. Mafic and pelitic discrimination is from Cr and Nb concentrations (Figure 9) mafic protoliths shown in green, pelitic in orange. The 4 ppm U line demarcates grains included/excluded by a U filter. Zr-in-rutile temperatures follow the Kohn (2020) calibration. Note that not all analyses have both U and trace element (TE) data, therefore there are fewer grains represented in this scatter plot than in Figure 9.

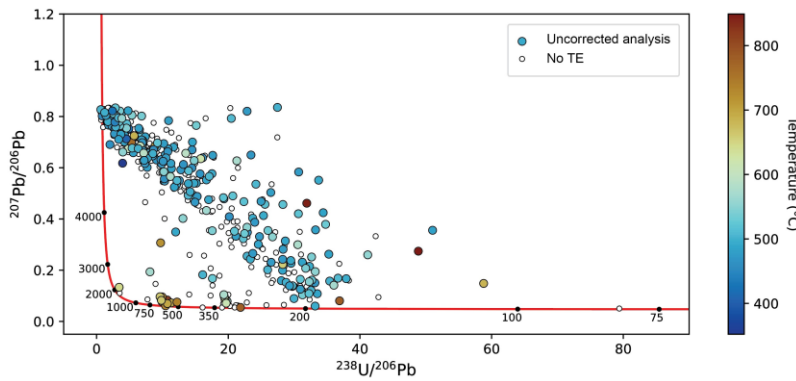
Formatted: Font: +Headings (Times New Roman), Font color: Black, English (United Kingdom)

Formatted: Font: +Headings (Times New Roman)

Formatted: Font: +Headings (Times New Roman)

Formatted: Default Paragraph Font, Font: (Default) +Headings (Times New Roman)

Formatted: Default Paragraph Font, Font: (Default) +Headings (Times New Roman), Font color: Black



745 *Figure 11. Uncorrected rutile U-Pb results in Tera-Wasserburg space colored by Zr-in-rutile temperature calculated from the Kohn (2020) calibration. The mode centered around 95 Ma has the highest temperatures, and modes centered around 300 Ma and 500–650 Ma also contain high temperatures, whereas the 185 Ma mode is predominantly composed of moderate temperature grains. Open circles are rutile U-Pb analyses without trace element (TE) data. Colormap is from Crameri (2020).*

750 **6.3 Principal Component Analysis**

Principal component analysis (PCA) was conducted on the detrital rutile trace element compositions (V, Cr, Zn, Zr, Nb, Hf, Ta, W) using an in-house R code (cf. Section 4.4; Mueller, 2024) and the results are given in the data repository. PCA is a multivariate statistical procedure that identifies the variables that explain the most amount of variance within a dataset. The principal components are ranked based on the amount of variance they explain. Plots of principal component 'loadings' display the distribution of the trace element variables with respect to the principal components. The scores and loadings in Figure 12 show that the variance between rutile grains can largely be explained by Cr, Nb and Ta, and W, Zr, and Hf. Because Cr, Nb and Ta are protolith dependent (PC 2) and Hf and Zr are temperature dependent (PC 1), the variance in detrital rutile trace element chemistry is best explained by both protolith and metamorphic grade, tracking these two properties of source rocks. The protolith and temperature components capture the most important portion of the trace element results.

Formatted: Default Paragraph Font, Font: (Default) +Headings (Times New Roman)

Formatted: Font: +Headings (Times New Roman)

Formatted: Body Char, Font: (Default) +Headings (Times New Roman)

Formatted: Font: +Headings (Times New Roman), Font color: Black

Formatted: Font: +Headings (Times New Roman), Font color: Black

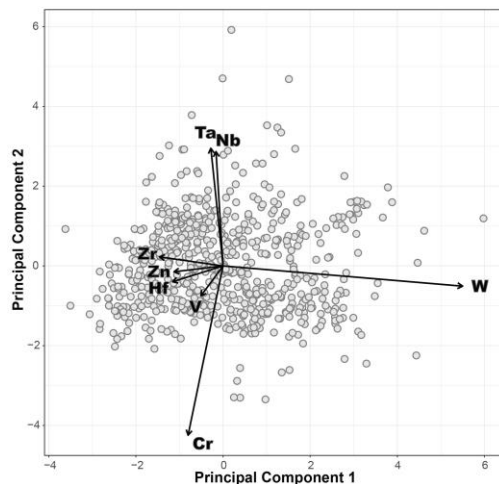


Figure 12. PCA score and loadings plot of principal components 1 and 2, which cumulatively explain 66.6% of trace element variance. The variance in trace element chemistry is best explained by metamorphic grade (PC 1) and protolith (PC 2).

Formatted: Font: +Headings (Times New Roman)

Formatted: Default Paragraph Font, Font: (Default) +Headings (Times New Roman)

Formatted: Default Paragraph Font, Font: (Default) +Headings (Times New Roman), Font color: Black

765 **7 Discussion**

7.1 Recommendations for U-Pb Data Rejection, Correction, and Filtering

The complex, natural dataset presented here allows an examination of the current practices of data reporting and limitations of large-*n* detrital rutile studies. In this study, a large number of analyses were rejected during U-Pb data reduction, but the SEM images do not provide simple criteria (e.g., inclusions, fractures) how to better select grains that will produce acceptable signal quality or lower U-Pb discordance (

770

Figure 3). All areas selected for analysis appeared inclusion-free before ablation, yet some analyses evidently ablated into inclusions (

Figure 3b,e). Because we expected grains from mafic sources with low U or low Pb concentrations, we used a large 50 μm laser beam diameter, but this potentially increased the probability of hitting inclusions. While rejecting analyses is not ideal, low U and Pb signal intensities are not unexpected in natural samples, so some degree of data rejection is to be anticipated, especially given the predicted metamafic (very low U) protolith sources. We contend here that while the exclusion of data from interpretation is common to many detrital rutile studies (e.g., Bracciali et al., 2013; Rösel et al., 2014, 2019; Caracciolo et al., 2021), ours included. However, in most studies, the number of discarded analyses and criteria for discarding analyses during U-Pb data reduction is unclear or not mentioned, thereby limiting opportunities to evaluate data quality and navigate results in a potentially meaningful way. We recommend that these criteria be explicitly stated and discussed in all studies using detrital rutile U-Pb geochronology.

775

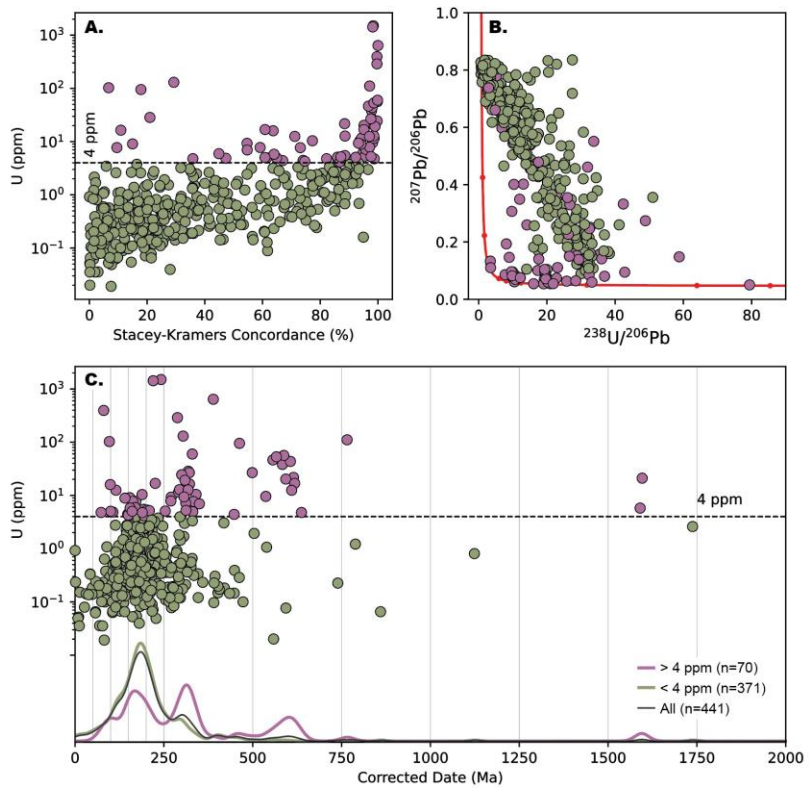
780

After U-Pb data reduction, additional analyses were excluded during common Pb correction and uncertainty filtering. Here, the ²⁰⁸Pb and ²⁰⁷Pb corrections produce similar date spectra (Figure 5) as do the various uncertainty

785 [filters \(Figure 6\)](#). We tentatively favor the power law uncertainty filter as it does not appear to alter the presence or
proportion of individual age populations, and because this filter excludes the fewest analyses. Future work is needed
to determine if this holds in other datasets. We propose that the Stacey-Kramers distance is a better metric than
Aitchison distance for quantifying discordance as it reflects U-Pb systematics (Figure 7). A discordance threshold is
not recommended as an exclusion criterion based on the similarity of the date distributions across concordance bins
790 [\(Figure 8\)](#). Further, most mafic-classified grains plot closer to common Pb compositions, so a discordance filter would
bias results toward pelitic and high U grains (Figure 9). Including initially discordant data is acceptable because
geologically meaningful interpretations can be made from initially discordant data when appropriate common Pb
corrections are applied. Note that common ²⁰⁸Pb and ²⁰⁷Pb corrections force concordance so that initially discordant
data are concordant after correction. U-Pb discordance in common Pb bearing minerals is well documented in
published reference materials (e.g., Chew et al., 2011, 2014). In petrochronologic applications, *in-situ* work
795 demonstrates that individual analyses can be nearly 100% discordant and still interpreted confidently within the
population of co-genetic grains (e.g., Poulaki et al., 2023). Although some detrital rutile U-Pb datasets are dominated
by concordant analyses (e.g., Rösel et al., 2019, Kooijman et al. 2010), many detrital datasets contain analyses across
the concordance spectrum, including highly discordant analyses, whose Pb-corrected dates are used in interpretations
(Bracciali et al., 2013; Mark et al., 2016; O’Sullivan et al., 2016; Govin et al., 2018; Ershova et al., 2024). For these
800 reasons, we do not advocate filtering detrital rutile U-Pb data based on discordance. Future work with large-*n* detrital
datasets is needed to explore the influence of common Pb corrections and data filters based on uncertainty and
discordance, including whether these filters influence date distributions in other datasets.

Expanding detrital rutile U-Pb applications is hindered by data rejection, as seen in this dataset and others.
[Caracciolo et al. \(2021\)](#) attempted to present a large-*n* detrital rutile dataset in which rutile grains were identified via
805 Raman spectroscopy. Their workflow using automated Raman is better suited for identifying polymorphs and reducing
bias than the handpicking and SEM-EDS workflow used here and in many other studies. However, of the 712 detrital
rutile grains analyzed by Caracciolo et al. (2021), only 347 grains remained (48%) after their data reduction and
uncertainty filtering (using a modified power law filter). Similar to our dataset, there were not enough rutile dates per
sample to discuss sample-by-sample provenance interpretations (Figure S7). Govin et al. (2018) discarded 36%
810 (n=53/146) of detrital rutile U-Pb analyses using their date-dependent filter. Shaanan et al. (2020) present the only
other detrital rutile dataset from Anatolia that does not impose a low-U filter; they discard 60% (n=97/163) of their
data during discordance filtering. Together these studies illustrate that there is a formidable methodological hurdle in
trying to scale up detrital rutile U-Pb to large-*n* provenance applications.

Formatted: Font: +Headings (Times New Roman), Font color: Black



815 *Figure 13. Comparison of detrital rutile filtering based on U concentration or concordance. (A) Rutile U*
concentration versus percent concordance (Stacey-Kramers distance). The U-threshold filter groups grains greater
than and less than 4 ppm U. (B) Rutile U-Pb results in Tera-Wasserburg space following the color scheme in panel
A. (C) Rutile U concentration versus ²⁰⁷Pb-corrected U-Pb date. The relative KDEs display the date spectra from the
different U concentration groups: all analyses, above 4 ppm U, below 4 ppm U. The power law filter is applied to all
plots in the figure.

Formatted: Font: +Headings (Times New Roman), Font color: Black

7.2 Low Uranium Rutile

Isotopic and elemental concentrations are calculated based on the measured count rate (i.e., counts per second, CPS), which is inherently dependent on the individual mass spectrometer and laser ablation parameters (e.g., spot size, fluence). For instruments with lower sensitivity (lower CPS per ppm), the same calculated concentration (i.e., the 4 ppm threshold used in some publications) yields lower CPS and therefore higher analytical uncertainties than for instrument with higher sensitivity. In this way, the U threshold filter based on calculated concentration is instrument and parameter dependent and we do not recommend screening rutile to exclude low U concentration analyses.

Most studies no longer impose a U threshold, yet, it is a regional concern in Türkiye where two of the four detrital rutile U-Pb datasets only analyze U-Pb on detrital rutile with uranium concentrations above 4-5 ppm (Okay et

Formatted: Normal, Indent: First line: 0.5"

al., 2011; Şengün et al., 2020). The two studies that do not use a U filter analyze all detrital rutile grains (Shaanan et al., 2020; this study) whereas, in this dataset of this study, 87% of detrital rutile are below 4 ppm U (n=537/612). The majority of detrital rutile with U > 4 ppm are classified as pelitic and generally have higher Zr contents (higher temperature), whereas low-U rutile in this study generally correlates with lower Zr contents (lower temperature) and includes the majority of mafic-classified grains (Figure 9). Note that there are limitations to the Zr-in-rutile thermometer in mafic rocks if the equilibrium conditions are not met. Figure 13 compares U concentration with concordance and U-Pb date. Concordance does not appear to be correlated with U concentration (Figure 13a). Comparing the date distribution for all grains with that of the below and above 4 ppm U groups reveals that provenance results would be biased by excluding grains below 4 ppm U (Figure 13c). The above 4 ppm U group has age modes at 100 Ma, 165 Ma, 315 Ma, 458 Ma, and 600 Ma (Figure 13c pink) whereas the total date spectrum has peaks at 185 Ma, 300 Ma, 400 Ma, 450 Ma and 600 Ma (Figure 13). Therefore, the exclusion of low-U rutile in provenance studies likely misses sediment sourced from lower grade metamorphic units and metamafic sources (gray). The above 4 ppm U rutile group has higher amplitude Paleozoic peaks, a minor 100 Ma peak, and a younger, lower amplitude Mesozoic peak (165 Ma vs 185 Ma). In summary, the U threshold filter introduces bias into the provenance results because omitting low-U rutile biases results toward metapelitic sources, higher Zr-in-rutile temperatures, and shifts the prominent date modes and their amplitudes.

Formatted: Font: +Headings (Times New Roman)

7.3 Source Protolith and Metamorphism

The Zr-in-rutile thermometer generally preserves the crystallization or recrystallization temperature. The Zr-in-rutile thermometer can become uncoupled from the U-Pb age because Pb diffusion during medium- to high-temperature metamorphic events or extended cooling periods will lead to cause partial or complete resetting of the U-Pb system (Cherniak et al., 2007; Luvizotto and Zack, 2009; Kooijman et al., 2012; Pereira and Storey, 2023). When displayed in Tera-Wasserburg space, the 4 dominant modes—95 Ma, 190 Ma, 310 Ma, 580 Ma—have fairly consistent Zr in rutile temperatures (°). The highest temperatures are found in the 95 Ma date mode, reaching granulite facies conditions. The 580 Ma and 310 Ma rutiles similarly preserve high temperatures, up to 700–800 °C, whereas the majority of 190 Ma rutiles show temperatures around 450–500 °C corresponding to blueschist/greenschist facies conditions. Because temperatures calculated for the 190 Ma population are cooler than for the older events and are not high enough to have reset the U-Pb dates, we interpret these temperatures as primary. Furthermore, partially reset dates would smear the data along discordia from the initial crystallization event age, not towards common Pb.

Formatted: Font: +Headings (Times New Roman)

Formatted: Font: +Headings (Times New Roman), Font color: Dark Red

Formatted: Font: +Headings (Times New Roman), Font color: Black

Formatted: Normal, Indent: First line: 0.5", Border: Top: (No border), Bottom: (No border), Left: (No border), Right: (No border), Between : (No border)

Formatted: Font: +Headings (Times New Roman), Font color: Black

Formatted: Font: +Headings (Times New Roman), Font color: Black

6.3 Principal Component Analysis

Principal component analysis (PCA) was conducted on the detrital rutile trace element compositions (V, Cr, Zn, Ga, Zr, Nb, Mo, Sn, Sb, Hf, Ta, W) using OriginPro statistical software and the results are given in Appendix B. PCA is a multivariate statistical procedure that identifies the variables that explain the most amount of variance within a dataset. The principal components are ranked based on the amount of variance they explain. Plots of principal component 'loadings' display the distribution of the trace element variables with respect to the principal components.

Formatted: Font: +Headings (Times New Roman), Font color: Black

Formatted: Font: +Headings (Times New Roman), Font color: Black

Formatted: Font: +Headings (Times New Roman), Font color: Black

Formatted: Font: +Headings (Times New Roman)

Formatted: Font: +Headings (Times New Roman), Font color: Black

Formatted: Font: +Headings (Times New Roman), Font color: Black

shows. The Zr-in-rutile temperatures and protolith classification are discussed in the following section in the context of regional provenance. The PCA results show that the variance between samples can largely be first two principal components are explained by Hf, Zr, Sn, Cr, V, Nb and Ta. Because Cr, Nb and Ta are protolith dependent (PC 2), and Hf, Zr, and Zr are Hf. These elements are protolith (Cr, Nb, Ta) and temperature dependent (PC 1), the variance in (Zr, Hf) dependent, therefore the protolith and Zr-in-rutile sections are already exploring the most salient aspects of the trace element dataset.

7.4 Evaluating Bias in Discarded U-Pb Data

To evaluate the potential bias in U-Pb data reduction and processing, the detrital rutile grains with both U-Pb and trace element data are compared to those with only trace element data (U-Pb rejected and/or excluded by filter). Figure 14 gives a sense for what data are missing from the U-Pb results as well as the effects of the uncertainty filter. Not all detrital rutile grains have trace element data, so the subset of grains with U-Pb analyses and without trace element data cannot be considered. In the plots of protolith versus Zr-in-rutile temperature, grains included by the power law filter (Figure 14a) are compared to those excluded by the power law filter or without U-Pb data (Figure 14b). Effectively this compares accepted U-Pb analyses to those rejected from unacceptable U-Pb signal patterns or high uncertainties. About 30% of mafic-classified grains and 35% of pelitic-classified grains are acceptable U-Pb analyses included by the power law filter (Figure 14c). The analyses rejected by power law filtering (Figure 14c) have a similar temperature distribution, with the majority of temperatures from 450–550 °C. Most grains with these temperatures fall within the 185 Ma date mode (Figure 11), potentially suggesting that the detrital rutile grains with poor U-Pb precision would have ~185 Ma dates. Further, the rejected analyses group has fewer high temperature pelitic grains (> 600 °C) and a more abundant lower temperature pelitic population (< 400 °C). These temperature windows do not seem diagnostic of specific date populations among pelitic grains, however, about 30% of high temperature pelitic grains fall within the 500-650 Ma population (Figure 11 trace element chemistry is best explained by both protolith and metamorphic grade, allowing us to track these two properties of source rocks.). The similarity in temperature distributions of pelitic and mafic grains between the accepted and rejected U-Pb analyses suggests that there is not significant bias in the U-Pb results due to data rejection. Consequently, the U-Pb and trace element data can be used together to interrogate potential bias in U-Pb data rejection and filtering.

Formatted: Font: +Headings (Times New Roman), Font color: Black

Formatted: Font: +Headings (Times New Roman), Font color: Black

Formatted: Font: +Headings (Times New Roman), Font color: Black

Formatted: Font: +Headings (Times New Roman), Font color: Black

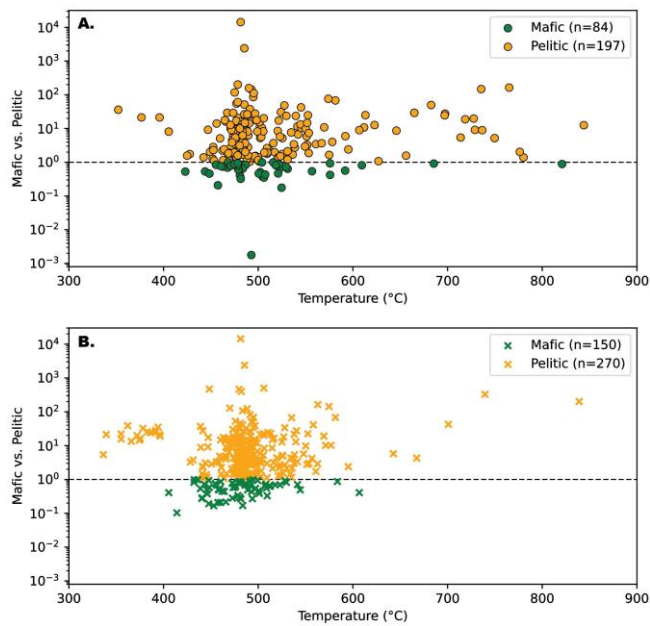
Formatted: Font: +Headings (Times New Roman), Font color: Black

Formatted: Font: +Headings (Times New Roman), Font color: Black

Formatted: Font: +Headings (Times New Roman)

Formatted: Normal, Indent: First line: 0.5"

Formatted: Font: +Headings (Times New Roman)



895 **Figure 14.** (A) Protolith versus Zr-in-rutile temperature plot displays all detrital rutile analyses with trace element data included in the power law filter. (B) Plot B shows both the detrital rutile analyses without U-Pb data and those excluded by the power law filter in A. The y-axis values are the transformed distance from the mafic-pelitic discrimination line of [Triebold et al. \(2012\)](#) ([Figure 97 Utility of Detrital Rutile Petrochronology 7-1](#)).

8 Anatolian Sedimentary Provenance Interpretation

900 Sedimentary provenance is interpreted from all detrital rutile dates together, rather than by sample, due to the small number of analyses in each [sample](#) (see [Figure S3S7](#) for individual sample results). The detrital rutile results are displayed along with detrital zircon dates from the same Upper Cretaceous to Eocene units in the Central Sakarya and Sarıcakaya Basins ([Figure 15](#); data from [Campbell, 2017](#); [Ocakoglu et al., 2018](#); [Mueller et al., 2019, 2022](#); [Okay and Kylander-Clark, 2022](#)). [The detrital zircon and rutile provenance results are discussed together from youngest to oldest date population.](#) The rutile grains that (poorly) define the ca. 9590 Ma population ([Figure 15](#)) include some of the highest Zr-in-rutile temperatures ([Figure 11](#)). The zircon record has abundant Late Cretaceous and Eocene populations ([Figure 15](#)) and are concurrent associated with a 110–76 Ma high flux magmatic flare-ups during Alpine orogeny-related subduction and syn-collisional magmatism, respectively ([Harris et al., 1994](#); [Kasapoğlu et al., 2016](#); [Yildiz et al., 2015](#); [Ocakoglu et al., 2018](#); [Mueller et al., 2022](#); [Campbell et al., 2023](#)) event that is dominant in the detrital zircon record. The lower plate Anatolide-Tauride northern margin terrane underwent HP/LT blueschist facies metamorphism

- Formatted: Font: +Headings (Times New Roman)
- Formatted: Font: +Headings (Times New Roman)
- Formatted: Heading 1
- Formatted: Font: +Headings (Times New Roman), Font color: Black
- Formatted: Font: +Headings (Times New Roman), Font color: Black
- Formatted: Font: +Headings (Times New Roman), Font color: Black
- Formatted: Font: +Headings (Times New Roman), English (United States)
- Formatted: Font: +Headings (Times New Roman)
- Formatted: Font: +Headings (Times New Roman)
- Formatted: Font: +Headings (Times New Roman), English (United States)
- Formatted: Font: +Headings (Times New Roman), English (United States)
- Formatted: Font: +Headings (Times New Roman), English (United States)
- Formatted: Font: +Headings (Times New Roman), English (United States)
- Formatted: Font: +Headings (Times New Roman), English (United States)
- Formatted: Font: +Headings (Times New Roman), English (United States)
- Formatted: Font: +Headings (Times New Roman), English (United States)
- Formatted: Font: +Headings (Times New Roman), English (United States)

910 ~~in the that generally youngs from Late Cretaceous, however, in the north to early Eocene in the south~~ (Sherlock et al.,
1999; Okay and Kelley, 1994; Candan et al., 2005; Pourteau et al., 2016). ~~The samples are from sedimentary basins~~
915 ~~in the upper plate (Figure 15 sedimentary provenance) and the detrital zircon record indicates no sediment transport~~
~~across the suture zone between from the Anatolide-Tauride terranes to the Pontides and Anatolide-Tauride terranes in~~
~~the latest Cretaceous (Okay and Kylander-Clark, 2022). Thus, we interpret the 9590 Ma age rutile population is~~
~~interpreted as either igneous or metamorphic rutile derived from Late Cretaceous magmatism and associated contact~~
~~metamorphism on the Pontides.~~

~~The 490185 Ma peak includes the lowest Zr-in-rutile temperatures (~450–5750 °C; Figure 11), mafic and~~
~~pelitic sources (Figure 9), and predominantly low -U rutile (Figure 13). The age, lithology, and temperature findings~~
920 ~~support a Karakaya Complex sediment source. The Permian-Triassic Karakaya Complex contains intra-oceanic~~
~~basalts and forearc deposits, the that were metamorphosed units reached temperatures of to blueschist and epidote-~~
~~amphibolite facies (340–550 ± 50 °C around 200–215 Ma; Okay et al., 2002; Federici et al., 2010) during the Triassic~~
~~Cimmerian event. The rutile U-Pb dates interpreted as Karakaya Complex (broad 185 Ma peak) are younger than~~
925 ~~existing Karakaya Complex phengite, glaucophane, and barroisite Ar-Ar cooling dates (~200–215 Ma; Okay et al.,~~
~~2002; Federici et al., 2010; Şengör et al., 1984). The closure temperature windows for rutile U-Pb and phengite Ar-~~
~~Ar overlap, with Pb in rutile extending to lower temperature than Ar in phengitic white mica (Itaya, 2020; M. Grove,~~
~~pers. comm., 2024)). The younger rutile dates likely indicate protracted cooling because extended time spent in the~~
~~partial retention zone would cause variable Pb loss that could lead to a younger rutile U-Pb dates than any actual~~
~~heating event and/or a spread in ages (broad peak). This 185 Ma population is not prominent in the detrital zircon~~
930 ~~spectra. Detrital zircons from Karakaya Complex units have age modes at ca. 235 Ma, 315 Ma, and 400 Ma and are~~
~~interpreted as sediment input to the forearc from the Pontides Triassic magmatic arc, oceanic plateau, or spreading~~
~~center (e.g., Okay et al., 2015). Variscan granitoids, and crystalline basement to the forearc (Ustaömer et al., 2016).~~
~~This 190 Ma rutile age population is not prominent~~

~~The Carboniferous peaks in the detrital zircon spectra and records Karakaya Complex metamorphism. The~~
~~310 Ma and 580 Ma detrital rutile age populations are mirrored in the detrital zircon and rutile record and match the~~
935 ~~zircon age modes present in Pontides basement. The Carboniferous peak corresponds correspond to a ~330–340 Ma~~
~~pulse of high-T metamorphism and ~290–320 Ma magmatism in the Pontides during the Variscan orogeny (Topuz et~~
~~al., 2007, 2020; Ustaömer et al., 2012, 2013). These basement units crop out along the thrust fault that partitions the~~
~~two basins (Tuzaklı-Gümele Thrust; b). Variscan-aged detrital rutiles were found in Jurassic sandstones in the Central~~
940 ~~Sakaraya Basin and interpreted as derived from either primary Pontide basement or recycled sedimentary~~
~~sources (Şengün et al., 2020). The Pontide basement units crop out along the thrust fault that partitions the two sedimentary~~
~~basins (Tuzaklı-Gümele Thrust; Figure 15b). Therefore, the Variscan-aged detrital rutile of this age present in Upper~~
~~Cretaceous to Eocene units could be derived from primary basement sources or recycled Jurassic sedimentary units.~~
~~Notably the ca. 395 Ma peak in the detrital zircon record is absent from the rutile age spectra, possibly because the~~
945 ~~rutile of that age were overprinted by the Carboniferous high temperature event. Scaree Silurian (440–420 Ma) and~~
~~The Pontides crystalline basement contains scarce Devonian (380–400–380 Ma) and Silurian (420–440 Ma)~~
~~metaigneous rocks exist, which are exposed in the hanging wall of the Tuzaklı-Gümele Thrust (Topuz et al., 2020).~~

Formatted

Formatted

Formatted

Formatted: Font: +Headings (Times New Roman)

Formatted

Formatted

Formatted

Formatted

The absence of this age population in the rutile record could be due to the scarcity of outcrops ~~of small~~ sample size, ~~dilution during sediment recycling, or overprinting by the Carboniferous high temperature event. Late Ordovician–Early Silurian metamorphism associated with the accretion of the Istanbul–Moesia–Scythian Platform~~ (Okay et al., 2006) ~~is not prominent in the detrital rutile record, which could suggest the absence of major south-directed sediment transport across the Pontides (i.e., from the Istanbul Zone to Sakarya Zone across Intra-Pontide ocean/suture) during the Late Cretaceous to Eocene.~~ Lastly, the ~~580~~500–650 Ma Pan-African ~~and older~~ detrital rutile ages align with the detrital zircon age spectra. ~~Gondwana-derived terranes are characterized by Neoproterozoic–Cambrian plutonism and metamorphism from the Pan-African–Cadomian orogeny, which is not well documented in Anatolia~~ (Okay et al., 2006) ~~These grains. Grains of this age~~ could be sourced from the Pontides basement or recycled from sedimentary units (Ustaömer et al., 2012; Mueller et al., 2019); ~~however, because.~~ However, if the grains of this age were first-cycle from crystalline basement sources, we would expect them to have reset U-Pb dates from younger metamorphic reheating events. In this interpretation, the 500–650 Ma dates are preserved because these grains must have ~~escaped been unaffected by any younger high-T events.~~ In order to have escaped metamorphic reheating, the grains had to have been already eroded from the crystalline basement and deposited in sedimentary units. Therefore, we interpret them the 500–650 Ma grains as polycyclic grains derived from recycled sedimentary units. ~~Carboniferous and older zircon grains have been interpreted as a mix of primary crystalline Pontides basement and recycled sedimentary sources, including recycled from the Karakaya Complex metasedimentary units and from sedimentary units exposed along thrust sheets. Therefore, it is possible that the rutile grains are derived from primary sources or recycled from Triassic and younger sedimentary units.~~ Together, the detrital zircon and rutile age spectra demonstrate that, from the Late Cretaceous to Eocene, sediment was ~~sourced~~ to the Central Sakarya and Sarıcakaya Basins from syn-depositional magmatic centers, the Karakaya Complex within the suture zone, the Pontides crystalline basement, and recycled sedimentary units (Figure 15).

Formatted: Font: +Headings (Times New Roman)

Formatted: Font: +Headings (Times New Roman)

Formatted: Font: +Headings (Times New Roman)

Formatted: Font: +Headings (Times New Roman)

Formatted: Font: +Headings (Times New Roman), Font color: Black, English (United Kingdom)

Formatted: Font: +Headings (Times New Roman)

Formatted: Font: +Headings (Times New Roman)

Formatted: Font: +Headings (Times New Roman), Font color: Black

Formatted: Font: +Headings (Times New Roman), Font color: Black

Formatted: Font: +Headings (Times New Roman), Font color: Black

Formatted: Font: +Headings (Times New Roman), Font color: Black

Formatted: Font: +Headings (Times New Roman), Font color: Black, English (United Kingdom)

Formatted: Font: +Headings (Times New Roman), English (United Kingdom)

Formatted: Font: +Headings (Times New Roman), English (United Kingdom)

Formatted: Font: +Headings (Times New Roman), Font color: Black, English (United Kingdom)

Formatted: Font: +Headings (Times New Roman), Font color: Black

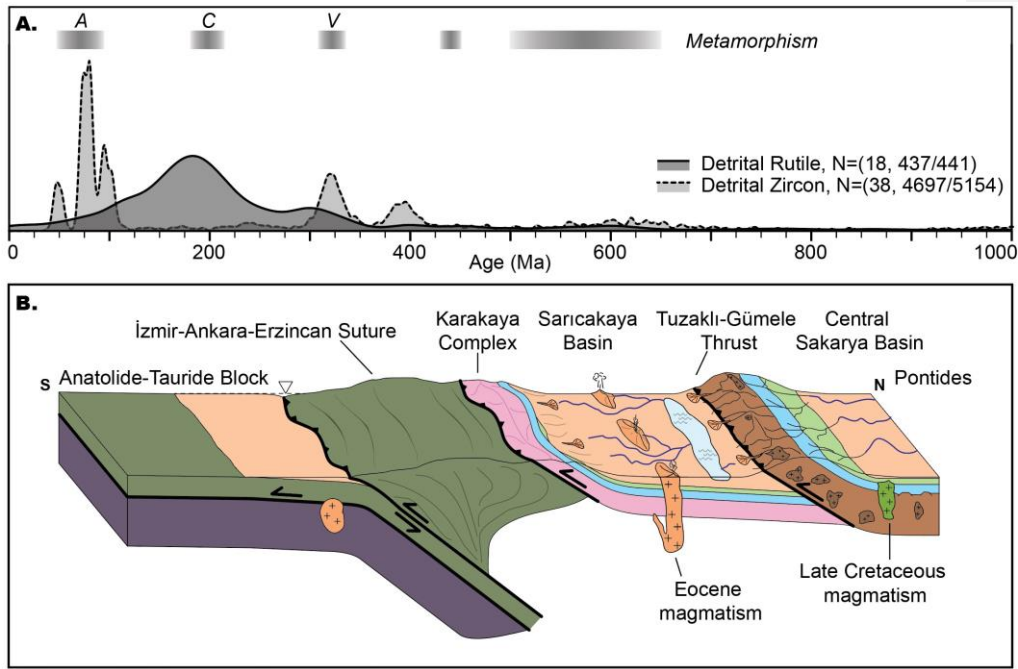


Figure 157.2 Implications of New Workflow on Provenance Applications

Employing detrital rutile geochronology and geochemistry, and the workflows presented here, have several implications for the provenance interpretations. First, the various Pb correction methods produce similar age spectra and do not change the final provenance interpretations. Second, the 190-Ma population is poorly represented in the detrital zircon record (-). This means that detrital rutile is capturing a unique sedimentary provenance signal. The Karakaya Complex is not easily captured in the detrital zircon record due to both zircon-poor lithologies and the multi-cyclic Carboniferous and Devonian-aged grains. This finding emphasizes the utility of detrital rutile to discriminate between specific sediment sources. Third, the majority of rutile analyses in the 190-Ma group are low-U grains, meaning this age population would not have been captured using workflow protocols that filter out low-U analyses (-). The Karakaya Complex is composed of metamafic and metapelitic rocks, and the rutile dataset demonstrates that low-U rutile are sourced from mafic and pelitic units (- and -). The contribution of Karakaya Complex to the basin would be underrepresented without including low-U rutile. Additionally, the U-threshold is dependent on the spot size and sensitivity of the ICP-MS used and does not adequately delineate interpretable data in a way that merits continued use. Lastly, the presence of 580-Ma grains means that those grains escaped younger high-T events, such as Variscan-related Carboniferous metamorphism (-). This supports the interpretation that the 580-Ma grains are recycled from sedimentary units, rather than derived from primary Pontide basement sources that underwent Carboniferous

metamorphism. In this way, paired rutile U-Pb dates and Zr in rutile thermometry can discriminate between potential sediment sources.

Because detrital rutile is capturing sediment input from a terrane not represented in the zircon record, detrital rutile has the potential to close the gap between the advances in zircon applicability and its limitations. For example, detrital zircon U-Pb dating, (U-Th)/He and fission track thermochronometry, and trace element and isotopic geochemistry are being performed on single grains to reconstruct the timing, tempo, and spatial extent of sedimentation, magmatism, deformation, exhumation, and crustal thickness. Rutile provides the opportunity to answer similar orogenic scale questions in areas where zircon alone is insufficient. The dataset from Anatolia demonstrates that detrital rutile provides information on sedimentation, deformation, and metamorphism. Finally, the accretion and collision of subduction complexes and oceanic plateaus has been notoriously difficult to discern with provenance techniques, often inferred from the absence of detrital zircon age modes. This work shows that detrital rutile is a promising proxy to track sediment input from accreted terranes and can be applied to convergent margins worldwide.

8 Conclusion

Sedimentary provenance analysis plays a crucial role in understanding the geodynamic, magmatic, structural, and topographic evolution of convergent margins. Detrital zircon U-Pb geochronology is a widely used technique, however, it has several limitations and can struggle to capture significant events in a convergent margin lifecycle (e.g., low grade metamorphism, mafic protoliths). Detrital rutile provides one opportunity to overcome these limitations. This study provides methods for using detrital rutile U-Pb and trace element analysis in tracking sediment input from metamorphic units using a new dataset from the Central Sakarya and Saricakaya Basins in Anatolia. We present a workflow for evaluating discordance and common Pb, which is critical for confidently interpreting age distributions. The results show that common Pb correction is important, but the choice of correction method is less influential, and that grains up to 60% discordant can be used for meaningful provenance interpretation. Using a concordance filter is more appropriate than filtering out low-U rutile. Low-U rutile comprise an important detrital population—lower grade metamorphic units and metamafic sources—that would otherwise be missed with analytical protocols that screen U concentration. Based on trace element geochemistry, these low-U rutile grains are classified as metamafic and metapelitic and predominantly have greenschist blueschist Zr in rutile temperatures, thus correspond to sediment input from the subduction accretion Karakaya Complex. Sedimentary provenance from the Karakaya Complex is poorly resolved in the detrital zircon record, further highlighting the potential of detrital rutile as an important provenance proxy in orogenic settings.

Appendix A: Sample Preparation and Analytical Methods

A.1 Sample Preparation

The samples in this study were previously separated for detrital zircon analysis. In order to extract detrital rutile, all heavy mineral fractions from post-water table separation steps were recombined and reprocessed. Then, samples were separated in heavy liquids (i.e., methylene iodide). The Frantz magnetic separator was set to 20° side

025 slope and 20° forward slope such that rutile grains were separated into the 0.7 to 1.5 amp. fraction. Rutile grains were handpicked with a Leica M205C binocular microscope using transmitted and polarized light. For samples with a small quantity of heavy mineral grains, rutile was picked from all 0.3 to >1.5 amp. magnetic fractions. Rutile grains were red-brown-yellow color in reflected light, red to opaque in plane polarized light, and displayed a resinous to vitreous luster; grains were well rounded to euhedral with many displaying twinning characteristic of rutile's tetragonal crystal system and striations parallel to the long axis. Grains were placed on Kapton tape and mounted in epoxy in 25-mm diameter cups. The mounts were polished to expose the internal structure of the grains.

030 Rutile mounts were carbon-coated and imaged with a TFS Apreo S with Lova SEM with an energy-dispersive detector (EDS) to distinguish rutile grains from other spurious heavy minerals (Figure A1). Then the epoxy mounts were polished with 1 µm and 0.25 µm grit in felt. Mounts were soaked in 2M nitric acid (HNO₃) in the ultrasonic, then in ultra-pure water in the ultrasonic to remove carbon coat remnants.

A.2 U-Pb Geochronology

035 Detrital rutile U-Pb geochronology was conducted at the Isotope Geochemistry Lab at the University of Kansas using a Thermo Element2 magnetic sector field ICP-MS coupled to a Photon Machines AnalyteG2 excimer laser ablation system (see also metadata in Table A2). We used a modified protocol from , which we optimized for low U concentrations. Because metamafic rocks, which have low U concentrations, were suspected to be an important sedimentary source, we designed a protocol to maximize U sensitivity. We spent a significant amount of time tuning acquisition parameters and opted for a laser beam diameter of 50 µm, running the secondary electron multiplier in 'both mode' to handle both the high U counts in the standards and low U counts in the unknowns, and using a long washout time of 15 seconds time to get a steady, low ²³⁸U background. Rutile unknowns were calibrated against a suite of reference materials. The data were reduced in *iolite 4*, calibrated against the R10 standard. Individual analyses with >20% discordance in ²⁰⁷Pb/²⁰⁶Pb ratios or abnormal patterns in raw signal intensity were excluded from analyses and interpretations.

040 The accuracy of the protocol was evaluated using a suite of international standards. We used R10 as the primary standard (1091.6 ± 3.5 Ma TIMS age; Luvizotto et al., 2009), and the secondary standards included Wodgina (2845.8 ± 7.8 Ma TIMS age; Ewing, 2011), Kragerø (1085.7 ± 7.9 Ma TIMS age; Kellett et al., 2018), 9826J (381.9 ± 1.1 Ma TIMS age; Kylander-Clark, 2008), and LJ04-08 (498 ± 3 Ma LA-ICP-MS age; Apen et al., 2020). Figure A2 displays the weighted mean of the uncorrected and corrected ages as the percent deviation from the published age (see also the data repository). The rutile U-Pb dates of individual sample are shown as histograms in Figure A3.

050 A.3 Trace Element Geochemistry

055 Detrital rutile trace element geochemistry was conducted at the Isotope Geochemistry Lab at the University of Kansas using a Thermo Element2 magnetic sector field ICP-MS coupled to a Photon Machines AnalyteG2 excimer laser ablation system (see also Table A2). Trace elements (⁴⁹Ti, ⁵¹V, ⁵³Cr, ⁶⁶Zn, ⁶⁹Ga, ⁹⁰Zr, ⁹³Nb, ⁹⁵Mo, ¹¹⁸Sn, ¹²¹Sb, ¹⁷⁷Hf, ¹⁸¹Ta, ¹⁸²W) were determined by ablating material from a 25–35 µm laser beam diameter with a beam energy density of 3.0 J/cm² and a repetition rate of 10 Hz. Trace element reference. (A) Kernel density estimate of all detrital

rutile dates (^{207}Pb -corrected, power law uncertainty filtered) shown alongside a compilation of all published detrital zircon ages from Upper Cretaceous to Eocene strata in Central Sakarya and Sarıcakaya Basins. Gray bars depict periods of metamorphism in western Anatolia, materials included USGS GSD-1G and USGS GSC-1G glasses (Joachim et al., 2011), and R10 rutile (Luvizotto et al., 2009). Trace element concentrations were calculated using the Trace Element routine in *iolite 4* with ^{49}Ti as an internal standard; for rutile unknowns, TiO_2 was set to be 100 mass-%. Following U-Pb and trace element analysis mounts were imaged in a SEM at University of Nevada Reno.

Trace element composition was then used to confirm that the analyzed grains are rutile. TiO_2 polymorphs rutile, brookite and anatase are argued to be optically distinct or optically indistinguishable. Either way, V, Cr, Zr, Fe, and Nb concentrations vary systematically among TiO_2 polymorphs. Discrimination diagrams of Cr versus V and V versus Zr can verify that analyzed grains are rutile. The grains from this study are plotted alongside the polymorph dataset of Triebold et al. which were classified using Raman spectrometry (Figure A4). All samples from this study plot within the range of rutile grains.

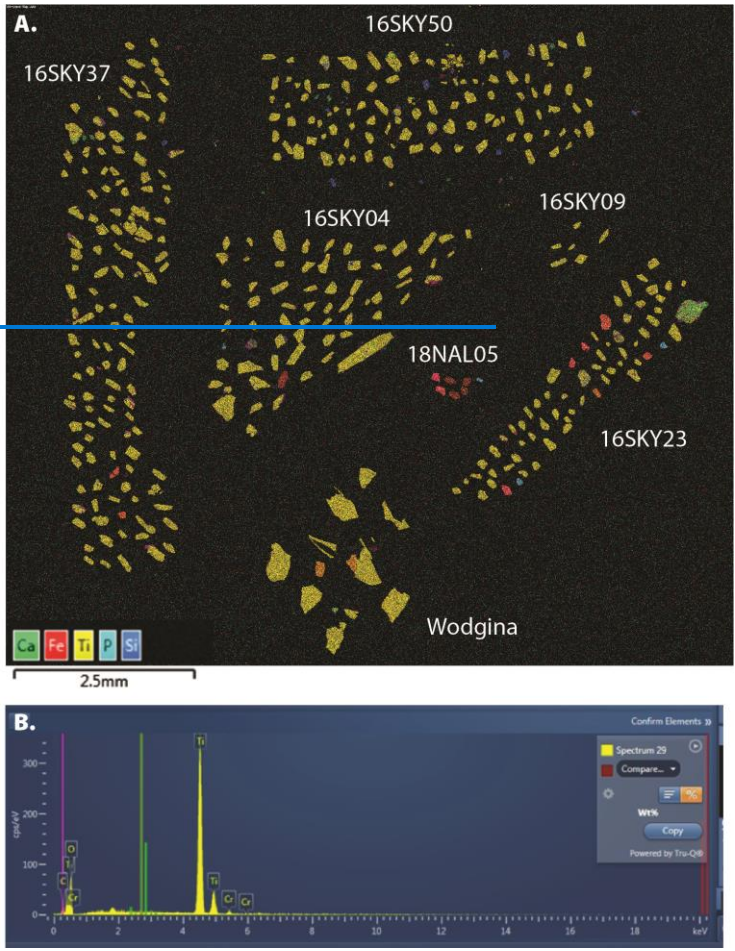
Formatted: Font: +Headings (Times New Roman)

Formatted: Font: +Headings (Times New Roman)

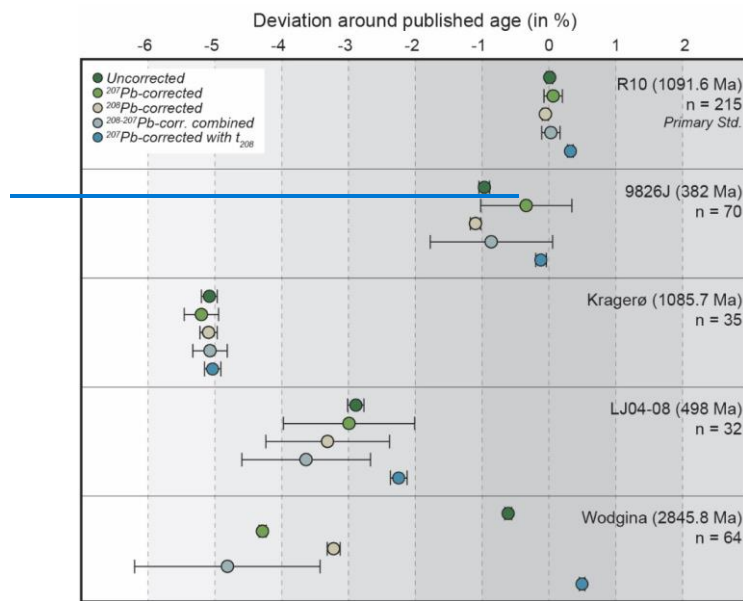
Formatted: Font: +Headings (Times New Roman)

Formatted: Font: +Headings (Times New Roman)

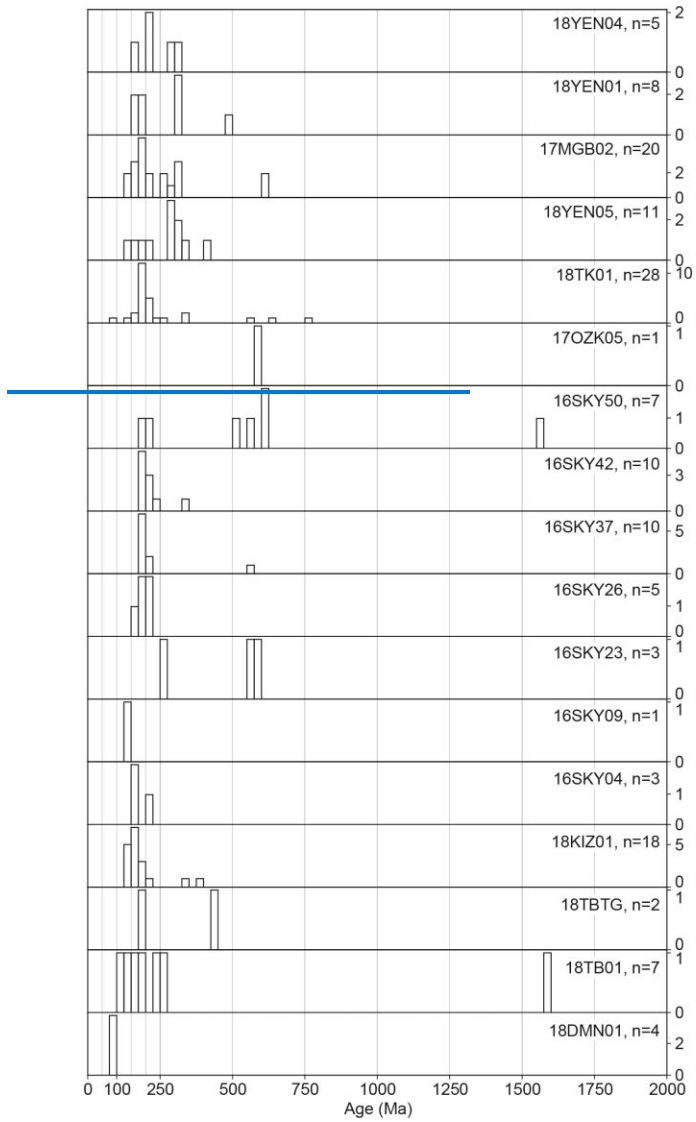
Formatted: Font: +Headings (Times New Roman)



070 *Figure A1. SEM EDS imaging of rutile grain mount 21RtF. (A) EDS elemental map where grains are colored by elements Ca, Fe, Ti, P, and Si. Rutile (TiO₂) grains are yellow, iron oxides are red, zircon are blue, and apatite are green. (B) Typical spectra of a rutile grain.*



075 *Figure A2. Deviation around the published age for the primary and secondary rutile reference materials. Circles and*
horizontal bars correspond to the weighted mean and standard deviation for analyses over all sessions. The various
correction methods are explained in the main text. Note: The final iteration of the ²⁰⁸Pb correction yields a corrected
²³⁸U/²⁰⁶Pb ratio. The combined ²⁰⁸⁻²⁰⁷Pb correction follows the ²⁰⁷Pb correction method in Tera-Wasserburg space
using the new ²⁰⁸Pb-corrected ²³⁸U/²⁰⁶Pb ratio and the original ²⁰⁷Pb/²⁰⁶Pb ratio. In general, this combined correction
method performed poorly and was not applied to detrital unknowns. Data from the figure are included in the data
repository.



085 *Figure A3. Histograms of detrital rutile U-Pb ages by sample. Histograms are 25-Myr bins and the ages shown are the ^{207}Pb correction with t_{205} . Visualized with detritalPy.*

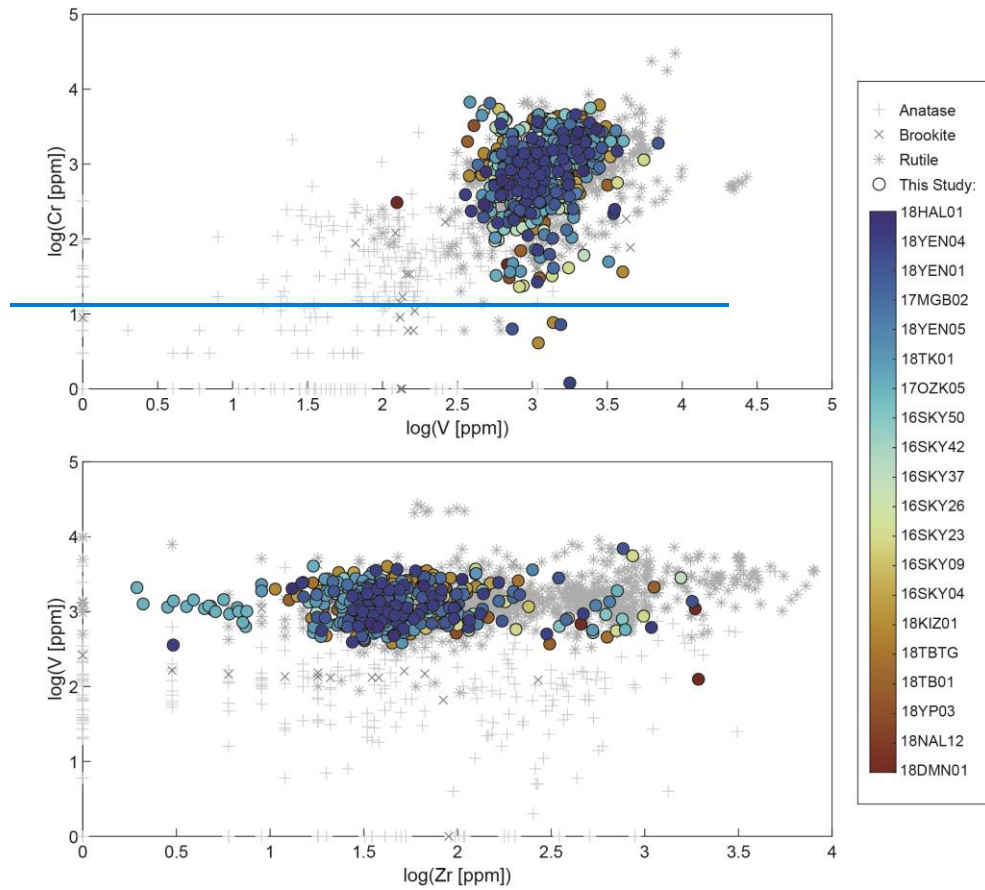


Figure A4. TiO_2 polymorph discrimination diagrams using (a) Cr versus V and (b) V versus Zr concentrations of analyzed grains. Rutile grains from this study, colored by sample, plot within the range of rutile grains identified in Triebold et al.

090

Table A1. Sample Information. IGSN: International Geo Sample Number, CSB: Central Sakarya Basin, SB: Sarıcağaya Basin. CSB and SB stratigraphic sections are from Ocakoğlu et al. and Mueller et al., respectively.

Sample Name	IGSN	Unit	Basin and Section	Stratigraphic Age	Latitude	Longitude	Sample and detrital zircon source
48DMN01	40.580524EMUE0005	Değirmenözü Fm	CSB, Okçular Section	Santonian	40.373917	30.977778	Mueller et al., 2022
48NAL12	40.580524EMUE000J	Yenipazar Fm	CSB, Nallıhan Section	Up. Camp. Mastrichtian	40.245028	31.309472	Mueller et al., 2022
48TK01	40.580524EMUE000I	Çataltepe Fm	CSB, Tarıklı Section	Paleocene-lower Eocene	40.327833	30.520861	Mueller et al., 2022
48KIZ01	40.580524EMUE000C	Kızılcay Fm	CSB, Okçular Section	Paleocene-lower Eocene	40.396667	30.962861	Mueller et al., 2022
48YEN05	40.580524EMUE000D	Kızılcay Fm	CSB, Yenipazar Section	Paleocene-lower Eocene	40.189639	30.626167	Mueller et al., 2022
48TB01	40.580524EMUE000F	Tarıklı Fm	CSB, Tarıklı Section	Paleocene-lower Eocene	40.357556	30.524444	Mueller et al., 2022
48TBTG	40.580524EMUE000G	Tarıklı Fm	CSB, Tarıklı Section	Paleocene-lower Eocene	40.355111	30.522278	Mueller et al., 2022
48YP03	40.580524EMUE000K	Yenipazar Fm	CSB, Okçular Section	Lower Paleocene	40.389556	30.990306	Mueller et al., 2022
46SKY04	40.580524EMUE0017	Mihalgazi Fm	SB, Mayıslar Section	Ypresian	40.030250	30.652306	Mueller et al., 2019
46SKY09	40.580524EMUE0019	Mihalgazi Fm	SB, Mayıslar Section	Ypresian-Lutetian	40.032250	30.651222	Mueller et al., 2019
46SKY23	40.580524EMUE001H	Mihalgazi Fm	SB, Iğdır Section	Ypresian	40.057806	30.686833	Mueller et al., 2019
46SKY26	40.580524EMUE001K	Mihalgazi Fm	SB, Iğdır Section	Ypresian-Lutetian	40.058583	30.688083	Mueller et al., 2019
46SKY37	40.580524EMUE001Q	Mihalgazi Fm	SB, Kapıkaya Section	Ypresian-Lutetian	40.072889	30.741806	Mueller et al., 2019
46SKY42	40.580524EMUE001T	Mihalgazi Fm	SB, Kapıkaya Section	Ypresian-Lutetian	40.074500	30.743944	Mueller et al., 2019
46SKY50	40.580524EMUE001W	Mihalgazi Fm	SB, Kapıkaya Section	Ypresian-Lutetian	40.078639	30.744722	Mueller et al., 2019
47OZK05	40.580524EMUE001Z	Mihalgazi Fm	SB, Ozanköy Section	Ypresian-Lutetian	40.138917	30.931111	Mueller et al., 2019
47MGB02	40.580524EMUE0007	Gemiciköy Fm	CSB, Yenipazar Section	Up. Lutetian-Low. Bartonian	40.210444	30.615528	Mueller et al., 2022
48YEN01	40.580524EMUE0008	Gemiciköy Fm	CSB, Yenipazar Section	Upper Bartonian-Priabonian	40.251000	30.534750	Mueller et al., 2022
48YEN04	40.580524EMUE0009	Güvenç Fm	CSB, Yenipazar Section	Lutetian	40.193583	30.623028	Mueller et al., 2022
48HAL01	40.580524EMUE000A	Halidiye Fm	CSB, Okçular Section	Lutetian	40.396889	30.960694	Mueller et al., 2022

1096
1097

Table A2. University of Kansas Isotope Geochemistry Lab LA-ICP-MS Metadata

Laboratory and Sample Preparation	
Laboratory name	The University of Kansas, Dept. of Geology, Isotope Geochemistry Lab
Sample type/mineral	Rutile
Sample preparation	1 in epoxy rounds
Imaging	EDS in SEM
Laser Ablation System	
Make, model & type	ATL ArF excimer laser (193 nm), Photon Machines AnalyteG2
Ablation cell & volume	HeLex 9 sample cell
Laser wavelength	193 nm
Pulse width (ns)	5 ns
Fluence	3.0 J/cm ² (77% at 5mJ output)
Repetition rate	10 Hz
Spot size (um)	Trace elements: 25 µm; U-Pb: 50 µm
Sampling mode/ pattern	Single spots
Carrier gas	He, 1.1 l/min, Ar, 1.07 l/min
Ablation duration	25s
Cell carrier gas flow	-He, 1.1 l/min
ICP-MS Instrument	
Make, Model & type	Thermo Element2 magnetic sector field ICP-MS (single collector)
Sample introduction	Aerosol with sample + He was mixed with Ar using a T-connector 15 cm upstream from torch
RF power	1200–1250 W
Make up gas flow	Ar, 1.07 l/min
Sampling depth	ea. 20 µm
Detection system	single detector (SEM), counting & analog modes
Elements/ isotopes analyzed	Trace elements: 49Ti, 51V, 53Cr, 56Fe, 66Zn, 69Ga, 90Zr, 93Nb, 95Mo, 118Sn, 121Sb, 177Hf, 181Ta, 182W, U-Pb: 206Pb, 207Pb, 208Pb, 232Th, 238U
Integration time per channel (Sample Time)	Trace elements: 49Ti=3 ms, 90Zr=20 ms, and 10 ms for all other isotopes; U-Pb: 206=8 ms, 207=10 ms, 208=2 ms, 232=2 ms, 238=4 ms
Total integration time (Segment Duration)	Trace elements: 49Ti=9 ms, 90Zr=20 ms, and 10 ms for all other isotopes; U-Pb: 206Pb=32 ms, 207Pb=40 ms, 208Pb=8 ms, 232Th=8 ms, 238U=20 ms
Total method time	Trace elements: 40s (120 runs, 1 pass); U-Pb: 31s (100 runs, 3 passes)
ICP Dead time	6 ns
UO+/U+	≤0.25%
232Th+/238U+	≥0.75
Data Processing	
Gas blank	Trace elements: 7–15 s, U-Pb: 7–15 s
Calibration strategy	Trace elements: standard sampling bracketing + internal standardization assuming 100% TiO ₂ ; U-Pb: standard sampling bracketing
Reference material info	Trace elements: GSD-1G (Guillong et al., 2005; Jochem et al., 2005); U-Pb: R10 (Luvizotto et al., 2009)
Internal std for trace elements	49Ti

Data processing package used/ Correction for LIEF	Iolite 4 (Paton et al., 2011); Trace elements: Trace Elements data reduction scheme; U-Pb: U-Pb Geochronology data reduction scheme; exponential LIEF correction for U-Pb ratios.
Common Pb correction, composition and uncertainty	See text for discussion.
Uncertainty level & propagation	Trace elements: 2 σ internal uncertainty; U-Pb: 2 σ propagated uncertainty from U-Pb Geochronology data reduction scheme. Concordia diagrams were plotted using IsoplotR (Vermeesch, 2018) with 2 σ uncertainty ellipses
Reproducibility	Trace elements: 5–7%, U-Pb ratios: 2–4%
Quality control/ Validation	Trace elements: R10 (Luvizotto et al., 2009) and GSC-1G (Guillong et al., 2005; Jochum et al., 2005); U-Pb: Wodgina (Ewing, 2011), Kragers (Kellett et al., 2018), 9826J (Kylander-Clark, 2008), L104-08 (Apen et al., 2020)

Appendix B: Additional Principal Component Analysis Information

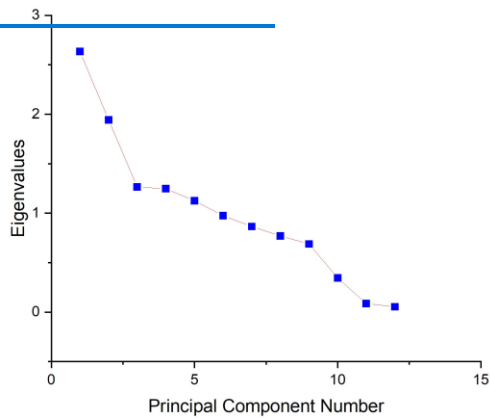


Figure B1. Principal component analysis scree plot displaying the eigenvalues for each principal component. Data are in Table B2.

Table B1. Principal Component Analysis—Correlation Matrix

10	V	Cr	Zn	Ga	Zr	Nb	Mo	Sn	Sb	Hf	Ta	W
V	1	0.28702	0.08471	-0.00424	0.05335	-0.09225	-0.04913	0.30235	-0.10058	0.14697	-0.06449	0.11768
Cr	0.28702	1	0.00721	-0.06293	-0.02758	-0.14992	-0.0576	0.13129	-0.11661	0.02323	-0.18616	0.02185
Zn	0.08471	0.00721	1	0.20306	-6.68E-04	-0.06795	0.00211	0.10389	-0.02017	-0.02065	-0.07042	-0.01978

Ga	-0.00424	-0.06293	0.20306	‡	0.02637	-0.01569	-0.0019	0.11868	-0.00756	0.03545	-0.02975	0.04133
Zr	0.05335	-0.02758	-6.68E-04	0.02637	‡	0.14416	0.23746	3.63E-01	-0.02579	0.93181	0.13945	0.17929
Nb	-0.09225	-0.14992	-0.06795	-0.01569	0.14416	‡	-0.00703	0.14644	0.06101	0.15243	0.90801	0.13124
Mo	-0.04913	-0.0576	0.00211	-0.0019	0.23746	-0.00703	‡	0.45606	-0.01226	0.14038	-0.02039	0.11896
Sn	0.30235	0.13129	0.10389	0.11868	3.63E-01	0.14644	0.45606	‡	0.11909	0.35819	0.15676	0.23521
Sb	-0.10058	-0.11661	-0.02017	-0.00756	-0.02579	0.06101	-0.01226	0.11909	‡	-0.03755	0.09806	0.06319
Hf	0.14697	0.02323	-0.02065	0.03545	0.93181	0.15243	0.14038	0.35819	-0.03755	‡	0.13769	0.26427
Ta	-0.06449	-0.18616	-0.07042	-0.02975	0.13945	0.90801	-0.02039	0.15676	0.09806	0.13769	‡	0.06838
W	0.11768	0.02185	-0.01978	0.04133	0.17929	0.13124	0.11896	0.23521	0.06319	0.26427	0.06838	‡

Table B2. Principal Component Analysis—Eigenvalues of the Correlation Matrix

	Eigenvalue	Percentage of Variance	Cumulative
1	2.63379	21.95%	21.95%
2	1.94337	16.19%	38.14%
3	1.26467	10.54%	48.68%
4	1.24705	10.39%	59.07%
5	1.12556	9.38%	68.45%
6	0.97551	8.13%	76.58%
7	0.86476	7.21%	83.79%
8	0.77053	6.42%	90.21%
9	0.68894	5.74%	95.95%
10	0.345	2.87%	98.83%
11	0.0868	0.72%	99.55%
12	0.05402	0.45%	100.00%

Table B3. Principal Component Analysis—Extracted Eigenvectors

	Coefficients of PC1	Coefficients of PC2	Coefficients of PC3	Coefficients of PC4	Coefficients of PC5
V	0.11188	0.32574	0.5509	0.18163	0.00963
Cr	-0.02241	0.33015	0.54321	-0.00609	0.08221
Zn	0.00128	0.1495	-0.09679	0.56211	-0.35561
Ga	0.04679	0.07679	-0.24684	0.52186	-0.39737
Zr	0.49771	0.16248	-0.18544	-0.30947	-0.25365
Nb	0.3141	-0.54281	0.24962	0.12009	-0.0531
Mo	0.24009	0.15855	-0.34487	0.10349	0.48557
Sn	0.40793	0.20734	0.04078	0.32142	0.3218
Sb	0.04322	-0.15434	-0.20528	0.19598	0.42865
Hf	0.50092	0.18027	-0.08342	-0.30607	-0.28105
Ta	0.30613	-0.55267	0.24494	0.12582	-0.0438
W	0.2605	0.07567	0.06886	0.08088	0.19405

1112
1113 **Data availability**

1114 The detrital rutile trace element and U-Pb raw data, results and Pb correction methods; rutile U-Pb reference material
1115 raw data and results; and statistical comparison of Pb correction methods are stored in an Open Science Framework data
1116 repository that can be accessed at <https://doi.org/10.17605/OSF.IO/A4YE5>. Analyses and plots were performed in MATLAB
1117 .

1118 **Author contributions**

1119 MAM conceptualized the project; MAM and AM performed the formal data analysis; MAM and AL acquired
1120 funding; all authors were involved in the investigation; MAM, AL, and AM developed the methodology; MAM and AM
1121 performed the validation; MAM completed the data visualizations; MAM wrote the original draft; all authors reviewed and
1122 edited the manuscript.

1123 **Competing interests**

1124 The authors declare that they have no conflict of interest.

1125 **Disclaimer**

1126 Publisher's note: Copernicus Publications remains neutral with regard to jurisdictional claims in published maps and
1127 institutional affiliations.

1128 **Acknowledgements**

1129 We thank Çelik Oeakoğlu, Jan Westerweel, Kate Huntington, Alison Duvall, Sean Muleahy, Scott Braswell, Joel
1130 DesOrmeau, Scott Dakins, and Eric Steig for support in the field and lab. We thank Andrew Kylander Clark, Francisco Apen,
1131 and Peter Downes for reference materials and Margo Odum and Eirini Poulaki for discussions on U-Pb data reduction. We
1132 thank the *iolite* team for student access.

Formatted: Font: +Headings (Times New Roman)

Formatted: Font: +Headings (Times New Roman)

Formatted: Font: +Headings (Times New Roman), Font color: Black

Formatted: Normal, Indent: First line: 0.5", Border: Top: (No border), Bottom: (No border), Left: (No border), Right: (No border), Between : (No border)

Formatted: Font: +Headings (Times New Roman)

Formatted: Font: +Headings (Times New Roman)

Formatted: Normal, Indent: First line: 0.5", Border: Top: (No border), Bottom: (No border), Left: (No border), Right: (No border), Between : (No border)

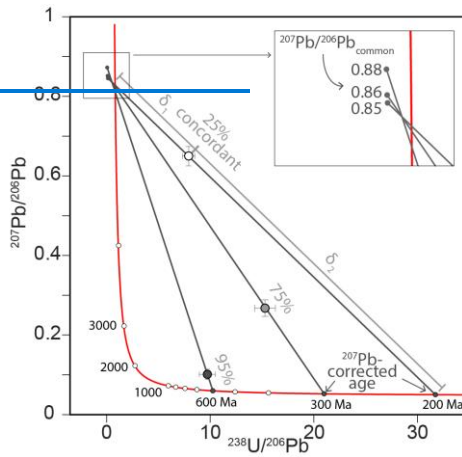
Formatted: Font: +Headings (Times New Roman), Font color: Black

1133 **Financial support**

1134 This work was funded by the University of Washington Department of Earth and Space Sciences and NSF EAR-
1135 1543684 and EAR-2141115.

1136 **References**

1137



1138
1139 *Figure : Conceptual schematic of the ^{207}Pb correction in Tera-Wasserburg space. First, the common $^{207}\text{Pb}/^{206}\text{Pb}$ ratio is calculated from*
1140 *the initial date estimate (i.e., t_1 or t_{208} ; see text for details). Next, a discordia is fitted between $^{207}\text{Pb}/^{206}\text{Pb}_{\text{common}}$ and the data point.*
1141 *Then, the lower intersection of the line with the concordia marks the corrected $^{238}\text{U}/^{206}\text{Pb}$ and $^{207}\text{Pb}/^{206}\text{Pb}$, which are used to*
1142 *calculate the ^{207}Pb corrected date. Concordance is defined as the distance along the discordia between the upper and lower intersections*
1143 *of the discordia with the concordia (Eqn. 7).*

Formatted: Font: +Headings (Times New Roman)

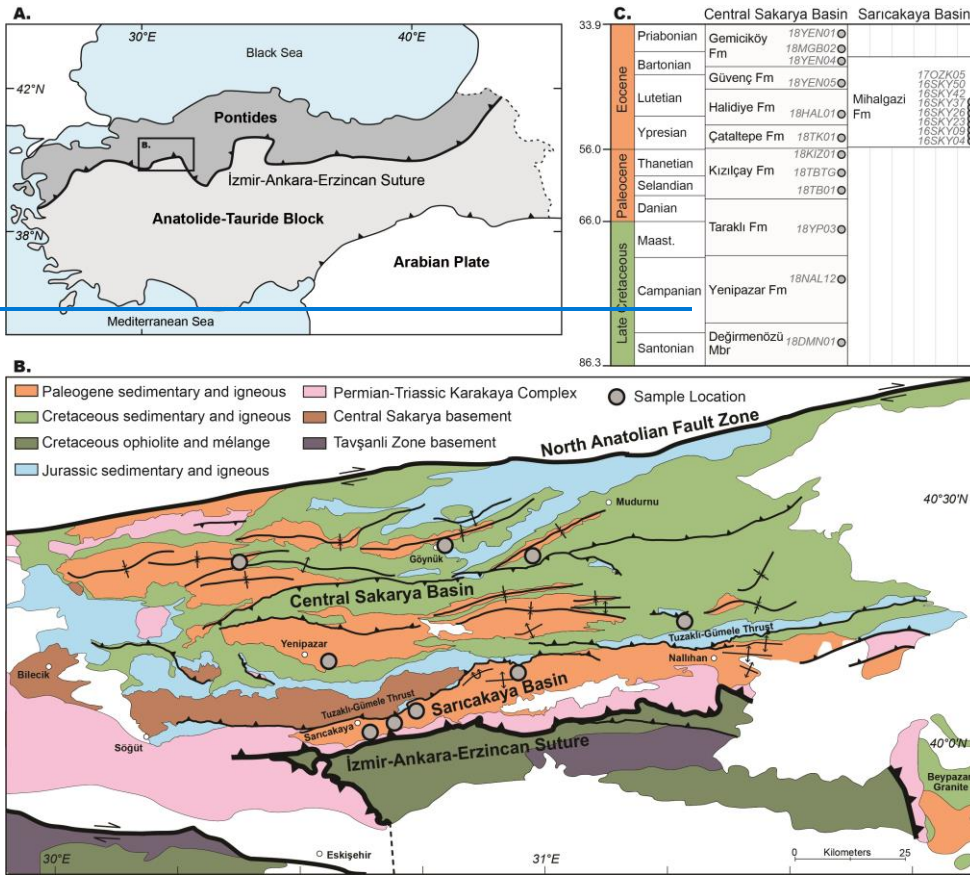


Figure 2: (A) Simplified terrane map of Anatolia and (B) geologic map of the Central Sakarya Basin and Sarıcakaya Basin region (after Aksay et al., 2002). (C) Simplified stratigraphic correlation chart and schematic sample distribution. Stratigraphy after Ocakoğlu et al. (2018).

Formatted: Font: (Default) +Headings (Times New Roman), Not Italic, English (United Kingdom)

Formatted: Font: +Headings (Times New Roman), Bold, Not Italic

Formatted: Font: +Headings (Times New Roman), Not Italic

Formatted: Font: +Headings (Times New Roman), Bold, Not Italic

Formatted: Font: +Headings (Times New Roman), Not Italic

Formatted: Font: +Headings (Times New Roman), Bold, Not Italic

Formatted: Font: +Headings (Times New Roman), Not Italic

Formatted: Default Paragraph Font, Font: (Default) +Headings (Times New Roman), Bold

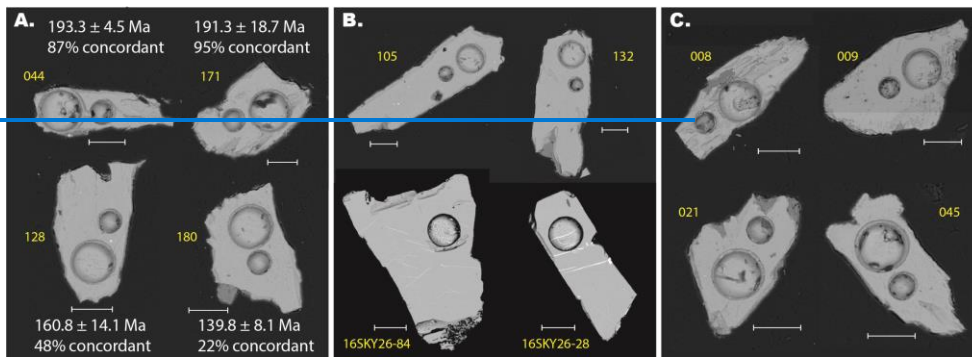
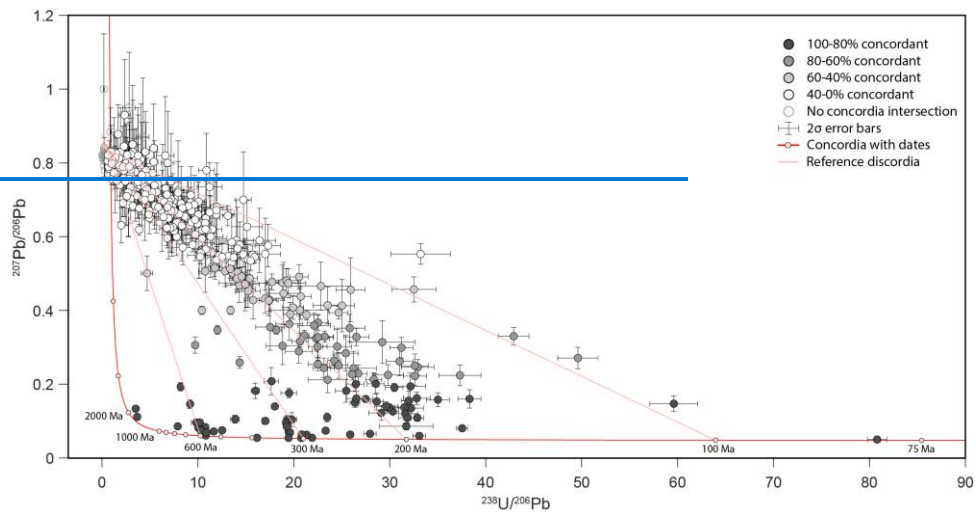


Figure : SEM BSE images of representative rutile grains. All grains are from sample 18TK01 unless otherwise noted; the grain number is in yellow. Ablation pits are from U-Pb analysis (larger) and trace element analysis (smaller). (A) Rutile analyses with acceptable U-Pb dates across a range of concordance. U-Pb date and concordance is from $^{207}\text{Pb}_c$ correction method. (B) Rutile analyses rejected because of inclusions (top) or exsolution lamellae (bottom). (C) Rutile analyses discarded for anomalous signal intensity (spiky signal). The scale bar is 50 μm .

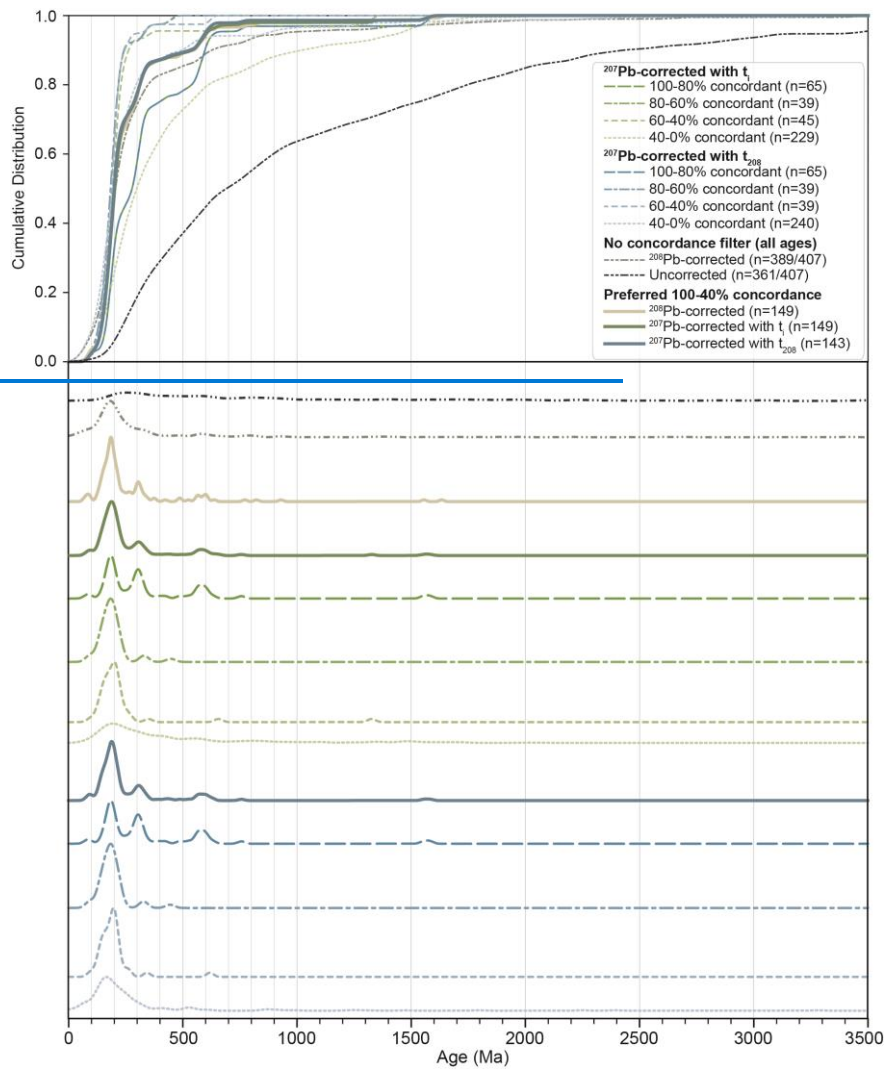
Formatted: Font: +Headings (Times New Roman), Not Italic

Formatted: Font: +Headings (Times New Roman), Not Italic, Pattern: Clear

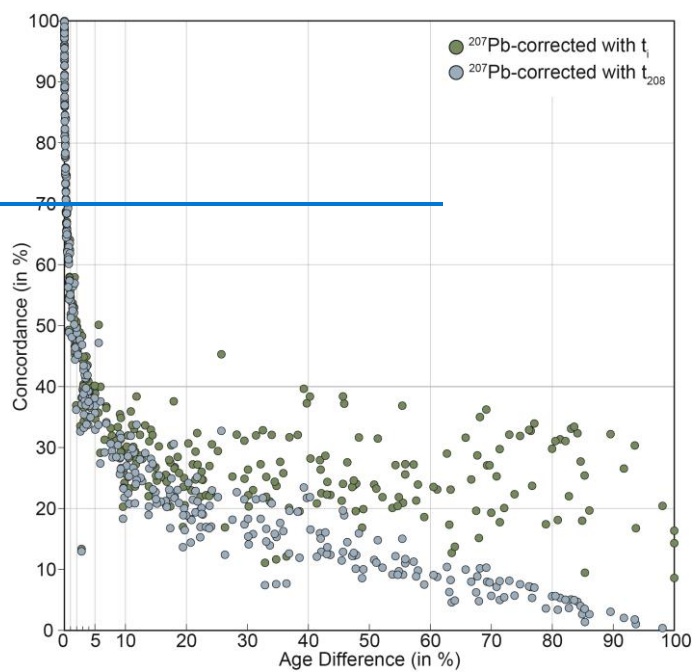
Formatted: Font: +Headings (Times New Roman), Not Italic, Pattern: Clear, Highlight



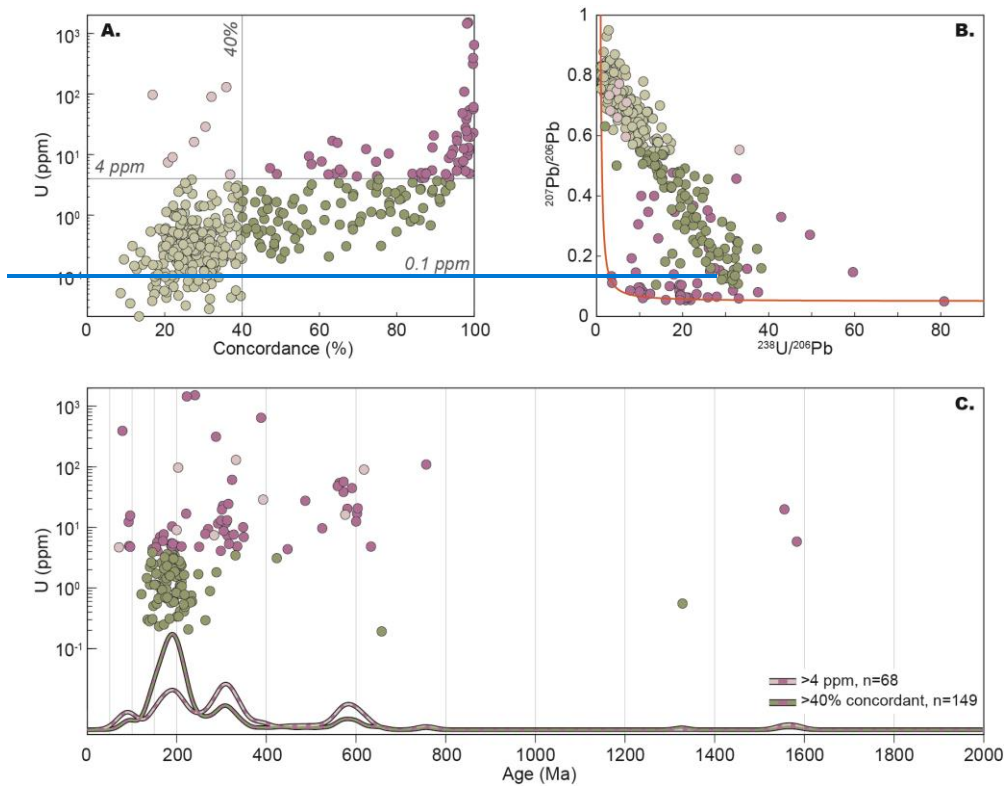
1156
 1157 *Figure : Detrital rutile U-Pb results displayed in Tera-Wasserburg space. Data points are colored by discordance bins, error bars are 2 σ .*
 1158 *Shown for reference are discordia lines towards lower intercepts at 100, 200, 300, and 600 Ma (pink lines).*



1160 *Figure : Distributions of dates of all samples together shown as kernel density estimates (KDEs) and cumulative distribution functions*
1161 *visualized with detritalPy. Uncorrected and corrected data are separated into concordance bins. Solid line KDEs represent the data with*
1162 *our preferred 100-40% concordance range.*

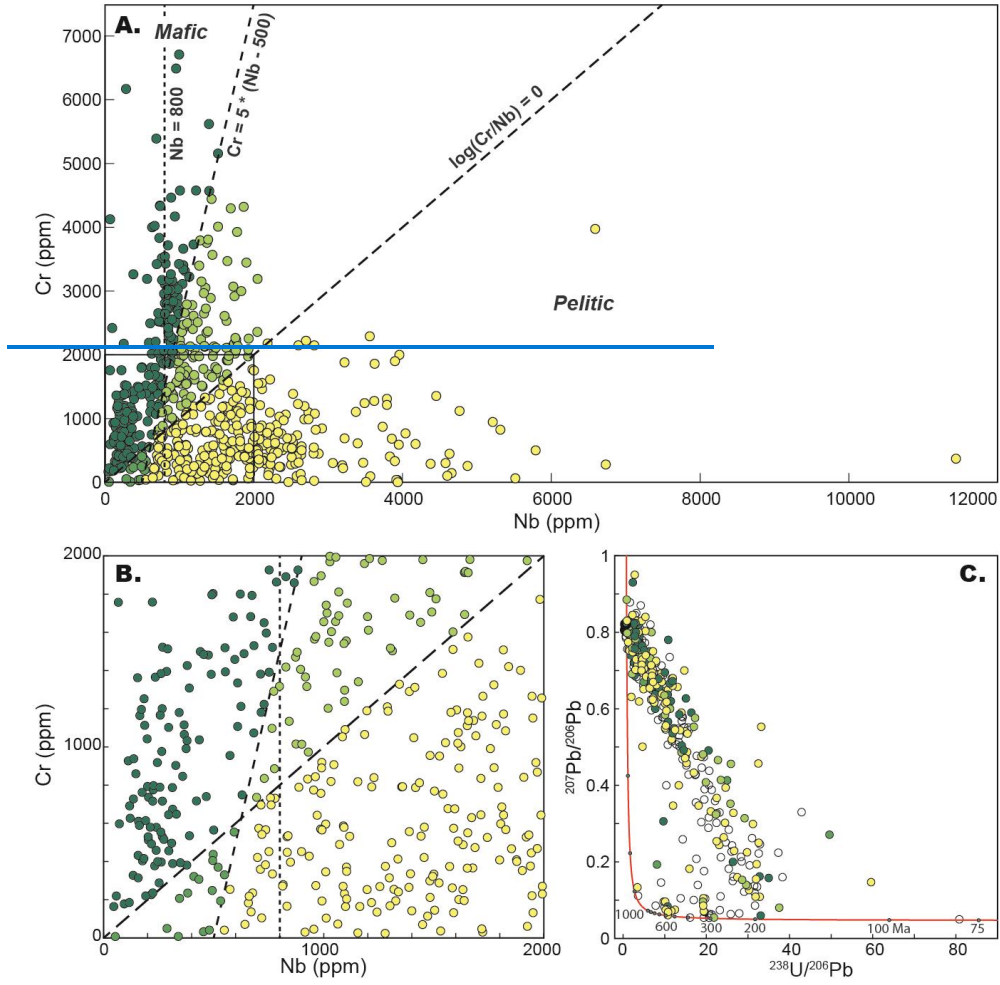


1164 *Figure : Concordance versus the difference in ^{207}Pb -corrected dates using t_1 or t_{208} . The largest differences in age are for grains that are*
1165 *less than 40% concordant.*

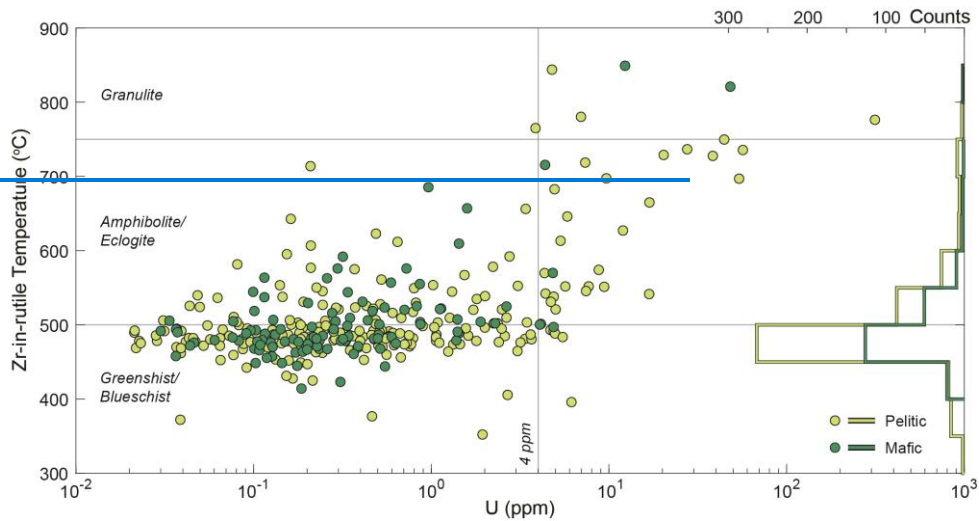


1168
 1169 *Figure 1: Comparison of detrital rutile filtering based on U concentration or concordance. (A) Rutile U concentration versus*
 1170 *percent concordance. U threshold filtering includes all grains greater than 4 ppm (pink colors), whereas concordance-*
 1171 *threshold filtering includes grains greater than 40% (dark pink and dark green colors). (B) Rutile U-Pb results in Tera-*
 1172 *Wasserburg space following the color scheme in panel A. (C) Rutile U concentration versus $^{207}\text{Pb}/^{206}\text{Pb}$, corrected U-Pb date. The*
 1173 *KDEs display the date spectra from the different filtering protocols. Rutile with less than 4 ppm and less than 40% concordance*
 1174 *are excluded by both filters and not included in panel C.*

Formatted: Font: +Headings (Times New Roman), Not Italic, Font color: Black



1175
 1176 *Figure 1: Cr versus Nb discrimination diagrams for detrital rutile from this study (A and B). Dashed lines demarcate proposed boundaries*
 1177 *between mafic and pelitic source fields. Rutile grains are colored by their respective source field. (C) Rutile analyses in Tera-Wasserburg*
 1178 *space reveal mixed source lithologies in each date mode. Unfilled circles are rutile U-Pb analyses without trace element data.*



1179
 1180 *Figure: Zr in rutile temperature versus U concentration. Mafic and pelitic scores are from the Triebold et al. (2012) discrimination (i.e.,*
 1181 *$Cr = 5 * [Nb - 500]$); mafic grains include the combined dark green colors from and pelitic include the light green and yellow colors. Zr-*
 1182 *in-rutile temperatures follow the Kohn (2020) calibration. The histogram shows the distribution of mafic and pelitic grains by*
 1183 *temperature. Note that not all analyses have both U and TRLE data, therefore there are fewer grains represented in the scatter plot than in*
 1184 *the histogram and A.*

Formatted: Default Paragraph Font, Font: (Default) +Headings (Times New Roman)

Formatted: Default Paragraph Font, Font: (Default) +Headings (Times New Roman), Font color: Black

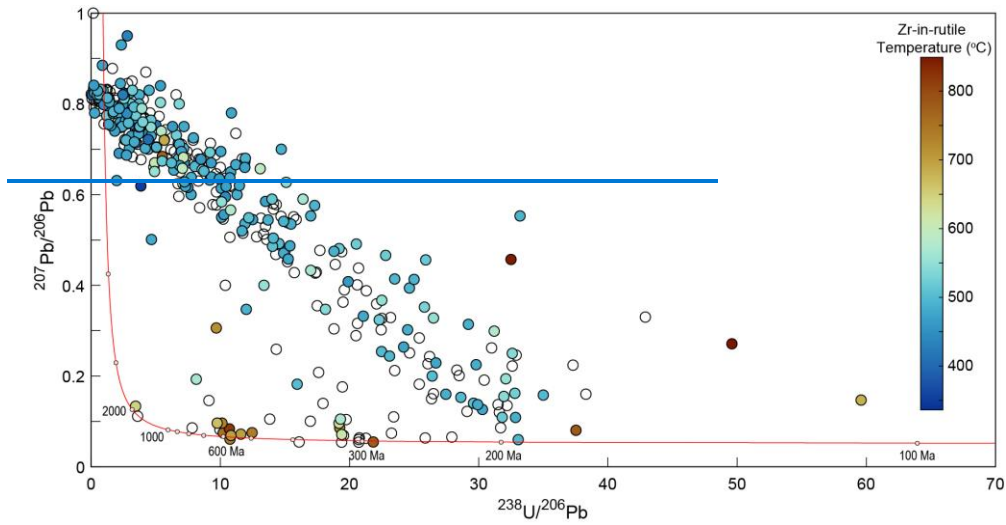


Figure : Rutile U-Pb results in Tera-Wasserburg space colored by Zr-in-rutile temperature calculated from the Kohn (2020) calibration. The mode centered around 95 Ma has the highest temperatures, and modes centered around 310 Ma and 580 Ma also contain high temperatures, whereas the 190 Ma mode is predominantly composed of lower temperature grains. Unfilled circles are rutile U-Pb analyses without trace element data. Colormap is from Crameri (2020).

Formatted: Default Paragraph Font, Font: (Default) +Headings (Times New Roman)
 Formatted: Font: +Headings (Times New Roman), Not Italic

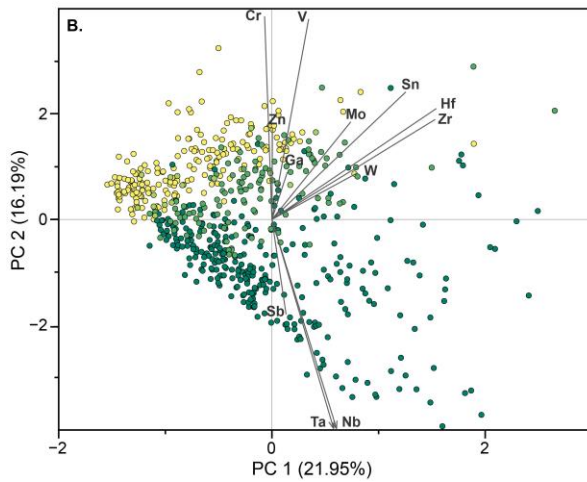
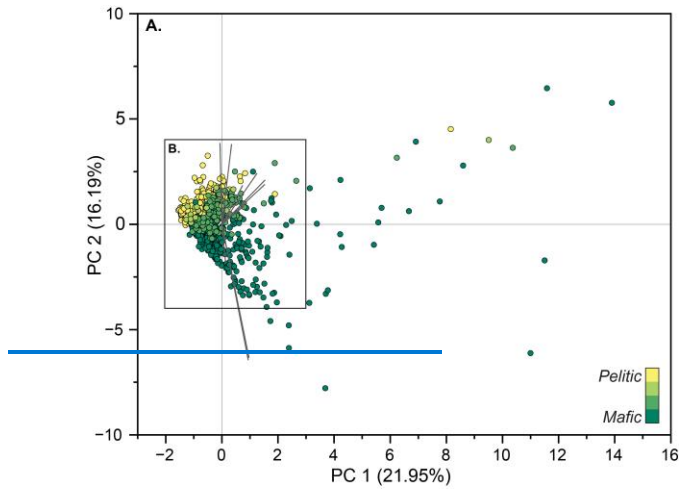


Figure - PCA score and loadings plot of principal components 1 and 2, which cumulatively explain 38.14% of trace element variance. Sample points are colored by mafic and pelitic scores from Cr/Nb discrimination shown in [Figure 1](#). The variance in trace element chemistry is best explained by metamorphic grade (PC 1) and protolith (PC 2).

Formatted: Font: +Headings (Times New Roman), Not Italic

Formatted: Default Paragraph Font, Font: (Default) +Headings (Times New Roman)

Formatted: Default Paragraph Font, Font: (Default) +Headings (Times New Roman), Font color: Black

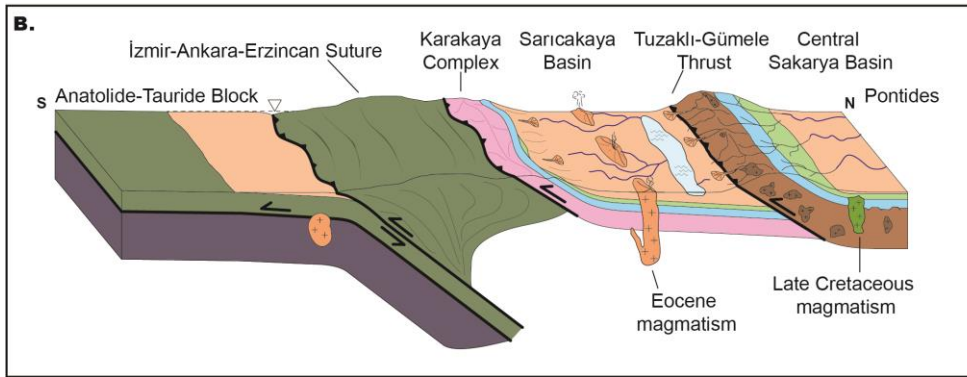
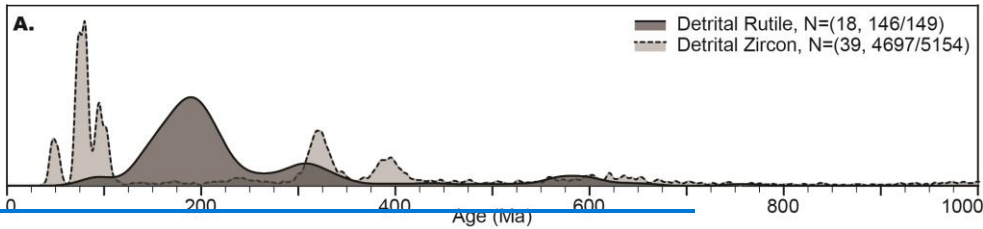


Figure .(A) Kernel density estimate of all detrital rutile ages ($^{207}\text{Pb}_n$ -corrected) shown alongside a compilation of all published detrital zircon ages from Upper Cretaceous to Eocene strata in Central Sakarya and Sarıcakaya Basins. (B) Schematic reconstruction of northwestern Anatolia in the Eocene during continental collision (after Mueller et al., 2019). The main sources of sediment to the basins were the Karakaya Complex exposed in the suture zone, Pontides crystalline basement exposed along the Tuzaklı-Gümele Thrust, Cretaceous-Eocene igneous units, and recycled sedimentary units. A: Alpine metamorphism, C: Cimmerian metamorphism, V: Variscan metamorphism.

Formatted: Font: +Headings (Times New Roman), Font color: Black

Formatted: Font: +Headings (Times New Roman)

Formatted: Font: +Headings (Times New Roman), Font color: Black

9 Conclusions

This work provides a systematic exploration of the data reduction and processing workflows for detrital rutile U-Pb geochronology using a new dataset from the Central Sakarya and Sarıcakaya Basins in Anatolia. Provenance interpretations are made from combining U-Pb dates and trace element geochemistry. The results have several implications for navigating workflows and interpretations in common Pb bearing detrital minerals:

(1) Natural datasets can be complex. While attempting a large- n provenance study, a significant number of analyses were discarded due to unacceptable U-Pb signal intensity and stability, namely low U, low Pb, and inclusions. This hurdle is evidently not unique to this dataset and should always be reported in detrital rutile U-Pb geochronology. Advances are needed to determine the best path forward, such as analyzing more grains for achieving large- n detrital rutile U-Pb datasets and more

1212 [rigorous data reporting and standardizing metrics used for evaluating 'acceptable' U-Pb analyses. We recommend that the](#)
1213 [criteria for data rejection be explicitly discussed in all detrital rutile studies.](#)

1214 (2) [We provide a method for evaluating the potential bias in U-Pb data rejection and filtering by comparing the detrital](#)
1215 [rutile grains with both U-Pb and trace element data to those with only trace element data. The U-Pb rejected and filtered out](#)
1216 [grains have a similar trace element distribution in terms of Zr-in-rutile temperature and mafic-pelitic classification to those](#)
1217 [with acceptable U-Pb analyses, suggesting there is not significant bias from U-Pb data rejection and filtering.](#)

1218 (3) [The \$^{208}\text{Pb}\$ and \$^{207}\text{Pb}\$ correction methods produce similar age spectra and do not change the final provenance](#)
1219 [interpretations. Similarly, the uncertainty filters—based on U-Pb ratio uncertainty and corrected date uncertainty—produce](#)
1220 [similar date spectra. The power law uncertainty filter is preferred because it does not alter the date distribution and includes](#)
1221 [the most grains.](#)

1222 (4) [There has not been an agreed upon metric to quantify discordance in common Pb minerals. We evaluate the](#)
1223 [Stacey-Kramers and Aitchison distance metrics and recommend the Stacey-Kramers distance as a suitable metric for](#)
1224 [quantifying discordance. However, because reliable interpretations can be made from analyses with significant proportions of](#)
1225 [common Pb, we recommend not applying a discordance filter to common Pb detrital minerals.](#)

1226 (5) [In some labs and geographic locations, only rutile above a certain uranium concentration \(i.e., 4-5 ppm U\) are](#)
1227 [analyzed for U-Pb. We demonstrate that excluding low-U rutile biases provenance interpretations toward grains with pelitic](#)
1228 [classification, higher Zr-in-rutile temperatures, and higher concordance, and changes the overall date distribution, especially](#)
1229 [the amplitude of date peaks.](#)

1230 (6) [A significant challenge in provenance work is pinpointing the signature of sediment recycling. Here we use paired](#)
1231 [U-Pb dates and Zr-in-rutile temperatures to identify polycyclic detrital rutile grains. The recycled grains preserve U-Pb dates](#)
1232 [that indicate that they escaped younger metamorphic reheating events of the crystalline basement by already being eroded and](#)
1233 [deposited in sedimentary units. In this way, detrital rutile petrochronology can address problems of sediment recycling.](#)

1234 (7) [The data processing workflows used here are provided as code in Jupyter Notebooks that can be used by future](#)
1235 [studies. The code includes common Pb corrections, uncertainty filters, discordance calculations, principal component analysis](#)
1236 [of trace element data, and other trace element plots. The provided code is one path forward to achieving the required](#)
1237 [documentation and unification of data reduction approaches.](#)

1238 **[Data and code availability](#)**

1239 [All of the data generated in this manuscript are publicly archived and available in an Open Science Framework data](#)
1240 [repository that can be accessed at <https://doi.org/10.17605/OSF.IO/A4YE5> \(Mueller et al., 2023\). The data repository also](#)
1241 [includes the supporting information text. Jupyter Notebooks containing the Python and R code used for data reduction and](#)
1242 [visualization are open and available at <https://zenodo.org/doi/10.5281/zenodo.10636727> \(Mueller, 2024\).](#)

Author contributions

MAM conceptualized the project; MAM and AL acquired funding; all authors were involved in the investigation; MAM and AM performed the formal data collection; all authors contributed to writing and revising the manuscript.

Formatted: Font: +Headings (Times New Roman)

Competing interests

The authors declare that they have no conflict of interest.

Formatted: Font: +Headings (Times New Roman)

Formatted: Font: +Headings (Times New Roman), Font color: Black

Formatted: Normal, Indent: First line: 0.5", Border: Top: (No border), Bottom: (No border), Left: (No border), Right: (No border), Between : (No border)

Disclaimer

The software described here is provided under the Apache License, Version 2.0. It is provided "as is," without warranty of any kind, express or implied, including but not limited to the warranties of merchantability, fitness for a particular purpose, and noninfringement. In no event shall the authors or copyright holders be liable for any claim, damages, or other liability, whether in an action of contract, tort, or otherwise, arising from, out of, or in connection with the software or the use or other dealings in the software.

Formatted: Font: +Headings (Times New Roman)

Acknowledgements

We thank Çelik Ocakoğlu, Jan Westerweel, Kate Huntington, Alison Duvall, Scott Braswell, Joel DesOrmeau, Sean Mulcahy, Scott Dakins, and Eric Steig for support in the field and lab. We thank Andrew Kylander-Clark, Francisco Apen, and Peter Downes for reference materials and Stuart Thomson, Margo Odium, Eirini Poulaki, and Drew Levy for discussions on common Pb corrections. We thank Associate Editor Pieter Vermeesch and referees David Chew, Laura Bracciali and Ines Pereira for thoughtful reviews that improved the manuscript. We thank the *iolite* team for student access.

Formatted: Font: +Headings (Times New Roman)

Formatted: Normal, Indent: First line: 0.5", Border: Top: (No border), Bottom: (No border), Left: (No border), Right: (No border), Between : (No border)

Formatted: Font: +Headings (Times New Roman), Font color: Black

Financial support

This work was funded by the University of Washington Department of Earth and Space Sciences and NSF EAR-1543684 and EAR-2141115.

Formatted: Font: +Headings (Times New Roman)

References

Açikalın, S., Ocakoğlu, F., Yılmaz, İ. Ö., Vonhof, H., Hakyemez, A., and Smit, J.: Stable isotopes and geochemistry of a Campanian–Maastrichtian pelagic succession, Mudurnu–Göynük Basin, NW Turkey: Implications for palaeoceanography, palaeoclimate and sea-level fluctuations, *Palaeogeogr. Palaeoclimatol. Palaeoecol.*, 441, 453–466, <https://doi.org/10.1016/j.palaeo.2015.10.005>, 2016.

- 1268 Aitchison, J.: The Statistical Analysis of Compositional Data, *J. R. Stat. Soc. Ser. B Methodol.*, 44, 139–177, 1982.
- 1269 Aksay, A., Pehlivan, Ş., Gedik, I., Bilginer, E., Duru, M., Akbaş, B., and Altun, I.: Geologic map of Turkey (Zonguldak, Scale
1270 1:500,000), Maden Tetkik ve Arma Genel Müdürlüğü, Ankara, Turkey, 2002.
- 1271 Andersen, T.: Correction of common lead in U–Pb analyses that do not report 204Pb, *Chem. Geol.*, 192, 59–79,
1272 [https://doi.org/10.1016/S0009-2541\(02\)00195-X](https://doi.org/10.1016/S0009-2541(02)00195-X), 2002.
- 1273 Angiboust, S. and Harlov, D.: Ilmenite breakdown and rutile-titanite stability in metagranitoids: Natural observations and
1274 experimental results, *Am. Mineral.*, 102, 1696–1708, <https://doi.org/10.2138/am-2017-6064>, 2017.
- 1275 Apen, F. E., Rudnick, R. L., Cottle, J. M., Kylander-Clark, A. R. C., Blondes, M. S., Piccoli, P. M., and Seward, G.: Four-
1276 dimensional thermal evolution of the East African Orogen: accessory phase petrochronology of crustal profiles through the
1277 Tanzanian Craton and Mozambique Belt, northeastern Tanzania, *Contrib. Mineral. Petrol.*, 175, 97,
1278 <https://doi.org/10.1007/s00410-020-01737-6>, 2020.
- 1279 Blackburn, T. J., Bowring, S. A., Perron, J. T., Mahan, K. H., Dudas, F. O., and Barnhart, K. R.: An Exhumation History of
1280 Continents over Billion-Year Time Scales, *Science*, 335, 73–76, <https://doi.org/10.1126/science.1213496>, 2012.
- 1281 Blum, M. and Pecha, M.: Mid-Cretaceous to Paleocene North American drainage reorganization from detrital zircons,
1282 *Geology*, 42, 607–610, <https://doi.org/10.1130/G35513.1>, 2014.
- 1283 Bracciali, L.: Coupled Zircon-Rutile U-Pb Chronology: LA ICP-MS Dating, Geological Significance and Applications to
1284 Sediment Provenance in the Eastern Himalayan-Indo-Burman Region, *Geosciences*, 9, 467,
1285 <https://doi.org/10.3390/geosciences9110467>, 2019.
- 1286 Bracciali, L., Parrish, R. R., Horstwood, M. S. A., Condon, D. J., and Najman, Y.: UPb LA-(MC)-ICP-MS dating of rutile:
1287 New reference materials and applications to sedimentary provenance, *Chem. Geol.*, 347, 82–101,
1288 <https://doi.org/10.1016/j.chemgeo.2013.03.013>, 2013.
- 1289 Campbell, C. F.: Tectonic Evolution of the Izmir-Ankara Suture Zone in Northwest Turkey using Zircon U-Pb Geochronology
1290 and Zircon Lu-Hf Isotopic Tracers, M.S., University of Kansas, United States -- Kansas, 99 pp., 2017.
- 1291 Campbell, C. F., Mueller, M. A., Taylor, M. H., Ocakoğlu, F., Möller, A., Métais, G., Coster, P. M. C., Beard, K. C., and Licht,
1292 A.: The Geodynamic Implications of Passive Margin Subduction in Northwest Turkey, *Geochem. Geophys. Geosystems*, 24,
1293 e2022GC010481, <https://doi.org/10.1029/2022GC010481>, 2023.
- 1294 Candan, O., Çetinkaplan, M., Oberhänsli, R., Rimmelé, G., and Akal, C.: Alpine high-P/low-T metamorphism of the Afyon
1295 Zone and implications for the metamorphic evolution of Western Anatolia, Turkey, *Lithos*, 84, 102–124,
1296 <https://doi.org/10.1016/j.lithos.2005.02.005>, 2005.
- 1297 Caracciolo, L., Ravidà, D. C. G., Chew, D., Janßen, M., Lünsdorf, N. K., Heins, W. A., Stephan, T., and Stollhofen, H.:
1298 Reconstructing environmental signals across the Permian-Triassic boundary in the SE Germanic Basin: A Quantitative
1299 Provenance Analysis (QPA) approach, *Glob. Planet. Change*, 206, 103631, <https://doi.org/10.1016/j.gloplacha.2021.103631>,
1300 2021.
- 1301 Carrapa, B.: Resolving tectonic problems by dating detrital minerals, *Geology*, 38, 191–192,
1302 <https://doi.org/10.1130/focus022010.1>, 2010.

- 1303 Cave, B. J., Stepanov, A. S., Craw, D., Large, R. R., Halpin, J. A., and Thompson, J.: RELEASE OF TRACE ELEMENTS
 1304 THROUGH THE SUB-GREENSCHIST FACIES BREAKDOWN OF DETRITAL RUTILE TO METAMORPHIC
 1305 TITANITE IN THE OTAGO SCHIST, NEW ZEALAND, *Can. Mineral.*, 53, 379–400,
 1306 <https://doi.org/10.3749/canmin.1400097>, 2015.
- 1307 Cherniak, D. J.: Pb diffusion in rutile, *Contrib. Mineral. Petrol.*, 139, 198–207, <https://doi.org/10.1007/PL00007671>, 2000.
- 1308 Cherniak, D. J., Manchester, J., and Watson, E. B.: Zr and Hf diffusion in rutile, *Earth Planet. Sci. Lett.*, 261, 267–279,
 1309 <https://doi.org/10.1016/j.epsl.2007.06.027>, 2007.
- 1310 Chew, D., O’Sullivan, G., Caracciolo, L., Mark, C., and Tyrrell, S.: Sourcing the sand: Accessory mineral fertility, analytical
 1311 and other biases in detrital U–Pb provenance analysis, *Earth-Sci. Rev.*, 202, 103093,
 1312 <https://doi.org/10.1016/j.earscirev.2020.103093>, 2020.
- 1313 Chew, D. M., Sylvester, P. J., and Tubrett, M. N.: U–Pb and Th–Pb dating of apatite by LA-ICPMS, *Chem. Geol.*, 280, 200–
 1314 216, <https://doi.org/10.1016/j.chemgeo.2010.11.010>, 2011.
- 1315 Chew, D. M., Petrus, J. A., and Kamber, B. S.: U–Pb LA-ICPMS dating using accessory mineral standards with variable
 1316 common Pb, *Chem. Geol.*, 363, 185–199, <https://doi.org/10.1016/j.chemgeo.2013.11.006>, 2014.
- 1317 Clark, D. J., Hensen, B. J., and Kinny, P. D.: Geochronological constraints for a two-stage history of the Albany–Fraser
 1318 Orogen, Western Australia, *Precambrian Res.*, 102, 155–183, [https://doi.org/10.1016/S0301-9268\(00\)00063-2](https://doi.org/10.1016/S0301-9268(00)00063-2), 2000.
- 1319 Clift, P. D., Hodges, K. V., Heslop, D., Hannigan, R., Van Long, H., and Calves, G.: Correlation of Himalayan exhumation
 1320 rates and Asian monsoon intensity, *Nat. Geosci.*, 1, 875–880, <https://doi.org/10.1038/ngeo351>, 2008.
- 1321 Clift, P. D., Mark, C., Alizai, A., Khan, H., and Jan, M. Q.: Detrital U–Pb rutile and zircon data show Indus River sediment
 1322 dominantly eroded from East Karakoram, not Nanga Parbat, *Earth Planet. Sci. Lett.*, 600, 117873,
 1323 <https://doi.org/10.1016/j.epsl.2022.117873>, 2022.
- 1324 Compston, W., Williams, I. S., and Meyer, C.: U–Pb geochronology of zircons from lunar breccia 73217 using a sensitive high
 1325 mass-resolution ion microprobe, *J. Geophys. Res. Solid Earth*, 89, B525–B534, <https://doi.org/10.1029/JB089iS02p0B525>,
 1326 1984.
- 1327 Crameri, F., Shephard, G. E., and Heron, P. J.: The misuse of colour in science communication, *Nat. Commun.*, 11, 5444,
 1328 <https://doi.org/10.1038/s41467-020-19160-7>, 2020.
- 1329 Davis, W. J., Canil, D., MacKenzie, J. M., and Carbone, G. B.: Petrology and U–Pb geochronology of lower crustal xenoliths
 1330 and the development of a craton, Slave Province, Canada, *Lithos*, 71, 541–573, [https://doi.org/10.1016/S0024-4937\(03\)00130-0](https://doi.org/10.1016/S0024-4937(03)00130-0),
 1331 2003.
- 1332 Dickinson, W. R. and Suczek, C. A.: Plate Tectonics and Sandstone Compositions, *AAPG Bull.*, 63, 2164–2182, 1979.
- 1333 Dodson, M. H.: Closure Temperature in Cooling Geochronological and Petrological Systems, *Contrib. Mineral. Petrol.*, 40,
 1334 259–274, 1973.
- 1335 Ershova, V., Prokopiev, A., and Stockli, D.: Provenance of Detrital Rutiles from the Triassic–Jurassic Sandstones in Franz
 1336 Josef Land (Barents Sea Region, Russian High Arctic): U–Pb Ages and Trace Element Geochemistry, *Geosciences*, 14, 41,
 1337 <https://doi.org/10.3390/geosciences14020041>, 2024.

- 1338 Ersoy, E. Y., Akal, C., Genç, Ş. C., Candan, O., Palmer, M. R., Prelević, D., Uysal, İ., and Mertz-Kraus, R.: U-Pb zircon
1339 geochronology of the Paleogene – Neogene volcanism in the NW Anatolia: Its implications for the Late Mesozoic-Cenozoic
1340 geodynamic evolution of the Aegean, *Tectonophysics*, 717, 284–301, <https://doi.org/10.1016/j.tecto.2017.08.016>, 2017.
- 1341 Ersoy, E. Y., Akal, C., Palmer, M. R., and Mertz-Kraus, R.: U-Pb dating of arc to post-collisional magmatic events in
1342 northwestern Anatolia: The Eocene Granitoids in NW Anatolia revisited, *J. Asian Earth Sci.* X, 9, 100148,
1343 <https://doi.org/10.1016/j.jaesx.2023.100148>, 2023.
- 1344 Ewing, T. A.: Hf isotope analysis and U-Pb geochronology of rutile : technique development and application to a lower crustal
1345 section (Ivrea-Verbanò Zone, Italy), <https://doi.org/10.25911/5d74e68841e8d>, 2011.
- 1346 Ewing, T. A., Rubatto, D., Beltrando, M., and Hermann, J.: Constraints on the thermal evolution of the Adriatic margin during
1347 Jurassic continental break-up: U–Pb dating of rutile from the Ivrea–Verbanò Zone, Italy, *Contrib. Mineral. Petrol.*, 169, 44,
1348 <https://doi.org/10.1007/s00410-015-1135-6>, 2015.
- 1349 Faure, G.: *Principles of Isotope Geology*, 2nd Edition., Wiley & Sons, Inc., 608 pp., 1986.
- 1350 Federici, I., CAVAZZA, W., OKAY, A. I., BEYSSAC, O., ZATTIN, M., CORRADO, S., and DELLISANTI, F.: Thermal
1351 Evolution of the Permo–Triassic Karakaya Subduction-accretion Complex between the Biga Peninsula and the Tokat Massif
1352 (Anatolia), *Turk. J. Earth Sci.*, 19, 409–429, <https://doi.org/10.3906/yer-0910-39>, 2010.
- 1353 Ferry, J. M. and Watson, E. B.: New thermodynamic models and revised calibrations for the Ti-in-zircon and Zr-in-rutile
1354 thermometers, *Contrib. Mineral. Petrol.*, 154, 429–437, <https://doi.org/10.1007/s00410-007-0201-0>, 2007.
- 1355 Flowers, R. M., Bowring, S. A., Tulloch, A. J., and Klepeis, K. A.: Tempo of burial and exhumation within the deep roots of
1356 a magmatic arc, Fiordland, New Zealand, *Geology*, 33, 17–20, <https://doi.org/10.1130/G21010.1>, 2005.
- 1357 Foley, S. F., Barth, M. G., and Jenner, G. A.: Rutile/melt partition coefficients for trace elements and an assessment of the
1358 influence of rutile on the trace element characteristics of subduction zone magmas, *Geochim. Cosmochim. Acta*, 64, 933–938,
1359 [https://doi.org/10.1016/S0016-7037\(99\)00355-5](https://doi.org/10.1016/S0016-7037(99)00355-5), 2000.
- 1360 Garzanti, E. and Andò, S.: Heavy Mineral Concentration in Modern Sands: Implications for Provenance Interpretation, in:
1361 *Developments in Sedimentology*, vol. 58, edited by: Mange, M. A. and Wright, D. T., Elsevier, 517–545,
1362 [https://doi.org/10.1016/S0070-4571\(07\)58020-9](https://doi.org/10.1016/S0070-4571(07)58020-9), 2007.
- 1363 Garzanti, E., Doglioni, C., Vezzoli, G., and Ando, S.: Orogenic belts and orogenic sediment provenance, *J. Geol.*, 115, 315–
1364 334, 2007.
- 1365 Gaschnig, R. M.: Benefits of a Multiproxy Approach to Detrital Mineral Provenance Analysis: An Example from the
1366 Merrimack River, New England, USA, *Geochem. Geophys. Geosystems*, 20, 1557–1573,
1367 <https://doi.org/10.1029/2018GC008005>, 2019.
- 1368 Gazzi, P.: On the Heavy Mineral Zones in the Geosyncline Series. *Recent Studies in the Northern Apennines, Italy*, *J.*
1369 *Sediment. Petrol.*, 35, 109–115, <https://doi.org/10.1306/74D71203-2B21-11D7-8648000102C1865D>, 1965.
- 1370 Gehrels, G.: Detrital Zircon U-Pb Geochronology: Current Methods and New Opportunities, in: *Tectonics of Sedimentary*
1371 *Basins*, John Wiley & Sons, Ltd, 45–62, <https://doi.org/10.1002/9781444347166.ch2>, 2011.
- 1372 Gehrels, G.: Detrital Zircon U-Pb Geochronology Applied to Tectonics, *Annu. Rev. Earth Planet. Sci.*, 42, 127–149,
1373 <https://doi.org/10.1146/annurev-earth-050212-124012>, 2014.

- 1374 Gehrels, G. E., Valencia, V. A., and Ruiz, J.: Enhanced precision, accuracy, efficiency, and spatial resolution of U-Pb ages by
 1375 laser ablation–multicollector–inductively coupled plasma–mass spectrometry, *Geochem. Geophys. Geosystems*, 9, Q03017,
 1376 <https://doi.org/10.1029/2007GC001805>, 2008.
- 1377 Gönçüoğlu, M. C., Turhan, N., Şentürk, K., Özcan, A., Uysal, Ş., and Yaliniz, M. K.: A Geotraverse Across Northwestern
 1378 Turkey: Tectonic Units of the Central Sakarya Region and their Tectonic Evolution, *Geol. Soc. Lond. Spec. Publ.*, 173, 139–
 1379 161, <https://doi.org/10.1144/GSL.SP.2000.173.01.06>, 2000.
- 1380 Govin, G., Najman, Y., Copley, A., Millar, I., van der Beek, P., Huyghe, P., Grujic, D., and Davenport, J.: Timing and
 1381 mechanism of the rise of the Shillong Plateau in the Himalayan foreland, *Geology*, 46, 279–282,
 1382 <https://doi.org/10.1130/G39864.1>, 2018.
- 1383 Guo, R., Hu, X., Garzanti, E., Lai, W., Yan, B., and Mark, C.: How faithfully do the geochronological and geochemical
 1384 signatures of detrital zircon, titanite, rutile and monazite record magmatic and metamorphic events? A case study from the
 1385 Himalaya and Tibet, *Earth-Sci. Rev.*, 201, 103082, <https://doi.org/10.1016/j.earscirev.2020.103082>, 2020.
- 1386 Harris, N. B. W., Kelley, S., and Okay, A. I.: Post-collisional magmatism and tectonics in northwest Anatolia, *Contrib. Mineral.
 1387 Petrol.*, 117, 241–252, 1994.
- 1388 Hart, E., Storey, C., Bruand, E., Schertl, H.-P., and Alexander, B. D.: Mineral inclusions in rutile: A novel recorder of HP-
 1389 UHP metamorphism, *Earth Planet. Sci. Lett.*, 446, 137–148, <https://doi.org/10.1016/j.epsl.2016.04.035>, 2016.
- 1390 Hart, E., Storey, C., Harley, S. L., and Fowler, M.: A window into the lower crust: Trace element systematics and the
 1391 occurrence of inclusions/intergrowths in granulite-facies rutile, *Gondwana Res.*, 59, 76–86,
 1392 <https://doi.org/10.1016/j.gr.2018.02.021>, 2018.
- 1393 Hietpas, J., Samson, S., Moecher, D., and Schmitt, A. K.: Recovering tectonic events from the sedimentary record: Detrital
 1394 monazite plays in high fidelity, *Geology*, 38, 167–170, <https://doi.org/10.1130/G30265.1>, 2010.
- 1395 Hietpas, J., Samson, S., Moecher, D., and Chakraborty, S.: Enhancing tectonic and provenance information from detrital zircon
 1396 studies: assessing terrane-scale sampling and grain-scale characterization, *J. Geol. Soc.*, 168, 309–318,
 1397 <https://doi.org/10.1144/0016-76492009-163>, 2011.
- 1398 Hubert, J. F.: Analysis of heavy-mineral assemblages, in: *Procedures in sedimentary petrology*, edited by: Carver, R. E., New
 1399 York: Wiley-Interscience, 453–478, 1971.
- 1400 Itaya, T.: K–Ar phengite geochronology of HP–UHP metamorphic rocks –An in–depth review–, *J. Mineral. Petrol. Sci.*, 115,
 1401 44–58, <https://doi.org/10.2465/jmps.190123>, 2020.
- 1402 Jochum, K. P., Wilson, S. A., Abouchami, W., Amini, M., Chmeleff, J., Eisenhauer, A., Hegner, E., Iaccheri, L. M., Kieffer,
 1403 B., Krause, J., McDonough, W. F., Mertz-Kraus, R., Raczek, I., Rudnick, R. L., Scholz, D., Steinhofel, G., Stoll, B., Stracke,
 1404 A., Tonarini, S., Weis, D., Weis, U., and Woodhead, J. D.: GSD-1G and MPI-DING Reference Glasses for In Situ and Bulk
 1405 Isotopic Determination, *Geostand. Geoanalytical Res.*, 35, 193–226, <https://doi.org/10.1111/j.1751-908X.2010.00114.x>, 2011.
- 1406 Kasapoğlu, B., Ersoy, Y. E., Uysal, İ., Palmer, M. R., Zack, T., Koralay, E. O., and Karlsson, A.: The petrology of Paleogene
 1407 volcanism in the Central Sakarya, Nallıhan Region: Implications for the initiation and evolution of post-collisional, slab break-
 1408 off-related magmatic activity, *Lithos*, 246–247, 81–98, <https://doi.org/10.1016/j.lithos.2015.12.024>, 2016.

- 1409 Kellett, D. A., Weller, O. M., Zagorevski, A., and Regis, D.: A petrochronological approach for the detrital record: Tracking
1410 mm-sized eclogite clasts in the northern Canadian Cordillera, *Earth Planet. Sci. Lett.*, 494, 23–31,
1411 <https://doi.org/10.1016/j.epsl.2018.04.036>, 2018.
- 1412 Keskin, M. and Tüysüz, O.: Stratigraphy, petrogenesis and geodynamic setting of Late Cretaceous volcanism on the SW
1413 margin of the Black Sea, Turkey, *Geol. Soc. Lond. Spec. Publ.*, 464, 95–130, <https://doi.org/10.1144/SP464.5>, 2018.
- 1414 Klemme, S., Blundy, J. D., and Wood, B. J.: Experimental constraints on major and trace element partitioning during partial
1415 melting of eclogite, *Geochim. Cosmochim. Acta*, 66, 3109–3123, [https://doi.org/10.1016/S0016-7037\(02\)00859-1](https://doi.org/10.1016/S0016-7037(02)00859-1), 2002.
- 1416 Kohn, M. J.: A refined zirconium-in-rutile thermometer, *Am. Mineral.*, 105, 963–971, <https://doi.org/10.2138/am-2020-7091>,
1417 2020.
- 1418 Kohn, M. J. and Kelly, N. M.: Petrology and Geochronology of Metamorphic Zircon, in: *Geophysical Monograph Series*,
1419 edited by: Moser, D. E., Corfu, F., Darling, J. R., Reddy, S. M., and Tait, K., John Wiley & Sons, Inc., Hoboken, NJ, USA,
1420 35–61, <https://doi.org/10.1002/9781119227250.ch2>, 2017.
- 1421 Kooijman, E., Mezger, K., and Berndt, J.: Constraints on the U–Pb systematics of metamorphic rutile from in situ LA-ICP-
1422 MS analysis, *Earth Planet. Sci. Lett.*, 293, 321–330, <https://doi.org/10.1016/j.epsl.2010.02.047>, 2010.
- 1423 Kooijman, E., Smit, M. A., Mezger, K., and Berndt, J.: Trace element systematics in granulite facies rutile: implications for
1424 Zr geothermometry and provenance studies, *J. Metamorph. Geol.*, 30, 397–412, <https://doi.org/10.1111/j.1525-1314.2012.00972.x>, 2012.
- 1426 Kylander-Clark, A. R. C.: Slow subduction and exhumation of a thick ultrahigh -pressure terrane: Western Gneiss Region,
1427 Norway, Ph.D., University of California, Santa Barbara, United States -- California, 121 pp., 2008.
- 1428 Kylander-Clark, A. R. C., Hacker, B. R., and Mattinson, J. M.: Slow exhumation of UHP terranes: Titanite and rutile ages of
1429 the Western Gneiss Region, Norway, *Earth Planet. Sci. Lett.*, 272, 531–540, <https://doi.org/10.1016/j.epsl.2008.05.019>, 2008.
- 1430 Lippert, P. G.: Detrital U-Pb geochronology provenance analyses: case studies in the Greater Green River Basin, Wyoming,
1431 and the Book Cliffs, Utah, Thesis, University of Kansas, 2014.
- 1432 Ludwig, K. R.: On the Treatment of Concordant Uranium-Lead Ages, *Geochim. Cosmochim. Acta*, 62, 665–676,
1433 [https://doi.org/10.1016/S0016-7037\(98\)00059-3](https://doi.org/10.1016/S0016-7037(98)00059-3), 1998.
- 1434 Luvizotto, G. L. and Zack, T.: Nb and Zr behavior in rutile during high-grade metamorphism and retrogression: An example
1435 from the Ivrea–Verbano Zone, *Chem. Geol.*, 261, 303–317, <https://doi.org/10.1016/j.chemgeo.2008.07.023>, 2009.
- 1436 Luvizotto, G. L., Zack, T., Meyer, H. P., Ludwig, T., Triebold, S., Kronz, A., Münker, C., Stockli, D. F., Prowatke, S., Klemme,
1437 S., Jacob, D. E., and von Eynatten, H.: Rutile crystals as potential trace element and isotope mineral standards for
1438 microanalysis, *Chem. Geol.*, 261, 346–369, <https://doi.org/10.1016/j.chemgeo.2008.04.012>, 2009.
- 1439 Malusà, M. G., Carter, A., Limoncelli, M., Villa, I. M., and Garzanti, E.: Bias in detrital zircon geochronology and
1440 thermochronometry, *Chem. Geol.*, 359, 90–107, <https://doi.org/10.1016/j.chemgeo.2013.09.016>, 2013.
- 1441 Mark, C., Cogné, N., and Chew, D.: Tracking exhumation and drainage divide migration of the Western Alps: A test of the
1442 apatite U-Pb thermochronometer as a detrital provenance tool, *GSA Bull.*, 128, 1439–1460, <https://doi.org/10.1130/B31351.1>,
1443 2016.

- 1444 McLean, N. M., Bowring, J. F., and Bowring, S. A.: An algorithm for U-Pb isotope dilution data reduction and uncertainty
1445 propagation, *Geochem. Geophys. Geosystems*, 12, <https://doi.org/10.1029/2010GC003478>, 2011.
- 1446 Meinhold, G.: Rutile and its applications in earth sciences, *Earth-Sci. Rev.*, 102, 1–28,
1447 <https://doi.org/10.1016/j.earscirev.2010.06.001>, 2010.
- 1448 Meinhold, G., Anders, B., Kostopoulos, D., and Reischmann, T.: Rutile chemistry and thermometry as provenance indicator:
1449 An example from Chios Island, Greece, *Sediment. Geol.*, 203, 98–111, <https://doi.org/10.1016/j.sedgeo.2007.11.004>, 2008.
- 1450 Meinhold, G., MORTON, A. C., FANNING, C. M., and WHITHAM, A. G.: U–Pb SHRIMP ages of detrital granulite-facies
1451 rutiles: further constraints on provenance of Jurassic sandstones on the Norwegian margin, *Geol. Mag.*, 148, 473–480,
1452 <https://doi.org/10.1017/S0016756810000877>, 2010.
- 1453 Mezger, K., Hanson, G. N., and Bohlen, S. R.: High-precision UPb ages of metamorphic rutile: application to the cooling
1454 history of high-grade terranes, *Earth Planet. Sci. Lett.*, 96, 106–118, [https://doi.org/10.1016/0012-821X\(89\)90126-X](https://doi.org/10.1016/0012-821X(89)90126-X), 1989.
- 1455 Moecher, D., Hietpas, J., Samson, S., and Chakraborty, S.: Insights into southern Appalachian tectonics from ages of detrital
1456 monazite and zircon in modern alluvium, *Geosphere*, 7, 494–512, <https://doi.org/10.1130/GES00615.1>, 2011.
- 1457 Möller, A., Mezger, K., and Schenk, V.: U–Pb dating of metamorphic minerals: Pan-African metamorphism and prolonged
1458 slow cooling of high pressure granulites in Tanzania, East Africa, *Precambrian Res.*, 104, 123–146,
1459 [https://doi.org/10.1016/S0301-9268\(00\)00086-3](https://doi.org/10.1016/S0301-9268(00)00086-3), 2000.
- 1460 Morton, A. and Yaxley, G.: Detrital apatite geochemistry and its application in provenance studies, *Geol. Soc. Am. Spec. Pap.*,
1461 420, 319–344, [https://doi.org/10.1130/2006.2420\(19\)](https://doi.org/10.1130/2006.2420(19)), 2007.
- 1462 Morton, A. C.: Heavy minerals in provenance studies, in: *Provenance of Arenites*, edited by: Zuffa, G. G., Reidel, Dordrecht,
1463 249–277, 1985.
- 1464 Mueller, M., Licht, A., Möller, A., Condit, C., Fosdick, J. C., Ocakoğlu, F., and Campbell, C.: Supplemental data for:
1465 Navigating the complexity of detrital rutile provenance: Methodological insights from the Neotethys Orogen in Anatolia,
1466 <https://doi.org/10.17605/OSF.IO/A4YE5>, 2023.
- 1467 Mueller, M. A.: *mmueller13/Detrital-UPb-and-TE: v0.2*, , <https://doi.org/10.5281/zenodo.10636728>, 2024.
- 1468 Mueller, M. A., Licht, A., Campbell, C., Ocakoğlu, F., Taylor, M. H., Burch, L., Ugrai, T., Kaya, M., Kurtoğlu, B., Coster, P.
1469 M. C., Métais, G., and Beard, K. C.: Collision Chronology Along the İzmir-Ankara-Erzincan Suture Zone: Insights From the
1470 Sarıcakaya Basin, Western Anatolia, *Tectonics*, 38, 3652–3674, <https://doi.org/10.1029/2019TC005683>, 2019.
- 1471 Mueller, M. A., Licht, A., Campbell, C., Ocakoğlu, F., Akşit, G. G., Métais, G., Coster, P. M. C., Beard, K. C., and Taylor,
1472 M. H.: Sedimentary Provenance From the Evolving Forearc-to-Foreland Central Sakarya Basin, Western Anatolia Reveals
1473 Multi-Phase Intercontinental Collision, *Geochem. Geophys. Geosystems*, 23, e2021GC010232,
1474 <https://doi.org/10.1029/2021GC010232>, 2022.
- 1475 Nemchin, A. A. and Cawood, P. A.: Discordance of the U–Pb system in detrital zircons: Implication for provenance studies
1476 of sedimentary rocks, *Sediment. Geol.*, 182, 143–162, <https://doi.org/10.1016/j.sedgeo.2005.07.011>, 2005.
- 1477 Ocakoğlu, F., Hakyemez, A., Açıkalın, S., Özkan Altıner, S., Büyükmeriç, Y., Licht, A., Demircan, H., Şafak, Ü., Yıldız, A.,
1478 Yılmaz, İ. Ö., Wagreich, M., and Campbell, C.: Chronology of subduction and collision along the İzmir-Ankara suture in

- 1479 Western Anatolia: records from the Central Sakarya Basin, *Int. Geol. Rev.*, 1–26,
1480 <https://doi.org/10.1080/00206814.2018.1507009>, 2018.
- 1481 Odlum, M. L., Stockli, D. F., Capaldi, T. N., Thomson, K. D., Clark, J., Puigdefàbregas, C., and Fildani, A.: Tectonic and
1482 sediment provenance evolution of the South Eastern Pyrenean foreland basins during rift margin inversion and orogenic uplift,
1483 *Tectonophysics*, 765, 226–248, <https://doi.org/10.1016/j.tecto.2019.05.008>, 2019.
- 1484 Okay, A., Satir, M., and Siebel, W.: Pre-Alpide Palaeozoic and Mesozoic Orogenic Events in the Eastern Mediterranean
1485 Region, *Geol. Soc. Lond. Mem.*, 32, 389–405, <https://doi.org/10.1144/GSL.MEM.2006.032.01.23>, 2006.
- 1486 Okay, A. I. and Gönçüoğlu, M. C.: The Karakaya Complex: A Review of Data and Concepts, *Turk. J. Earth Sci.*, 13, 77–95,
1487 2004.
- 1488 Okay, A. I. and Kelley, S. P.: Tectonic setting, petrology and geochronology of jadeite + glaucophane and chloritoid +
1489 glaucophane schists from north-west Turkey, *J. Metamorph. Geol.*, 12, 455–466, <https://doi.org/10.1111/j.1525-1314.1994.tb00035.x>, 1994.
- 1491 Okay, A. I. and Kylander-Clark, A. R. C.: No sediment transport across the Tethys ocean during the latest Cretaceous: detrital
1492 zircon record from the Pontides and the Anatolide–Tauride Block, *Int. J. Earth Sci.*, <https://doi.org/10.1007/s00531-022-02275-1>, 2022.
- 1494 Okay, A. I., Monod, O., and Monié, P.: Triassic blueschists and eclogites from northwest Turkey: vestiges of the Paleo-Tethyan
1495 subduction, *Lithos*, 64, 155–178, [https://doi.org/10.1016/S0024-4937\(02\)00200-1](https://doi.org/10.1016/S0024-4937(02)00200-1), 2002.
- 1496 Okay, A. I., Altiner, D., and Kiliç, A. M.: Triassic limestone, turbidites and serpentinite—the Cimmeride orogeny in the Central
1497 Pontides, *Geol. Mag.*, 152, 460–479, <https://doi.org/10.1017/S0016756814000429>, 2015.
- 1498 Okay, A. I., Sunal, G., Sherlock, S., Kylander-Clark, A. R. C., and Özcan, E.: İzmir-Ankara Suture as a Triassic to Cretaceous
1499 Plate Boundary—Data From Central Anatolia, *Tectonics*, 39, e2019TC005849, <https://doi.org/10.1029/2019TC005849>, 2020.
- 1500 Okay, N., Zack, T., Okay, A. I., and Barth, M.: Sinistral transport along the Trans-European Suture Zone: detrital zircon–rutile
1501 geochronology and sandstone petrography from the Carboniferous flysch of the Pontides, *Geol. Mag.*, 148, 380–403,
1502 <https://doi.org/10.1017/S0016756810000804>, 2011.
- 1503 O’Sullivan, G., Chew, D., Kenny, G., Henrichs, I., and Mulligan, D.: The trace element composition of apatite and its
1504 application to detrital provenance studies, *Earth-Sci. Rev.*, 201, 103044, <https://doi.org/10.1016/j.earscirev.2019.103044>,
1505 2020.
- 1506 O’Sullivan, G. J., Chew, D. M., and Samson, S. D.: Detecting magma-poor orogens in the detrital record, *Geology*, 44, 871–
1507 874, <https://doi.org/10.1130/G38245.1>, 2016.
- 1508 Paterson, S. R. and Ducea, M. N.: Arc Magmatic Tempos: Gathering the Evidence, *Elements*, 11, 91–98,
1509 <https://doi.org/10.2113/gselements.11.2.91>, 2015.
- 1510 Paton, C., Hellstrom, J., Paul, B., Woodhead, J., and Hergt, J.: Iolite: Freeware for the visualisation and processing of mass
1511 spectrometric data, *J. Anal. At. Spectrom.*, 26, 2508, <https://doi.org/10.1039/c1ja10172b>, 2011.
- 1512 Pawlowsky-Glahn, V., Egozcue, J. J., and Tolosana-Delgado, R.: *Modeling and Analysis of Compositional Data*, John Wiley
1513 & Sons, Incorporated, Newark, UNITED STATES, 2015.

- 1514 Pereira, I. and Storey, C. D.: Detrital rutile: Records of the deep crust, ores and fluids, *Lithos*, 107010,
1515 <https://doi.org/10.1016/j.lithos.2022.107010>, 2023.
- 1516 Pereira, I., Storey, C. D., Strachan, R. A., Bento dos Santos, T., and Darling, J. R.: Detrital rutile ages can deduce the tectonic
1517 setting of sedimentary basins, *Earth Planet. Sci. Lett.*, 537, 116193, <https://doi.org/10.1016/j.epsl.2020.116193>, 2020.
- 1518 Pereira, I., Storey, C. D., Darling, J. R., Moreira, H., Strachan, R. A., and Cawood, P. A.: Detrital rutile tracks the first
1519 appearance of subduction zone low T/P paired metamorphism in the Palaeoproterozoic, *Earth Planet. Sci. Lett.*, 570, 117069,
1520 <https://doi.org/10.1016/j.epsl.2021.117069>, 2021.
- 1521 Pickett, E. A. and Robertson, A. H. F.: Formation of the Late Palaeozoic–Early Mesozoic Karakaya Complex and related
1522 ophiolites in NW Turkey by Palaeotethyan subduction–accretion, *J. Geol. Soc.*, 153, 995–1009,
1523 <https://doi.org/10.1144/gsjgs.153.6.0995>, 1996.
- 1524 Plavsa, D., Reddy, S. M., Agangi, A., Clark, C., Kylander-Clark, A., and Tiddy, C. J.: Microstructural, trace element and
1525 geochronological characterization of TiO₂ polymorphs and implications for mineral exploration, *Chem. Geol.*, 476, 130–149,
1526 <https://doi.org/10.1016/j.chemgeo.2017.11.011>, 2018.
- 1527 Poulaki, E. M., Stockli, D. F., and Shuck, B. D.: Pre-Subduction Architecture Controls Coherent Underplating During
1528 Subduction and Exhumation (Nevado-Filábride Complex, Southern Spain), *Geochem. Geophys. Geosystems*, 24,
1529 e2022GC010802, <https://doi.org/10.1029/2022GC010802>, 2023.
- 1530 Pourteau, A., Oberhänsli, R., Candan, O., Barrier, E., and Vrielynck, B.: Neotethyan closure history of western Anatolia: a
1531 geodynamic discussion, *Int. J. Earth Sci.*, 105, 203–224, <https://doi.org/10.1007/s00531-015-1226-7>, 2016.
- 1532 Rösel, D., Boger, S. D., Möller, A., Gaitzsch, B., Barth, M., Oalmann, J., and Zack, T.: Indo-Antarctic derived detritus on the
1533 northern margin of Gondwana: evidence for continental-scale sediment transport, *Terra Nova*, 26, 64–71,
1534 <https://doi.org/10.1111/ter.12070>, 2014.
- 1535 Rösel, D., Zack, T., and Möller, A.: Interpretation and significance of combined trace element and U–Pb isotopic data of
1536 detrital rutile: a case study from late Ordovician sedimentary rocks of Saxo-Thuringia, Germany, *Int. J. Earth Sci.*, 108, 1–25,
1537 <https://doi.org/10.1007/s00531-018-1643-5>, 2019.
- 1538 Rudnick, R., Barth, M., Horn, I., and McDonough, W. F.: Rutile-Bearing Refractory Eclogites: Missing Link Between
1539 Continents and Depleted Mantle, *Science*, 287, 278–281, <https://doi.org/10.1126/science.287.5451.278>, 2000.
- 1540 Schärer, U., Krogh, T. E., and Gower, C. F.: Age and evolution of the Grenville Province in eastern Labrador from U–Pb
1541 systematics in accessory minerals, *Contrib. Mineral. Petrol.*, 94, 438–451, <https://doi.org/10.1007/BF00376337>, 1986.
- 1542 Schmitz, M. D. and Bowring, S. A.: Constraints on the thermal evolution of continental lithosphere from U–Pb accessory
1543 mineral thermochronometry of lower crustal xenoliths, southern Africa, *Contrib. Mineral. Petrol.*, 144, 592–618,
1544 <https://doi.org/10.1007/s00410-002-0419-9>, 2003.
- 1545 Schoene, B.: U–Th–Pb Geochronology, in: *Treatise on Geochemistry*, Elsevier, 341–378, <https://doi.org/10.1016/B978-0-08-095975-7.00310-7>, 2014.
- 1547 Şengör, A. M. C. and Yılmaz, Y.: Tethyan evolution of turkey: a plate tectonic approach, *Tectonophysics*, 75, 181–241, 1981.

- 1548 Şengör, A. M. C., Yılmaz, Y., and Sungurlu, O.: Tectonics of the Mediterranean Cimmerides: nature and evolution of the
 1549 western termination of Palaeo-Tethys, *Geol. Soc. Lond. Spec. Publ.*, 17, 77–112,
 1550 <https://doi.org/10.1144/GSL.SP.1984.017.01.04>, 1984.
- 1551 Şengün, F., Zack, T., and Dunkl, I.: Provenance of detrital rutiles from the Jurassic sandstones in the Central Sakarya Zone,
 1552 NW Turkey: U-Pb ages and trace element geochemistry, *Geochemistry*, 80, 125667,
 1553 <https://doi.org/10.1016/j.chemer.2020.125667>, 2020.
- 1554 Shaanan, U., Avigad, D., Morag, N., Güngör, T., and Gerdes, A.: Drainage response to Arabia–Eurasia collision: Insights from
 1555 provenance examination of the Cyprian Kythrea flysch (Eastern Mediterranean Basin), *Basin Res.*, n/a,
 1556 <https://doi.org/10.1111/bre.12452>, 2020.
- 1557 Sharman, G. R., Sharman, J. P., and Sylvester, Z.: detritalPy: A Python-based toolset for visualizing and analysing detrital
 1558 geo-thermochronologic data, *Depositional Rec.*, 4, 202–215, <https://doi.org/10.1002/dep2.45>, 2018.
- 1559 Sherlock, S., Kelley, S., Inger, S., Harris, N., and Okay, A.: 40Ar-39Ar and Rb-Sr geochronology of high-pressure
 1560 metamorphism and exhumation history of the Tavsanli Zone, NW Turkey, *Contrib. Mineral. Petrol.*, 137, 46–58,
 1561 <https://doi.org/10.1007/PL00013777>, 1999.
- 1562 Simonetti, A., Heaman, L. M., Hartlaub, R. P., Creaser, R. A., MacHattie, T. G., and Böhm, C.: U–Pb zircon dating by laser
 1563 ablation-MC-ICP-MS using a new multiple ion counting Faraday collector array, *J. Anal. At. Spectrom.*, 20, 677–686,
 1564 <https://doi.org/10.1039/B504465K>, 2005.
- 1565 Smye, A. J. and Stockli, D. F.: Rutile U–Pb age depth profiling: A continuous record of lithospheric thermal evolution, *Earth
 1566 Planet. Sci. Lett.*, 408, 171–182, <https://doi.org/10.1016/j.epsl.2014.10.013>, 2014.
- 1567 Smye, A. J., Marsh, J. H., Vermeesch, P., Garber, J. M., and Stockli, D. F.: Applications and limitations of U-Pb
 1568 thermochronology to middle and lower crustal thermal histories, *Chem. Geol.*, 494, 1–18,
 1569 <https://doi.org/10.1016/j.chemgeo.2018.07.003>, 2018.
- 1570 Spencer, C. J., Kirkland, C. L., and Taylor, R. J. M.: Strategies towards statistically robust interpretations of in situ U–Pb
 1571 zircon geochronology, *Geosci. Front.*, 7, 581–589, <https://doi.org/10.1016/j.gsf.2015.11.006>, 2016.
- 1572 Stacey, J. S. and Kramers, J. D.: Approximation of terrestrial lead isotope evolution by a two-stage model, *Earth Planet. Sci.
 1573 Lett.*, 26, 207–221, [https://doi.org/10.1016/0012-821X\(75\)90088-6](https://doi.org/10.1016/0012-821X(75)90088-6), 1975.
- 1574 Steiger, R. H. and Jäger, E.: Subcommittee on geochronology: Convention on the use of decay constants in geo- and
 1575 cosmochronology, *Earth Planet. Sci. Lett.*, 36, 359–362, [https://doi.org/10.1016/0012-821X\(77\)90060-7](https://doi.org/10.1016/0012-821X(77)90060-7), 1977.
- 1576 Storey, C. D., Jeffries, T. E., and Smith, M.: Common lead-corrected laser ablation ICP–MS U–Pb systematics and
 1577 geochronology of titanite, *Chem. Geol.*, 227, 37–52, <https://doi.org/10.1016/j.chemgeo.2005.09.003>, 2006.
- 1578 Storey, C. D., Smith, M. P., and Jeffries, T. E.: In situ LA-ICP-MS U–Pb dating of metavolcanics of Norrbotten, Sweden:
 1579 Records of extended geological histories in complex titanite grains, *Chem. Geol.*, 240, 163–181,
 1580 <https://doi.org/10.1016/j.chemgeo.2007.02.004>, 2007.
- 1581 Sundell, K. E., George, S. W. M., Carrapa, B., Gehrels, G. E., Ducea, M. N., Saylor, J. E., and Pepper, M.: Crustal Thickening
 1582 of the Northern Central Andean Plateau Inferred From Trace Elements in Zircon, *Geophys. Res. Lett.*, 49, e2021GL096443,
 1583 <https://doi.org/10.1029/2021GL096443>, 2022.

- 1584 Tang, M., Ji, W.-Q., Chu, X., Wu, A., and Chen, C.: Reconstructing crustal thickness evolution from europium anomalies in
1585 detrital zircons, *Geology*, 49, 76–80, <https://doi.org/10.1130/G47745.1>, 2020.
- 1586 Templ, M., Hron, K., and Filzmoser, P.: robCompositions: An R-package for Robust Statistical Analysis of Compositional
1587 Data, in: *Compositional Data Analysis*, John Wiley & Sons, Ltd, 341–355, <https://doi.org/10.1002/9781119976462.ch25>,
1588 2011.
- 1589 Tera, F. and Wasserburg, G. J.: U-Th-Pb systematics in three Apollo 14 basalts and the problem of initial Pb in lunar rocks,
1590 *Earth Planet. Sci. Lett.*, 14, 281–304, [https://doi.org/10.1016/0012-821X\(72\)90128-8](https://doi.org/10.1016/0012-821X(72)90128-8), 1972.
- 1591 Tomkins, H. S., Powell, R., and Ellis, D. J.: The pressure dependence of the zirconium-in-rutile thermometer, *J. Metamorph.*
1592 *Geol.*, 25, 703–713, <https://doi.org/10.1111/j.1525-1314.2007.00724.x>, 2007.
- 1593 Topuz, G., Altherr, R., Schwarz, W. H., Dokuz, A., and Meyer, H.-P.: Variscan amphibolite-facies rocks from the Kurtoğlu
1594 metamorphic complex (Gümüşhane area, Eastern Pontides, Turkey), *Int. J. Earth Sci.*, 96, 861–873,
1595 <https://doi.org/10.1007/s00531-006-0138-y>, 2007.
- 1596 Topuz, G., Candan, O., Okay, A. I., von Quadt, A., Othman, M., Zack, T., and Wang, J.: Silurian anorogenic basic and acidic
1597 magmatism in Northwest Turkey: Implications for the opening of the Paleo-Tethys, *Lithos*, 356–357, 105302,
1598 <https://doi.org/10.1016/j.lithos.2019.105302>, 2020.
- 1599 Triebold, S., von Eynatten, H., Luvizotto, G. L., and Zack, T.: Deducing source rock lithology from detrital rutile geochemistry:
1600 An example from the Erzgebirge, Germany, *Chem. Geol.*, 244, 421–436, <https://doi.org/10.1016/j.chemgeo.2007.06.033>,
1601 2007.
- 1602 Triebold, S., Luvizotto, G. L., Tolosana-Delgado, R., Zack, T., and von Eynatten, H.: Discrimination of TiO₂ polymorphs in
1603 sedimentary and metamorphic rocks, *Contrib. Mineral. Petrol.*, 161, 581–596, <https://doi.org/10.1007/s00410-010-0551-x>,
1604 2011.
- 1605 Triebold, S., von Eynatten, H., and Zack, T.: A recipe for the use of rutile in sedimentary provenance analysis, *Sediment.*
1606 *Geol.*, 282, 268–275, <https://doi.org/10.1016/j.sedgeo.2012.09.008>, 2012.
- 1607 Ustaömer, P., Ustaömer, T., and Robertson, Alastair. H. F.: Ion Probe U-Pb Dating of the Central Sakarya Basement: A peri-
1608 Gondwana Terrane Intruded by Late Lower Carboniferous Subduction/Collision-related Granitic Rocks, *Turk. J. Earth Sci.*,
1609 21, 905–932, <https://doi.org/10.3906/yer-1103-1>, 2012.
- 1610 Ustaömer, T., Robertson, A. H. F., Ustaömer, P. A., Gerdes, A., and Peytcheva, I.: Constraints on Variscan and Cimmerian
1611 magmatism and metamorphism in the Pontides (Yusufeli–Artvin area), NE Turkey from U–Pb dating and granite
1612 geochemistry, *Geol. Soc. Lond. Spec. Publ.*, 372, 49–74, <https://doi.org/10.1144/SP372.13>, 2013.
- 1613 Ustaömer, T., Ustaömer, P., Robertson, A. H. F., and Gerdes, A.: Implications of U–Pb and Lu–Hf isotopic analysis of detrital
1614 zircons for the depositional age, provenance and tectonic setting of the Permian–Triassic Palaeotethyan Karakaya Complex,
1615 NW Turkey, *Int. J. Earth Sci.*, 105, 7–38, <https://doi.org/10.1007/s00531-015-1225-8>, 2016.
- 1616 Vermeesch, P.: Unifying the U–Pb and Th–Pb methods: joint isochron regression and common Pb correction, *Geochronology*,
1617 2, 119–131, <https://doi.org/10.5194/gchron-2-119-2020>, 2020.
- 1618 Vermeesch, P.: On the treatment of discordant detrital zircon U–Pb data, *Geochronology*, 3, 247–257,
1619 <https://doi.org/10.5194/gchron-3-247-2021>, 2021.

- 1620 Vry, J. K. and Baker, J. A.: LA-MC-ICPMS Pb–Pb dating of rutile from slowly cooled granulites: Confirmation of the high
1621 closure temperature for Pb diffusion in rutile, *Geochim. Cosmochim. Acta*, 70, 1807–1820,
1622 <https://doi.org/10.1016/j.gca.2005.12.006>, 2006.
- 1623 Watson, E. B., Wark, D. A., and Thomas, J. B.: Crystallization thermometers for zircon and rutile, *Contrib. Mineral. Petrol.*,
1624 151, 413, <https://doi.org/10.1007/s00410-006-0068-5>, 2006.
- 1625 Williams, I. S.: U-Th-Pb Geochronology by Ion Microprobe, in: *Applications of Microanalytical Techniques to Understanding*
1626 *Mineralizing Processes*, Society of Economic Geologists, 1–35, <https://doi.org/10.5382/Rev.07.01>, 1997.
- 1627 Xiong, X. L., Adam, J., and Green, T. H.: Rutile stability and rutile/melt HFSE partitioning during partial melting of hydrous
1628 basalt: Implications for TTG genesis, *Chem. Geol.*, 218, 339–359, <https://doi.org/10.1016/j.chemgeo.2005.01.014>, 2005.
- 1629 Yildiz, A., Kibici, Y., Bağci, M., Dumlupinar, İ., Kocabaş, C., and Aritan, A. E.: Petrogenesis of the post-collisional Eocene
1630 volcanic rocks from the Central Sakarya Zone (Northwestern Anatolia, Turkey): Implications for source characteristics,
1631 magma evolution, and tectonic setting, *Arab. J. Geosci.*, 8, 11239–11260, <https://doi.org/10.1007/s12517-015-1991-4>, 2015.
- 1632 Zack, T. and Kooijman, E.: Petrochronology and Geochronology of Rutile, *Rev. Mineral. Geochem.*, 83, 443–467, 2017.
- 1633 Zack, T., von Eynatten, H., and Kronz, A.: Rutile geochemistry and its potential use in quantitative provenance studies,
1634 *Sediment. Geol.*, 171, 37–58, <https://doi.org/10.1016/j.sedgeo.2004.05.009>, 2004a.
- 1635 Zack, T., Moraes, R., and Kronz, A.: Temperature dependence of Zr in rutile: empirical calibration of a rutile thermometer,
1636 *Contrib. Mineral. Petrol.*, 148, 471–488, <https://doi.org/10.1007/s00410-004-0617-8>, 2004b.
- 1637 Zack, T., Stockli, D. F., Luvizotto, G. L., Barth, M. G., Belousova, E., Wolfe, M. R., and Hinton, R. W.: In situ U–Pb rutile
1638 dating by LA-ICP-MS: 208Pb correction and prospects for geological applications, *Contrib. Mineral. Petrol.*, 162, 515–530,
1639 <https://doi.org/10.1007/s00410-011-0609-4>, 2011.
- 1640 Zoleikhaei, Y., Mulder, J. A., and Cawood, P. A.: Integrated detrital rutile and zircon provenance reveals multiple sources for
1641 Cambrian sandstones in North Gondwana, *Earth-Sci. Rev.*, 213, 103462, <https://doi.org/10.1016/j.earscirev.2020.103462>,
1642 2021.

1643

Formatted: Font color: Black

Formatted: Normal, Space After: 10 pt, Border: Top: (No border), Bottom: (No border), Left: (No border), Right: (No border), Between : (No border)